PROGRESSIVE FAILURE ANALYSIS OF LAMINATED COMPOSITE STRUCTURES

by

Eduardo Moas

Dissertation submitted to the Faculty of the
Virginia Polytechnic Institute and State University
in partial fulfillment of the requirements for the degree of

DOCTOR OF PHILOSOPHY

in

Engineering Mechanics

APPROVED:

O. H. Griffin, Chairman

M. S. Cramer

M. W. Hyer

E. R. Johnson

L. Librescu

April, 1996
Blacksburg, Virginia

C-2

Progressive Failure Analysis of Laminated Composite Structures

by

Eduardo Moas

Dr. O. H. Griffin, Chairman

(ABSTRACT)

A methodology for progressive failure analysis is presented that is applicable to thin composite structures undergoing large deformations. The method is based on a nonlinear shell theory that accounts for geometric and material nonlinearities. An isoparametric, displacement-based finite element formulation is used to discretize the nonlinear shell equations and an iterative solution is obtained via the Newton-Raphson method. Phenomenological failure criteria are used to predict the onset of damage in the material. Damage is treated using nonlinear constitutive relationships where the material properties are degraded to simulate loss of load-carrying capability. Unlike traditional ply discount models where properties are degraded in an entire ply, the damage models are evaluated at several material points within each ply during the element integration. This allows damage to be localized within an element or ply, and reduces finite element mesh sensitivity since localized damage can develop even in a relatively coarse mesh.

An experimental program was conducted to validate the progressive failure analysis. Six foot diameter graphite/epoxy frames—representative of ring stiffeners for rotorcraft fuselage—were tested in quasi-static crush tests that simulated crash loading of the rotorcraft. Excellent agreement was obtained between the analysis and experiments: the analysis successfully predicted the failure load, the magnitude of unloading at failure, and the residual stiffness of the frames after failure for several different frame configurations. Several parameters affecting the progressive failure analysis are investigated including nonlinear solution procedures, material failure data, damage models, and finite element mesh effects.

ACKNOWLEDGEMENTS

I would like to thank my advisor, Dr. O. Hayden Griffin, for providing me the opportunity to complete this work, for his support and guidance throughout the project, and for firmly letting me know when I was finished. I would also like to thank Drs. Mark S. Cramer, Michael W. Hyer, Eric R. Johnson, and Livieu Librescu for serving on my graduate committee.

This work was supported in part under NASA Grant NAG1-343 by the Landing and Impact Dynamics Branch, NASA Langley Research Center under the auspices of the NASA-Virginia Tech Composites Program. I would like to thank Dr. Hyer, Director, NVTCP, and Mr. Huey D. Carden, Head, LIDB, for the opportunity to participate in this program. Dr. Richard L. Boitnott served as grant monitor and assisted in much of the experimental work reported herein. I am grateful for his valuable insight and support throughout this work.

This work was also supported in part by the Computational Mechanics Branch, NASA Langley Research Center as part of NASA Contract NAS1-19317. I would like to thank Dr. Jerrold M. Housner, Head, CMB, for his comments and suggestions during this work.

Most of the experimental work was performed at Langley Research Center and I would like to acknowledge the valuable assistance of the Landing and Impact Dynamics Branch technical staff, especially Mssrs. George Palko, Donald Reaves, and Kenny Wallace.

Acknowledgements iii

The analytical work was conducted using the Computational Structural Mechanics Testbed, and I am indebted to Ms. Tina Lotts for her unflagging patience and friendly disposition in revealing the depths of the code to me.

I would like to thank my colleagues for their suggestions and insights while performing this work, especially Mr. Richard D. Young and Drs. Ronald C. Averill, Allan Pifko, and Gary M. Stanley.

And finally to my family and friends, I would like to express my love and gratitude for their steadfast support, encouragement, and faith throughout this prolonged endeavor.

TABLE OF CONTENTS

Page

ABSTRACT ii

ACKNOWLEDGEMENTS iii

TABLE OF CONTENTS v

LIST OF FIGURES ix

LIST OF TABLES xii

LIST OF SYMBOLS xiii

1.0 INTRODUCTION 1

1.1 Motivation 1

1.2 Literature Review of Progressive Failure Analysis 3

1.3 Objectives 13

1.4 Organization 14

2.0 NONLINEAR SHELL ANALYSIS 15

2.1 Principle of Virtual Work 15

2.2 Incremental Form of the Principle of Virtual Work 18

2.3 Consistent Linearization 20

2.4 Specialization for Shell Assumptions 22

2.4.1 Geometric and Kinematic Assumptions 22

2.4.2 Local Coordinate System 25

2.4.3 Reduction to Resultant Form 28

3.0 DAMAGE MODEL 33
3.1 Damage Initiation 34
3.1.1 Maximum Strain Criterion 37
3.1.2 Tsai-Wu Criterion 41
3.2 Damage Constitutive Model 46
3.2.1 Ply Discount Model 46
3.2.2 Statistical Strength Model 48

4.0 FINITE ELEMENT FORMULATION 50
4.1 Finite Element Approximation 51
4.1.1 Geometric Approximation 52
4.1.2 Kinematic Approximation 53
4.1.3 Strain Measures 54
4.1.4 Deformation Gradient 56
4.2 Finite Element Matrices 57
4.2.1 Material Stiffness Matrix 57
4.2.2 Geometric Stiffness Matrix 58
4.2.3 External Force Vector 58
4.2.4 Internal Force Vector 59
4.2.5 Finite Element Equations 59
4.3 Numerical Integration 60
4.3.1 Through-Thickness (Constitutive) Integration 60
4.3.2 Two-Dimensional (Element) Integration 62
4.3.3 Selective Reduced Integration 63
4.4 Finite Element Transformations 64
4.5 Nonlinear Solution Procedure 68
4.5.1 Newton-Raphson Method 68
4.5.2 Automatic Load Stepping Algorithm 70

5.0 EXPERIMENTAL PROGRAM 72
5.1 Test Specimen Description 73
5.2 Test Setup and Fixtures 78
5.3 Instrumentation 81
5.3.1 Load Measurement 81
5.3.2 Displacement Measurement 81
5.3.3 Strain Measurement 82
5.3.4 Data Acquisition System 83

6.0 COMPARISON OF ANALYSIS AND EXPERIMENT 84
6.1 Frame Finite Element Model 85
6.2 Linear Response (Prior to Failure) 86
6.3 Nonlinear Response (without Damage) 88
6.4 Nonlinear Response Including Damage 91
6.4.1 Nonlinear Analysis Control Parameters 93
6.4.2 Effect of Material Failure Data 97
6.4.3 Mesh Sensitivity 98
6.4.4 Comparison of Damage Models 99

7.0 CONCLUDING REMARKS 124
7.1 Summary 124
7.2 Guidelines for Progressive Failure Analysis 127
7.3 Conclusions 129
7.4 Recommendations for Future Studies 130

REFERENCES 132

APPENDICES

A. Green-Lagrange (GL) Strain Tensor 137
B. Second Piola-Kirchhoff (2PK) Stress Tensor 140
C. Energy Conjugance of the 2PK and GL Tensors 143
D. Polar Decomposition of the Deformation Gradient 145
E. Rotation Matrix for Small Angles 147
F. Constitutive Transformations for an Off-Axis Ply 150
G. Fiber Bundle Strength Distribution 156

VITA 159

LIST OF FIGURES

Page

1.1 Euler-Type Solution Scheme 5
1.2 Iterative Solution with Material Update During Load Step 10

2.1 Definition of Deformed and Undeformed Configurations 16
2.2 Surface-Oriented Coordinate System Describing Shell Geometry 23
2.3 Local Shell Material/Stress Reference Frame 26

3.1 Principal Material Directions 38
3.2 Maximum Strain Criterion in Stress Space 40
3.3 Inadmissible Branch of Maximum Strain Criterion in Stress Space 40
3.4 45° Off-Axis Strength Test 44

4.1 Mapping of 3D Shell Surface to 2D "Master" Element 53

5.1 Typical Frame Specimen 72
5.2 I-Frame Cross-Section 73
5.3 Illustration of I-Frame Fabrication Technique 73
5.4 Frame Specimen Geometry 76
5.5 Typical Frame Specimen in Testing Machine 78
5.6 Frame Clamping Fixture—Steel Housing 79
5.7 Frame Clamping Fixture—Aluminum Housing 80
5.8 Typical Strain Gage Installation 82

6.1 Finite Element Discretization of Frame Specimen 100
6.2a Load-Deflection Curves—FR001I-2 and FR001I-3 101
6.2b Load-Deflection Curves—FR002I-2 and FR002I-3 102
6.2c Load-Deflection Curves—FR003I-2 103
6.2d Load-Deflection Curves—FR004I-1 and FR004I-2 104
6.2e Load-Deflection Curves—FR005I-1 and FR006I-1 105
6.3 Nonlinear Response Predicted by Analysis (without Damage) Matches Experiments Prior to Failure 106
6.4 Comparison of Analytical and Experimental Circumferential Strain Distribution—FR001I-3 108
6.5 Comparison of Analytical and Experimental Circumferential Strain Distribution—FR002I-3 109
6.6 Comparison of Analytical and Experimental Circumferential Strain Distribution—FR003I-2 110
6.7 Comparison of Analytical and Experimental Circumferential Strain Distribution—FR006I-1 111
6.8 Nonlinear Response of FR001I-3 Exhibits Convergence Problems 112
6.9 FR001I-3 First Buckling Mode—Out-of-Plane Bending/Twisting 113
6.10 FR001I-3 Second Buckling Mode—Localized Web/Cap Flange Crippling 114
6.11 Addition of Mode I Imperfection Does Not Stabilize FR001I-3 Response 115
6.12 Addition of Mode II Stabilizes FR001I-3 Response 115
6.13 Progressive Failure Analysis Compared to Experiment 116
6.14 Damage Development Predicted by Progressive Failure Analysis for Frame FR004I-1 (Maximum Strain Criterion with Ply Discount) 117
6.15 Cap Flange Delamination 118
6.16 Comparison of Analysis Results With and Without Damage 118
6.17 Effect of DES_ITERS Nonlinear Analysis Contol Parameter 119
6.18 Constant Load Step (DES_ITERS=0) Can Result in Poor Failure Load Prediction 119
6.19 Typical Error Convergence Behavior 120
6.20 Comparison of Damage Analysis for AS4/3502 and T300/5208 120

6.21 Effect of Finite Element Mesh on Damage Analysis Results 121
6.22 Comparison of Maximum Strain and Tsai-Wu Failure Criteria 122
6.23 Comparison of Discount and Statistical Strength Damage Models 123
6.24 Material Property Degradation in Statistical Strength Damage Model 123

A.1 Line Segments in Deformed and Undeformed Configurations 137
B.1 Force Vectors Due to 2PK and Cauchy Stresses 140
E.1 1-2-3 Rotation of Orthogonal Triad 148
F.1 Laminated Composite Construction 150
F.2 Orthotropic Ply with Rotation θ about the x_3-axis 153
G.1 Fiber Bundle Chain 156

LIST OF TABLES

Page

4.1 Nodal Coordinates and Weights for Gaussian Quadrature 63

5.1 Laminate Stacking Sequence for the Frame Flange and Web 74
5.2 Average Flange Thickness and Web Height Measurements 75
5.3 Frame Radius and Arc Length Measurements 76

6.1 Comparison of Analytical and Experimental Frame Stiffness 87
6.2 Comparison of Analytical and Experimental Critical Loads 90
6.3 Material Failure Data Representative of AS4/3508 97

LIST OF SYMBOLS

$\mathbf{A}$	laminate extensional stiffness matrix
a, b	finite element nodal indices
$\mathbf{B}$	laminate extension-bending coupling stiffness matrix
$\mathbf{B}_L$	linear, incremental strain-displacement matrix
$\mathbf{C}$	material constitutive (stiffness) tensor
$\widehat{\mathbf{C}}$	integrated constitutive matrices
$\mathbf{C}^S$	transverse shear stiffness matrix
$\mathbf{D}$	laminate bending stiffness matrix
$\mathbf{d}$	vector of (incremental) kinematic variables, $\mathbf{d}^T = (\mathbf{u}^T\ \boldsymbol{\theta}^T)$
E_α	Young's moduli referred to principal material axes
$\mathbf{e}_i$	basis vectors
$\mathbf{e}_i^\ell$	basis vectors for local (lamina) coordinate frame
$\mathbf{e}, \widehat{\mathbf{e}}$	vector of strains, strain mesures
$\mathbf{e}$	linear components of Green-Lagrange strain tensor
$\mathbf{e}^0$	midplane strain measures
$\mathbf{F}$	coefficients of stress tensor polynomial
$\mathbf{F}^{ext}, \mathbf{F}^{int}$	external, internal finite element force vector
f	scalar failure function (stress tensor polynomial)
$\mathbf{f}^B, \mathbf{f}^S$	vector of body forces, surface tractions
G_{ij}	shear moduli referred to principal material axes
$\mathbf{G}$	coefficients of strain tensor polynomial
$\mathbf{g}, \mathcal{G}$	matrices defining the incremental displacement gradient
g	scalar failure function (strain tensor polynomial)
$\mathbf{H}$	integrated transverse shear stiffness matrix
h	shell (laminate) thickness
$\mathbf{I}_N$	$N \times N$ identity matrix
$\mathbf{J}, \mathbf{J}^0$	Jacobian matrix, surface Jacobian matrix

$\mathbf{K}^{matl}, \mathbf{K}^{geom}$ material, geometric stiffness matrices

$\widehat{\mathbf{M}}, \mathbf{M}$ vector, matrix, respectively, of integrated stress couples

${}^t\widehat{\mathbf{N}}, {}^t\mathbf{N}$ vector, matrix, respectively, of integrated stress resultants

$\mathcal{N}$ matrix of stress resultants

N_a two-dimensional interpolation functions

$\mathbf{N}$ matrix of interpolation functions

$\mathbf{Q}$ integrated shear stress resultants

$\mathbf{Q}, \overline{\mathbf{Q}}$ reduced material stiffness matrix referred to material, laminate axes

$\mathbf{q}$ vector of element kinematic variables

$\mathbf{R}$ rotation matrix

$\mathbf{r}$ system of nonlinear equilibrium equations

S surface

$\mathbf{s}$ components of the second Piola-Kirchhoff stress tensor

$\mathbf{S}$ material constitutive (compliance) matrix

$\mathbf{T}$ second order tensor transformation matrix

$\mathbf{u}$ displacement vector

$\overline{\mathbf{u}}^i$ incremental midsurface displacement vector

$\hat{\mathbf{u}}$ incremental relative displacement vector (due to rotations)

${}^tV$ volume

$\mathbf{v}_i$ reference basis vectors attached to the shell "pseudonormal"

$\mathbf{x}$ shell coordinates

$\overline{\mathbf{x}}$ shell midsurface/reference surface coordinates

$\hat{\mathbf{x}}$ shell "pseudonormal" vector

$\mathbf{x}^\ell$ local (lamina) coordinate reference frame

$\mathbf{Z}$ partitioning matrix

z shell through-thickness coordinate referred to midsurface

$\overline{z}$ shell through-thickness coordinate referred to finite element reference surface

z_{ref} offset of shell midsurface from finite element reference surface

β shape factor in Weibull probability distribution function

$\boldsymbol{\gamma}$ transverse shear strain measures

δ variational operator

δ_{ij} Kronecker delta function

$\boldsymbol{\varepsilon}_\alpha$ curvilinear basis vectors for shell surface defined by ζ = constant

$\boldsymbol{\varepsilon}$ infinitesimal strain tensor

$\boldsymbol{\epsilon}$ Green-Lagrange strain tensor

$\boldsymbol{\epsilon}^C, \boldsymbol{\epsilon}^T$ compressive, tensile allowable values for strain tensor

$\widehat{\boldsymbol{\epsilon}}$ vector of strain measures

$\zeta, \overline{\zeta}$ nondimensional through-thickness coordinate referred to shell midsurface, finite element reference surface

η_{ij} nonlinear components of Green-Lagrange strain tensor

$\boldsymbol{\Theta}$ skew-symmetric rotation matrix

$\boldsymbol{\theta}$ incremental rotation angles

$\boldsymbol{\kappa}$ midplane curvature strain measures

ν_{ij} Poisson's ratios referred to principal material axes

ξ_α shell curvilinear coordinates; nondimensional isoparametric coordinates

$\boldsymbol{\sigma}$ second Piola-Kirchhoff stress tensor

$\boldsymbol{\sigma}^C, \boldsymbol{\sigma}^T$ compressive, tensile allowable values for stress tensor, respectively

$\boldsymbol{\tau}$ Cauchy stress tensor

CHAPTER 1
INTRODUCTION

1.1 Motivation

Laminated, fiber-reinforced composite materials are finding an increasing number of applications in many industries due to their high strength-to-weight ratio, the ability to tailor laminate properties for specific applications, and their improved fatigue life and corrosion resistance. This is especially evident in military aircraft, *e.g.*, the YF-22 Advanced Tactical Fighter uses 23 percent graphite-reinforced composites, compared with 35 percent aluminum, 24 percent titanium, and five percent steel. NASA's Advanced Composites Technology program has been studying design and manufacturing issues for an all composite transport aircraft.

One of the major concerns with the use of composites in aircraft is the effect of these materials' inherent brittleness on the structure's stiffness and strength. Traditionally, structures have been designed to meet certain failure criteria related to material failure or stability-related phenomenon. In some cases such as with a fuselage skin, the structure may be allowed to buckle and the post-buckling response is considered. Generally, however, the analysis does not consider the behavior of the structure after material failure is predicted.

While laminated composite materials are susceptible to damage, they also exhibit residual stiffness and strength due to redistribution of the load through the structure. This can take place at many structural levels: at a micromechanics level, where load is transferred around a broken fiber; at the laminate level where undamaged plies take up load from a cracked ply; or in a built-up structure where redundant load paths exist. Analytical methods have been developed to analyze the response of the structure after material damage is initiated and consist of two parts: predicting the onset of damage and calculating the subsequent accumulation of damage. The overall goal of this work is to investigate these progressive failure methods.

This type of analysis has many applications, *e.g.*, in the analysis of aircraft and automotive vehicle crashworthiness. The progressive failure analysis yields information about the energy dissipated by the structure during a crash and allows for improved crashworthy designs. Another application is the evaluation of damage tolerance, *e.g.*, impact damage, where an impact causes an initial damage state. In this case the analysis is used to determine the residual stiffness of the damaged structure, the growth of the damage area, and the ultimate strength at catastrophic failure. Yet another application is in the area of fracture mechanics, where the progressive failure analysis can be applied at the micromechanics level to study crack propagation and delamination.

Progressive failure analysis methods have been developed primarily for two-dimensional applications, as will be discussed in the next section. Furthermore, the applications generally have been limited to geometrically linear cases. The research described herein seeks to extend this work to treat combined materially and geometrically nonlinear problems applicable to large deformations. A materially nonlinear damage model is introduced that degrades the mechanical material properties locally at a damage site. Large structural deformations are allowed to

treat geometrically nonlinear problems. The analytical predictions are compared to experimental results from crush tests of full-scale structural components.

1.2 Literature Review of Progressive Failure Analysis

The literature for progressive failure analysis can be divided into two broad approaches:

(1) The damage is modeled as a discrete phenomenon and the analysis predicts the initiation and accumulation of the discrete damage occurrences.

(2) The damage is modeled by some average or effective measure.

An example of the first approach is in the study of matrix cracking, where the load to initiate matrix cracking is determined and the damage accumulation is sought in terms of the crack density for the damaged ply (*e.g.*, see [Reifsnider, et al., 1982]). Damage is also treated discretely in the study of delamination, *e.g.*, see [O'Brien, 1990]. Damage initiation is determined by the onset of delamination, and the accumulation can be analyzed in terms of the growth of edge delaminations or the occurrence of multiple delaminations through the thickness of the laminate. For both matrix cracking and delamination studies, the analyses and testing have been limited to the laminate coupon scale.

In the second approach for progressive failure analysis, two methods have emerged to provide the average or effective damage measures. In the field of continuum damage mechanics, the damage is represented by internal state variables that are volumetric averages of the damage state [Allen, 1994]. The damaged material is

considered to be elastic, and the damage enters the constitutive description of the material as an effective strain:

$$\epsilon_{ij} = C_{ijkl}\sigma_{kl} + \alpha_{ij} \tag{1-1}$$

where α_{ij} are the damage internal state variables. The second method uses a nonlinear material description where the damage is modeled in terms of a nonlinear constitutive tensor:

$$\epsilon_{ij} = C_{ijkl}(\epsilon_{mn})\sigma_{kl} \tag{1-2}$$

This material degradation method is the subject of the current study, and the literature pertaining to the method is reviewed next.

Generally, the ply degradation methods use some type of failure criterion to determine the onset of damage in a ply and the corresponding damage mode. The material property degradation is associated with a particular failure mode, and the failure modes are assumed to act independently. An incremental analysis is used in which the load is applied to the structure as a series of small steps. Early work in this area used an Euler-type solution, illustrated in Fig. 1.1, where the material properties were held constant during a load step and updated properties were used in subsequent steps. More recent work refined this method using an iterative solution which allowed damage to develop within a load step.

Euler-Type Solution—Constant Material Properties During Load Step

Petit and Waddoups [1969] presented a method for the nonlinear analysis of laminated composites loaded to ultimate failure and including the effects of material nonlinearity and a progressive damage model. The material nonlinearity was handled by utilizing a simple Euler-type integration procedure: the average laminate stresses $\overline{\sigma}$ were added incrementally, and the increment in the laminate strains

$\Delta\epsilon$ was computed assuming the laminate behaved linearly over the applied stress increment:

$$\Delta\epsilon_{n+1} = \mathbf{A}_n^* \Delta\overline{\sigma}_{n+1} \tag{1-3}$$

where $\mathbf{A}_n^* = \mathbf{A}_n^{-1}$ is the laminate compliance matrix, which was calculated from the experimentally determined lamina tangent moduli and Poisson's ratio at the n'th load increment. The total strain at load step $n+1$ was obtained by adding the strain increment to the previous strain state:

$$\epsilon_{n+1} = \epsilon_n + \Delta\epsilon_{n+1} \tag{1-4}$$

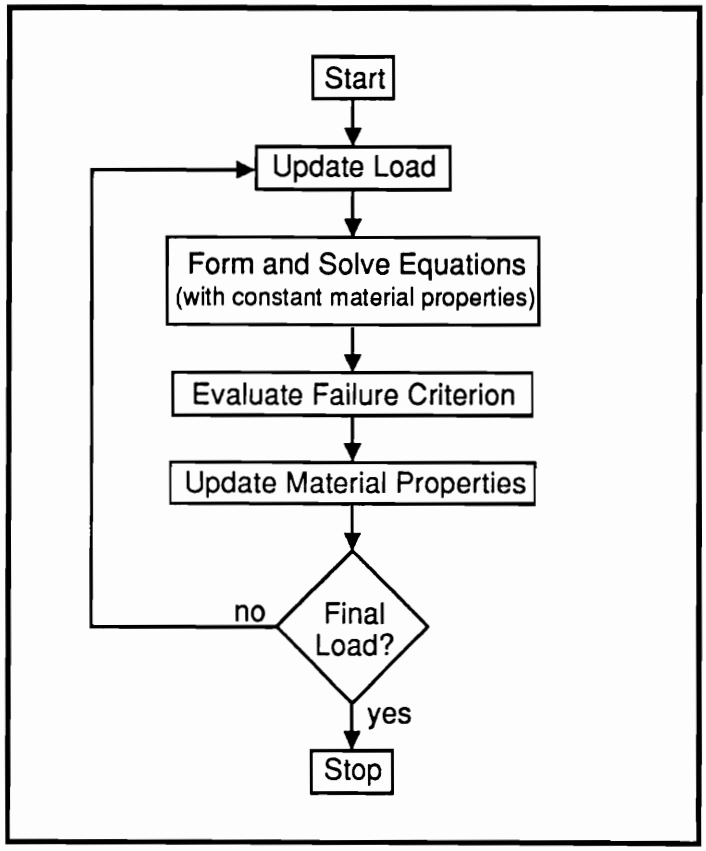

Fig. 1.1 Euler-Type Solution Scheme

A maximum strain failure criterion was used to predict the initiation of damage in the lamina, and three failure modes were included: longitudinal, transverse, and shear modes. The failed lamina was assumed to unload through a steep negative tangent modulus until no load remained in the lamina. It was assumed that degradation was restricted to the failed lamina and was not transmitted to adjacent lamina, and the lamina damage had the effect of unloading the stress in the direction associated with the failure (longitudinal, transverse, or shear). The analysis was continued in this manner until ultimate failure, which was assumed to occur when the laminate stiffness matrix **A** became singular or a negative term appeared on the diagonal of the stiffness matrix.

Petit and Waddoups showed reasonable correlation of the analysis with experimental results from tests of boron/epoxy laminates, even when considerable material nonlinearity was present. Some experimental failures occurred before the predicted laminate ultimate failures, which were attributed to statistical variations in the lamina stress-strain curves. They suggested that improved ultimate strength predictions could be obtained by using lamina stress-strain curves with a sound statistical basis.

Grimes and Whitney [1974] used this method to predict the laminate strength of orthotropic laminates. They reported reasonable correlation between analytical predictions and results from tests of $[0/90]_C$ and $[\pm 45]_C$ laminates of HTS/ERL-2256 graphite/epoxy material.

Humphreys [1981] developed a method to predict damage initiation and growth in composite laminates subjected to low velocity, low mass lateral impact. Humphrey's analysis was limited to the case of a thin, symmetrically laminated plate undergoing small deformations. It was assumed that the damage-induced bending-extension coupling was highly localized and thus was ignored in the analysis. The

analysis used a transient dynamic finite element analysis, and the damage predicted at a time step was included in the analysis of subsequent time steps.

The analysis allowed for fiber and in-plane matrix failure modes, predicted using Hashin's failure theory, and an interlaminar failure mode to predict onset of delamination. The element stiffness matrix was reformed using the appropriate material degradation model when a failure mode was detected. For the matrix damage mode, the transverse properties of the ply were removed: $E_2 = G_{12} = 0$. For the fiber damage mode, all lamina moduli were set to zero: $E_1 = E_2 = G_{12} = 0$. For the interlaminar delamination mode, there was no effect on the element stiffness matrix due to the assumption that the Kirchhoff kinematic assumptions were still valid.

Shivakumar, et al. [1983] studied progressive damage in thin, circular plates due to static-equivalent impact loads. The analysis was based on a minimum total potential energy method using the von Kárman nonlinear strain-displacement equations. The solution domain was divided into a number of subdomains in the radial, cicumferential and thickness directions. The problem was solved by incrementing the transverse displacement and calculating the resultant plate load and ply stresses. The analysis considered quasi-isotropic laminates that were flexurally anisotropic. However, the degree of anisotropy was assumed to be small and the deformations were assumed to be axisymmetric.

The Tsai-Wu criterion was used to determine when the state of stress caused failure in a subdomain. The mode of failure was determined by the stress component that most nearly satisfied the maximum stress criterion. The modes of failure were limited to ply splitting and fiber failure. Elements that failed by splitting were considered to have lost their transverse modulus and transverse shear modulus: $E_2 = G_{12} = 0$. When a fiber failure was detected, complete loss of stiffness was assumed in the element: $E_1 = E_2 = G_{12} = 0$. The reduced moduli were used in

the failed elements in the subsequent steps of the analysis. Because the process of reducing the in-plane lamina moduli increased flexural anisotropy, the analysis was restricted to mildly damaged plates.

The analysis was compared to test results for both static and impact tests of circular laminated plates with different radii. Comparisons were made of the laminate damage length and fiber damage width. Good correlation between the analysis and test results was obtained for static loading, however the correlation was poorer for impact loading.

In the methods discussed above, the usual practice was to model a cracked ply by reducing the transverse and shear moduli to zero. Tsai [1988] argued that this was unacceptable because the cracked ply was not completely disintegrated. He proposed replacing the cracked ply with a continuum of lower stiffness so that conventional stress analysis could be applied. Tsai used a semi-empirical method to replace the cracked plies with quasi-homogeneous plies. The degree of matrix stiffness reduction was observed from experiments on laminates with partially or totally degraded plies. Then a micromechanics analysis was used to predict the loss in transverse and shear moduli due to reduction in matrix modulus.

Tsai modified this approach for cases when a micromechanics analysis was not available (*e.g.*, many laminate analysis and finite element analysis programs are based on macromechanics and do not include micromechanics analysis capabilities). Tsai recommended empirical constants for various lamina degradation factors, and used rule-of-mixtures equations to determine the loss of transverse ply stiffness and in-plane shear stiffness.

Woodson [1994] incorporated this approach in a beam analysis using a curved, thin-walled composite beam theory. Comparisons with experiments of semicircular, graphite/epoxy frames showed that the analysis captured the first major failure

event with reasonable accuracy, and predictions of the total energy absorbed followed the trend of the experiments. Woodson used the frame data from the present study for his analytical comparisons.

Iterative Solution—Material Update During Load Step

The progressive failure analysis method described in the papers above was refined by using an iterative technique to allow for load redistribution at a particular load step. The approach adopted by many researchers can be summarized by the following steps, illustrated in Fig. 1.2:

1. Increment load.
2. Form finite element equations.
3. Solve finite element equations.
4. Obtain ply-level stresses and strains in principal material axes by post-processing.
5. Test for failure using ply failure criterion.

6a. If no failure is detected, go to Step 1.

6b. If a failure is detected, apply the appropriate material damage model corresponding to the failure mode and go to Step 2.

Lee [1982] developed a three-dimensional finite element analysis program to predict the damage accumulation and ultimate strength for a fiber-reinforced composite laminate. The analysis was applied to a rectangular, symmetrically laminated plate with a centered, circular cutout subjected to in-plane biaxial loading. The analysis used linear, eight-noded solid elements to model the laminate. Three failure modes were considered in the analysis: fiber breakage, matrix failure and delamination. A maximum stress failure criterion was employed that compared the normal stress and shear stress associated with each mode to the stress allowables for that mode. For fiber breakage, the lamina stiffness matrix was reduced to zero. For the matrix and delamination failure modes, the lamina stiffness matrix was degraded by

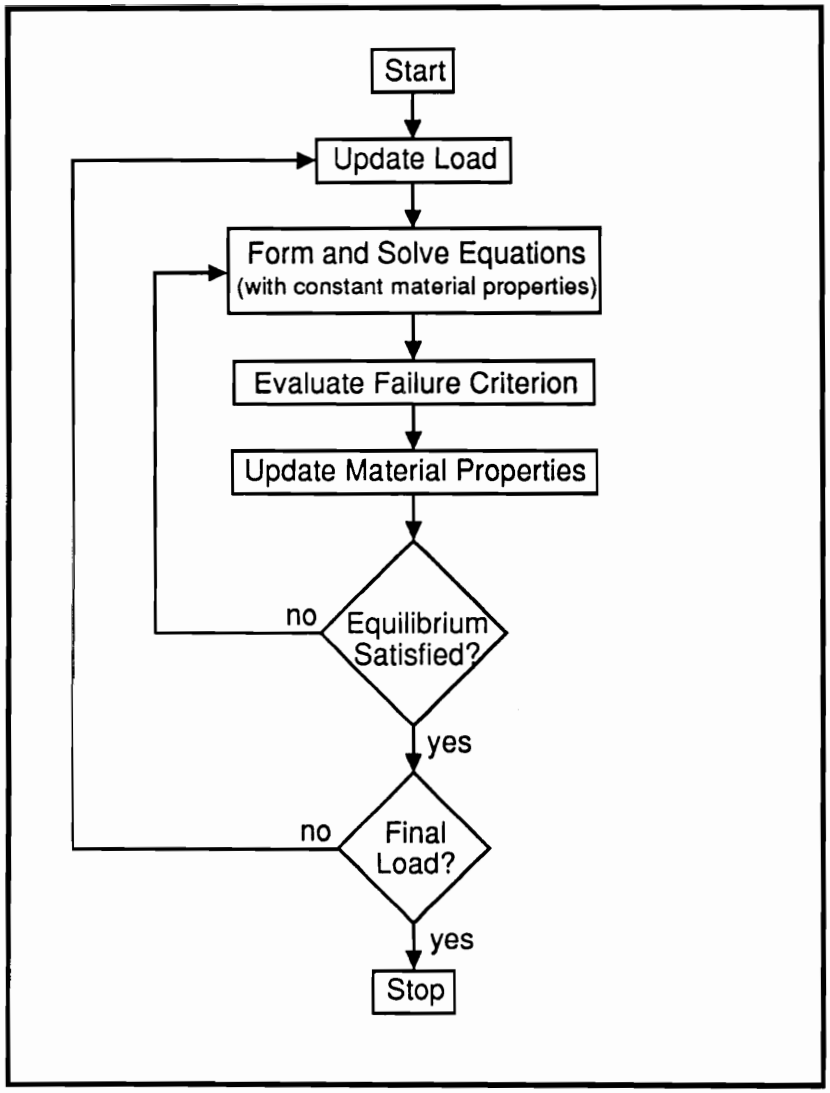

Fig. 1.2 Iterative Solution with Material Update During Load Step

reducing to zero the moduli and major Poisson's ratio associated with the lamina transverse and normal directions, rspectively:

$$E_2 = G_{12} = G_{23} = \nu_{12} = \nu_{23} = 0 \quad \longrightarrow \quad \text{(matrix failure mode)}$$

$$E_3 = G_{13} = G_{23} = \nu_{13} = \nu_{23} = 0 \quad \longrightarrow \quad \text{(delamination failure mode)}$$

Stresses sampled at a single point were taken to be representative of the entire element.

Pandey [1987, see also Pandey and Reddy, 1987] developed a post-first-ply failure analysis algorithm that was implemented in a two-dimensional finite element code for laminated plates and shells. The analysis was applied to a laminated plate with a hole subjected to uniaxial tension, and to a rectangular, simply-supported laminated plate under uniform pressure. Several failure criteria were compared, including maximum stress, maximum strain, Tsai-Hill, Hoffman, and Tsai-Wu. The individual contribution from each stress component to the failure criterion was computed and failure indices were defined as $\alpha_I = \sigma_I / f$, where $I = 1, 2, 6$, and f is the value of the failure criterion. These indices were used to interpret the mode of failure and to reduce the stiffness in the post-first-ply failure analysis. Once the first-ply failure load was reached, the elastic constants of the failed ply were reduced according to:

$$\begin{aligned} E_1^{n+1} &= (1 - \alpha_1) E_1^n \\ E_2^{n+1} &= (1 - \alpha_2) E_2^n \\ G_{12}^{n+1} &= (1 - \alpha_6) G_{12}^n \end{aligned} \tag{1-5}$$

The analysis was completed iteratively as described above except a load-scaling algorithm was employed. If the failure criterion was not exactly satisfied, the applied load was either increased or decreased according to the value of the failure index. For example, if the failure index was greater than one, the applied load increment and displacement solution were decreased proportionally until the failure criterion was exactly satisfied.

Chang, et. al. [1987, 1987a, 1987b, 1989a, 1989b] developed a progressive failure damage model for laminated composites containing stress concentrations using the numerical procedure described above. Four different in-plane failure modes are considered: fiber breakage, fiber-matrix shearing, matrix cracking, and matrix compression failure. Both fiber breakage and fiber-matrix shearing were predicted by the Yamada-Sun criterion [Yamada and Sun, 1978]; Hashin's failure criterion was

used for the matrix failure modes. Chang used a nonlinear shear stress-strain relation in his formulation and modified the failure criterion to account for the history of shear deformation. Chang used the in-situ shear strength, which is the actual shear strength of a ply in a laminate and reflects the effect of lamination on ply shear strength. Experiments have shown that the in-situ shear strength is significantly higher than shear strengths measured for single plies [Yamada and Sun, 1978, and Chang and Chen, 1987].

For a matrix mode failure (tension or compression) the transverse modulus and Poisson's ratio were reduced to zero: $E_2 = \nu_{12} = 0$; The longitudinal modulus and shear stress-strain relation remain unchanged. For fiber breakage or fiber-matrix shearing, both E_2 and ν_{12} were reduced to zero; the degree of property degradation for E_1 and G_{12} was assumed to depend on the size of the damage area predicted by the failure criterion. The property degradation model was based on a micromechanics approach for fiber bundle strength (see Appendix G) and the longitudinal and shear moduli were degraded according to a Weibull distribution:

$$\begin{aligned} E_1 &= E_1^0 \exp\left[-\left(\frac{A}{A_0}\right)^{\beta}\right] \\ G_{12} &= G_{12}^0 \exp\left[-\left(\frac{A}{A_0}\right)^{\beta}\right] \end{aligned} \tag{1-6}$$

where superscript 0 denotes the undamaged moduli, A is the area of the damage zone predicted by the failure criterion, and A_0 is the area of the fiber failure interaction zone associated with the measured ply tensile strength X_T [Rosen, 1965, and Tsai and Hahn, 1980]. β is the shape parameter of the Weibull distribution, and it was assumed that the property degradation distribution had the same shape as the fiber strength reduction.

Chang et al. applied this method to bolted composite joints [1987b], to a cylindrical composite shell subjected to out-of-plane loadings [1989a], and to a laminated composite plate containing an open hole [1989b]. Comparisons with experimental

data yielded reasonable correlation, even for laminates exhibiting extreme nonlinear behavior.

1.3 Objectives

Previous work in the area of progressive failure analysis generally has been limited to geometrically linear problems, and to small-scale application problems. The overall goal of this study is to provide a rigorous foundation for including damage models in a geometrically nonlinear analysis that admits large deformations, and to demonstrate the analysis with tests of large-scale structural components.

The specific objectives of the research are summarized below:

1. *Develop analysis that includes the effect of material damage as it progresses through the structure.* The analysis will consider static loading, account for geometric and material nonlinearities, and be applicable to laminated shell structures.

2. *Incorporate material damage models that define the pointwise constitutive properties as a function of the damage state.* Phenomenological failure criteria will be used to determine the onset of damage and to identify the failure mode. The damage state is defined by the failure mode (*e.g.*, matrix cracking, fiber breakage, *etc.*) and the state of strain at the point.

3. *Conduct an experimental program with frame/skin sections to provide data for validating the analysis.* Six foot diameter, semicircular graphite/epoxy specimens were crushed to simulate crash-loading of an aircraft fuselage. The results from these tests will be compared with the analysis to evaluate the progressive failure analysis.

1.4 Organization

The remainder of this report is divided into seven chapters. Chapter 2 includes a derivation of the nonlinear shell theory used to model the structural response. The theory is based on a linearized, incremental form of the principle of virtual work, and is further specialized for thin shells.

The damage models are described in Chapter 3, including the phenomenological failure criteria used to predict the onset of damage, and the constitutive models used to predict the post-failure material behavior.

Chapter 4 describes the finite element solution of the nonlinear shell theory described in Chapter 2. An isoparametric finite element formulation is used with selective reduced integration to treat element locking. The nonlinear algebraic equations are solved via the Newton-Raphson method.

The experimental program is discussed in Chapter 6, including descriptions of the frame/skin specimens, testing apparatus, and data acquisition system. The analytical and experimental results are compared in Chapter 7.

Finally, Chapter 8 summarizes the findings of this work and includes recommendations for future research.

CHAPTER 2
NONLINEAR SHELL ANALYSIS

The analysis of the structural response due to arbitrary loading and boundary conditions will be formulated using the principle of virtual work, which is described in Section 2.1. The resulting nonlinear equations are solved using an incremental approach, whereby the solution is obtained at a series of load steps that trace the nonlinear response. The incremental strategy improves the ability of the predictor-corrector solution methods to converge by keeping the predicted solution in the neighborhood of the converged solution. The incremental form of the principle of virtual work is derived in Section 2.2. The nonlinear equations are linearized in Section 2.3 to obtain a form that is suitable for solution by the Newton-Raphson method. The linearized equations are specialized for thin shell structures in Section 2.4.

2.1 Principle of Virtual Work

The principle of virtual work states that a body is in equilibrium if the virtual work due to actual stresses acting on kinematically admissible virtual displacements is zero. The principle is valid for any configuration of the body as it undergoes

deformation, as illustrated in Fig. 2.1, where the initial configuration at time 0 and the deformed configuration at time t are assumed to be known, and time $t + \Delta t$ is the current, unknown configuration.

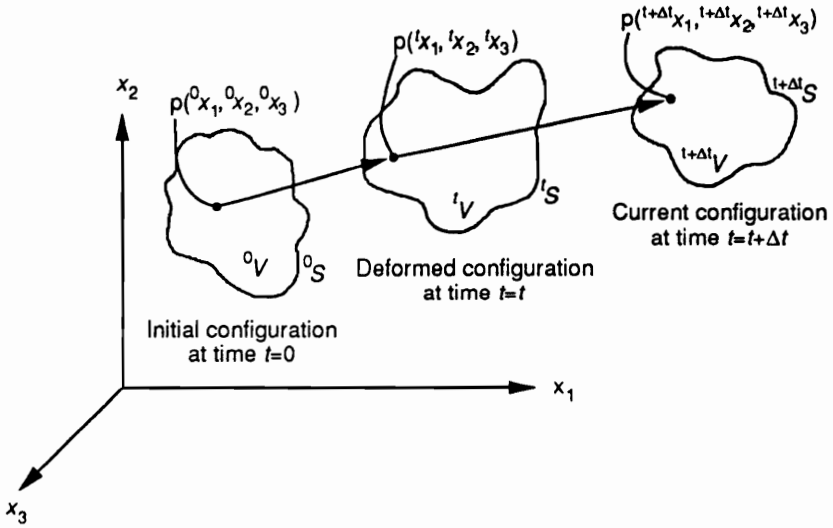

Fig. 2.1 Definition of Deformed and Undeformed Configurations

In the following development we use a left superscript to denote the configuration of the body. The principle of virtual work can be stated mathematically for the current (unknown) configuration as:

$$0 = {}^{t+\Delta t}\mathcal{F}^{ext} - \int_{t+\Delta t V} {}^{t+\Delta t}\tau_{ij}\, \delta\varepsilon_{ij}\, {}^{t+\Delta t}dV \tag{2-1}$$

where τ_{ij} is the Cauchy stress tensor (referred to the current configuration), ε_{ij} is the infinitesimal strain tensor,

$$\varepsilon_{ij} = \frac{1}{2}\left(\frac{\partial u_i}{\partial\, {}^{t+\Delta t}x_j} + \frac{\partial u_j}{\partial\, {}^{t+\Delta t}x_i}\right) \tag{2-2}$$

and $\mathcal{F}^{ext}$ is the virtual work due to the applied body forces f_i^B and surface tractions f_i^S,

$${}^{t+\Delta t}\mathcal{F}^{ext} = \int_{t+\Delta t V} {}^{t+\Delta t}f_i^B\, \delta u_i\, {}^{t+\Delta t}dV + \int_{t+\Delta t S} {}^{t+\Delta t}f_i^S\, \delta u_i\, {}^{t+\Delta t}dS \tag{2-3}$$

The evaluation of Eq. 2-1 presents some difficulty since we cannot integrate over the unknown configuration described by the volume ${}^{t+\Delta t}V$ and surface area ${}^{t+\Delta t}S$. However, any energetically conjugate measures of stress and strain may be used in the principle of virtual work; a widely used pair of stress and strain measures are the Piola-Kirchhoff stress tensor, σ_{ij}, and the Green-Lagrange strain tensor, ϵ_{ij}. These stress and strain measures are referred to previous (known) configurations, which allows for the evaluation of the principle of virtual work stated in terms of these measures. For the sake of brevity, the derivations of ϵ_{ij} and σ_{ij} are not included here, but may be found in Appendices A and B, respectively. Also, the proof that σ_{ij} and ϵ_{ij} are energetically conjugate is included in Appendix C.

In the total Lagrangian formulation the stress and strain measures are referred to the undeformed configuration at time 0; in the updated Lagrangian formulation they are referred to the known configuration at time t. Mathematically, the updated and total Lagrangian formulations are identical and lead to exactly the same numerical results. However, the updated Lagrangian formulation is simpler from an implementation point of view since there are no initial displacement effects as in the total Lagrangian formulation. Thus in the present study the updated Lagrangian formulation is used to develop the incremental, nonlinear governing equations. Then the principle of virtual work can be stated as:

$$0 = {}^{t+\Delta t}\mathcal{F}^{ext} - \int_{{}^{t}V} {}^{t+\Delta t}\sigma_{ij}\, \delta {}^{t+\Delta t}\epsilon_{ij}\, {}^{t}dV \tag{2-4}$$

where $\sigma_{ij}, \epsilon_{ij}$ are referred to the known configuration at time t.

2.2 Incremental Form of the Principle of Virtual Work

Next, we turn our attention to the incremental form of the principle of virtual work. The second Piola-Kirchhoff stress tensor is invariant under rigid body rotation (see Appendix B), and can be decomposed as follows:

$$^{t+\Delta t}\sigma_{ij} = {}^{t}\sigma_{ij} + \sigma_{ij} \tag{2-5}$$

where the absence of the left superscript in σ_{ij} denotes this as an incremental quantity. The Cauchy stresses cannot be decomposed directly since they are not invariant under rigid body motion, thus the stress increment (due to straining) will not account for the change in the Cauchy stresses due to the rigid body motion.

The Green-Lagrange strain tensor is related to the displacement gradient by (see Appendix A):

$$^{t+\Delta t}\epsilon_{ij} = \tfrac{1}{2}({}^{t+\Delta t}u_{i,j} + {}^{t+\Delta t}u_{j,i} + {}^{t+\Delta t}u_{r,i}\,{}^{t+\Delta t}u_{r,j}) \tag{2-6}$$

where $()_{,i}$ denotes differentiation with respect to $^{t}x_i$. Generally, the displacements can be decomposed in the same manner as the stress tensor:

$$^{t+\Delta t}u_i = {}^{t}u_i + u_i \tag{2-7}$$

However in the updated Lagrangian formulation, the displacements are referred to the (known) configuration at time t, so $^{t}u_i = 0$ (thus eliminating the initial displacement terms), and

$$^{t+\Delta t}u_i = u_i \tag{2-8}$$

Substituting Eq. 2-8 in 2-6 results in the following decomposition for the strain tensor:

$$^{t+\Delta t}\epsilon_{ij} = e_{ij} + \eta_{ij} \tag{2-9}$$

where e_{ij}, η_{ij} are the linear and nonlinear (in u_i) components of the strain increment, given by

$$e_{ij} = \tfrac{1}{2}(u_{i,j} + u_{j,i}) \tag{2-10}$$

$$\eta_{ij} = \tfrac{1}{2}(u_{r,i}u_{r,j}) \tag{2-11}$$

The variation in strain at time $t + \Delta t$ is given by

$$\delta^{t+\Delta t}\epsilon_{ij} = \delta\epsilon_{ij} = \delta e_{ij} + \delta\eta_{ij} \tag{2-12}$$

where

$$\delta e_{ij} = \tfrac{1}{2}(\delta u_{i,j} + \delta u_{j,i}) \tag{2-13}$$

$$\delta\eta_{ij} = \tfrac{1}{2}(u_{r,i}\delta u_{r,j} + \delta u_{r,i}u_{r,j}) \tag{2-14}$$

Substituting the decomposed form of the stress and strain tensors (Eqs. 2-5 and 2-12, respectively) in 2-4 yields the following incremental form for the principle of virtual work:

$$\int_{{}^tV} (\sigma_{ij}\delta\epsilon_{ij} + {}^t\sigma_{ij}\delta e_{ij} + {}^t\sigma_{ij}\delta\eta_{ij})\, {}^tdV = {}^{t+\Delta t}\mathcal{F}^{ext} \tag{2-15}$$

Note from Eq. 2-13 that $\delta\epsilon_{ij}$ is constant for a given δu_i. Thus the term ${}^t\sigma_{ij}\delta e_{ij}$ (representing the virtual work due to internal forces at time t) is a "known" quantity and can be brought to the right hand side:

$$\int_{{}^tV} (\underbrace{\sigma_{ij}\delta\epsilon_{ij}}_{\mathcal{K}^{matl}} + \underbrace{{}^t\sigma_{ij}\delta\eta_{ij}}_{\mathcal{K}^{geom}})\, {}^tdV = {}^{t+\Delta t}\mathcal{F}^{ext} - \int_{{}^tV} \underbrace{{}^t\sigma_{ij}\delta e_{ij}}_{\mathcal{F}^{int}}\, {}^tdV \tag{2-16}$$

Equation 2-16 is the incremental form of the principle of virtual work. Several variational "operators" can be identified which will be considered in detail in the sequel: the material stiffness, geometric stiffness and internal force operators. Note that this expression is exact, *i.e.*, no approximations have been made up to this point. Next we consider how to linearize the variational statement.

2.3 Consistent Linearization

The basic approach used to solve the nonlinear equations resulting from the incremental form of the principle of virtual work is to linearize the equations about a known configuration. This is done in a "consistent" manner by considering the contribution from each term and retaining only those terms that are linear in u_i; terms containing higher-order powers of u_i are discarded. This introduces certain approximations to the principle of virtual work, so the solution to the linearized equations is no longer exact. The approximate solution can be improved by iteration, as discussed in Chapter 4.

We first consider the geometric stiffness operator in Eq. 2-16 and expand ${}^t\sigma_{ij}\delta\eta_{ij}$ using Eq. 2-14, *i.e.*,

$$ {}^t\sigma_{ij}\delta\eta_{ij} = \tfrac{1}{2}{}^t\sigma_{ij}(u_{r,i}\delta u_{r,j} + \delta u_{r,i}u_{r,j}) = {}^t\sigma_{ij}u_{r,i}\delta u_{r,j} \tag{2-17} $$

where the symmetry of the stress tensor is used to simplify the result. Since this result contains only linear terms in u_i, it is already in the desired linearized form.

The material stiffness operator is a function of the generally nonlinear stress-strain relationships that can be written as

$$ {}^t\sigma_{ij} = {}^tC_{ijkl}{}^t\epsilon_{kl} \tag{2-18} $$

The constitutive relationships used in the present study are discussed in detail in Chapter 3. The use of Eq. 2-18 can be justified on several counts. First, in the present study we consider fiber-reinforced composite materials which are generally linearly elastic, and exhibit brittle failure modes at relatively small strains. Second, the use of the Piola-Kirchhoff stress tensor and Green-Lagrange strain tensor admits the use of Eq. 2-18, because the tensors remain invariant under rigid body

rotation. So for small strain analysis in the presence of large displacements and rotations, Eq. 2-18 is equivalent to the generalized form of Hooke's law for infinitesimal conditions [Bathe, 1982].

The incremental form of the stress-strain relationships can be obtained by performing a Taylor series expansion around ${}^t\sigma_{ij}$ and neglecting the higher-order terms of ϵ_{kl}:

$$\begin{aligned} \sigma_{ij} &= \frac{\partial {}^t\sigma_{ij}}{\partial {}^t\epsilon_{kl}} \epsilon_{kl} + \mathcal{O}(\epsilon_{kl}^2) \\ &\approx C_{ijkl}\epsilon_{kl} \end{aligned} \tag{2-19}$$

where C_{ijkl} is the incremental stiffness and is tangent to the stress-strain curve at time t.

Next, expanding $\epsilon_{ij} = e_{ij} + \eta_{ij}$ results in

$$\sigma_{ij} \approx C_{ijkl}\epsilon_{kl} = \underline{C_{ijkl}e_{kl}} + \underline{\underline{C_{ijkl}\eta_{kl}}} \tag{2-20}$$

The terms underlined once and twice are linear and quadratic functions of u_i, respectively, and only the linear part is retained:

$$\sigma_{ij} \approx C_{ijkl}e_{ij} \tag{2-21}$$

Then the material stiffness operator in Eq. 2-16 can be approximated by

$$\sigma_{ij}\delta\epsilon_{ij} \approx C_{ijkl}e_{kl}\delta\epsilon_{ij} = \underline{C_{ijkl}e_{kl}\delta e_{ij}} + \underline{\underline{C_{ijkl}e_{kl}\delta\eta_{ij}}} \tag{2-22}$$

Again, the term underlined once is linear in u_i and is retained, and the term underlined twice is quadratic and is discarded:

$$\sigma_{ij}\delta\epsilon_{ij} \approx C_{ijkl}e_{kl}\delta e_{ij} \tag{2-23}$$

Finally, the linearized, incremental form of the principle of virtual work becomes

$$\int_{{}^tV} (\underbrace{C_{ijkl}e_{kl}\delta e_{ij}}_{\mathcal{K}^{matl}} + \underbrace{{}^t\sigma_{ij}u_{r,i}\delta u_{r,j}}_{\mathcal{K}^{geom}})\, {}^tdV = {}^{t+\Delta t}\mathcal{F}^{ext} - \int_{{}^tV} \underbrace{{}^t\sigma_{ij}\delta e_{ij}}_{\mathcal{F}^{int}}\, {}^tdV \tag{2-24}$$

The specialization of the variational statement for thin shells is considered next.

2.4 Specialization for Shell Assumptions

Up to this point the incremental nonlinear equations have been developed in a general form; the only approximation was to linearize the material stiffness operator in the variational statement. Next we introduce certain kinematic assumptions for thin shells which allow further simplification of the variational statement. Specifically, a first-order shear deformation theory is adopted that is analogous to the Mindlin-Reissner theory for flat plates ([Reissner, 1944 and 1945] and [Mindlin, 1951]). As a result the variational operators become explicit functions of the through-thickness coordinate and are pre-integrated in the through-thickness direction, leading to a resultant form involving two-dimensional integrals over the shell midsurface.

2.4.1 Geometric and Kinematic Assumptions

The undeformed shell geometry is defined by the surface-oriented coordinates illustrated in Fig. 2.2:

$$ {}^0x_i(\xi_\alpha) = {}^0\overline{x}_i + z\,{}^0\widehat{x}_i \tag{2-25} $$

where ${}^0\overline{x}_i$ are the coordinates of a point on the shell midsurface defined by the curvilinear coordinates ξ_α, ${}^0\widehat{x}_i$ are the components of the unit vector normal to the midsurface, and z is the through-thickness coordinate measured along the normal:

$$ z = \frac{h}{2}\zeta, \qquad -1 \le \zeta \le 1 \tag{2-26} $$

A first-order shear deformation theory is adopted to describe the deformed geometry, which states that normals to the midsurface before deformation remain straight but not necessarily normal to the midsurface after deformation, and the

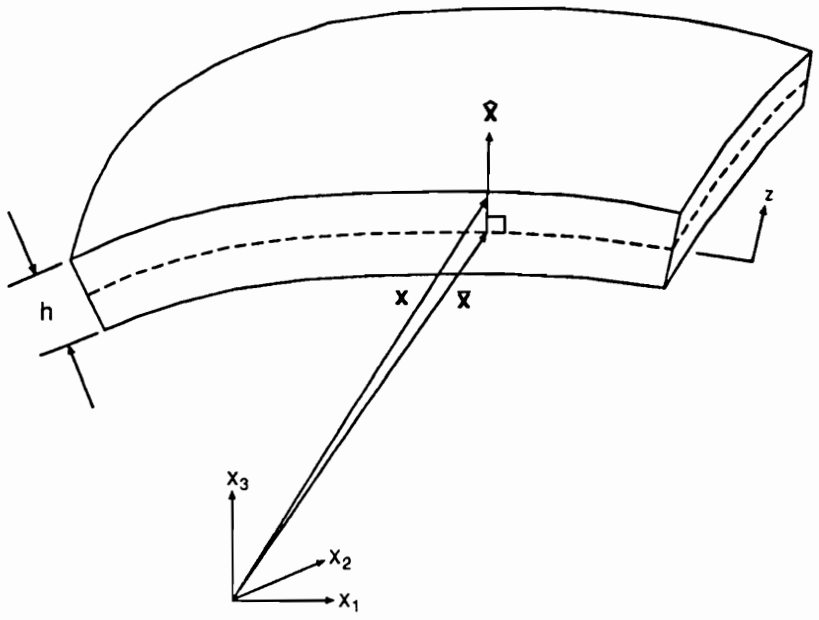

Fig. 2.2 Surface-Oriented Coordinate System Describing Shell Geometry

normals do not change length. Thus the deformed geometry at time t may be described by

$$ {}^{t}x_i(\xi_\alpha) = {}^{t}\overline{x}_i + z\,{}^{t}\widehat{x}_i \tag{2-27} $$

where ${}^{t}\overline{x}_i$ are the coordinates of the deformed midsurface and ${}^{t}\widehat{x}_i$ are the components of the "pseudonormal" vector that was originally normal to the midsurface.

The incremental displacements going from the configuration at time t to the one at time $t + \Delta t$ are

$$ u_i(\xi_\alpha) = {}^{t+\Delta t}x_i - {}^{t}x_i = \overline{u}_i + z\widehat{u}_i \tag{2-28} $$

where $\overline{u}_i$, $\widehat{u}_i$ are the incremental midsurface displacements and relative displacements, respectively:

$$ \overline{u}_i = {}^{t+\Delta t}\overline{x}_i - {}^{t}\overline{x}_i \tag{2-29} $$

$$ \widehat{u}_i = {}^{t+\Delta t}\widehat{x}_i - {}^{t}\widehat{x}_i \tag{2-30} $$

The relative displacements represent the change in the pseudonormal vector which can be expressed in terms of rotations θ_i from some previous configuration:

$$^{t+\Delta t}\hat{\mathbf{x}} = \mathbf{R}(\theta_i)\, ^{t}\hat{\mathbf{x}} \tag{2-31}$$

where $\mathbf{R}$ is a rotation matrix that is a nonlinear function of θ_i and generally depends on the order in which the θ_i are applied. For small (incremental) rotations, small angle approximations may be used to simplify the rotation matrix (*e.g.*, see Appendix E):

$$\mathbf{R} = \mathbf{I}_3 + \boldsymbol{\Theta} \tag{2-32}$$

where $\boldsymbol{\Theta}$ is a skew-symmetric matrix given by

$$\boldsymbol{\Theta} = \begin{bmatrix} 0 & -\theta_3 & \theta_2 \\ \theta_3 & 0 & -\theta_1 \\ -\theta_2 & \theta_1 & 0 \end{bmatrix} \tag{2-33}$$

The assumption of small angles is not too restrictive: the rotations must remain small within an increment Δt, however they may accumulate to allow large motion of the body. Substituting Eqs. 2-31, 2-32 in 2-30, the relative displacements are given by

$$\hat{\mathbf{u}} = {}^{t+\Delta t}\hat{\mathbf{x}} - {}^{t}\hat{\mathbf{x}} = \boldsymbol{\Theta}\, ^{t}\hat{\mathbf{x}} = \boldsymbol{\theta} \times {}^{t}\hat{\mathbf{x}} \tag{2-34}$$

where $\boldsymbol{\theta}^T = (\theta_1 \ \theta_2 \ \theta_3)$ is the axial vector corresponding to the skew-symmetric matrix $\boldsymbol{\Theta}$.

Equation 2-34 may be rewritten as:

$$\hat{\mathbf{u}} = \boldsymbol{\chi} \times \boldsymbol{\theta} \tag{2-35}$$

where

$$\boldsymbol{\chi} = \begin{bmatrix} 0 & {}^{t}\hat{x}_3 & -{}^{t}\hat{x}_3 \\ -{}^{t}\hat{x}_3 & 0 & {}^{t}\hat{x}_1 \\ {}^{t}\hat{x}_2 & -{}^{t}\hat{x}_1 & 0 \end{bmatrix} \tag{2-36}$$

This result expresses the rotational equivalence of the shell relative displacements, and will be used in Chapter 4 to transform the shell finite element equations to a "standard" form with rotational degrees of freedom.

The rotations θ_i may be measured with respect to any arbitrary reference vectors, $\mathbf{v}_i$. However, these may be chosen at time t such that ${}^t\mathbf{v}_3 = {}^t\widehat{\mathbf{x}}$, so ${}^t\widehat{\mathbf{x}} = {}^t\mathbf{v}_1 \times {}^t\mathbf{v}_2$. Then using the vector triple product, Eq. 2-34 becomes

$$\widehat{\mathbf{u}} = \boldsymbol{\theta} \times ({}^t\mathbf{v}_1 \times {}^t\mathbf{v}_2) = \theta_2 {}^t\mathbf{v}_1 - \theta_1 {}^t\mathbf{v}_2 \tag{2-37}$$

Then the relative displacements with respect to $\mathbf{v}_i$ are simply

$$\begin{aligned} \widehat{u}_{v_1} &= \theta_2 \\ \widehat{u}_{v_2} &= -\theta_1 \\ \widehat{u}_{v_3} &= 0 \end{aligned} \tag{2-38}$$

Note that when Eq. 2-35 is transformed to this local basis, the transformation matrix $\boldsymbol{\chi}$ is revealed in its simplest form [Stanley, 1985]:

$$\boldsymbol{\chi} = \begin{bmatrix} 0 & 1 & -1 \\ -1 & 0 & 1 \\ 1 & -1 & 0 \end{bmatrix} \tag{2-39}$$

2.4.2 Local Coordinate System

The variational operators are most naturally evaluated in a local reference frame $\mathbf{x}^\ell$ that is tangent to the surface defined by ζ = constant, as shown in Fig. 2.3. The curvilinear basis vectors for this surface are given by

$$\boldsymbol{\varepsilon}_\alpha = \frac{\partial {}^t\mathbf{x}}{\partial \xi_\alpha}\Big|_{\zeta=\text{constant}} \tag{2-40}$$

Define the local x_3^ℓ-direction as normal to this surface:

$$\mathbf{e}_3^\ell = \frac{\boldsymbol{\varepsilon}_1 \times \boldsymbol{\varepsilon}_2}{|\boldsymbol{\varepsilon}_1 \times \boldsymbol{\varepsilon}_2|} \tag{2-41}$$

The local x_1^ℓ-direction can be defined as parallel to $\boldsymbol{\varepsilon}_1$, and the x_2^ℓ-direction completes a right-hand coordinate system:

$$\begin{aligned} \mathbf{e}_1^\ell &= \frac{\boldsymbol{\varepsilon}_1}{|\boldsymbol{\varepsilon}_1|} \\ \mathbf{e}_2^\ell &= \mathbf{e}_3^\ell \times \mathbf{e}_1^\ell \end{aligned} \tag{2-42}$$

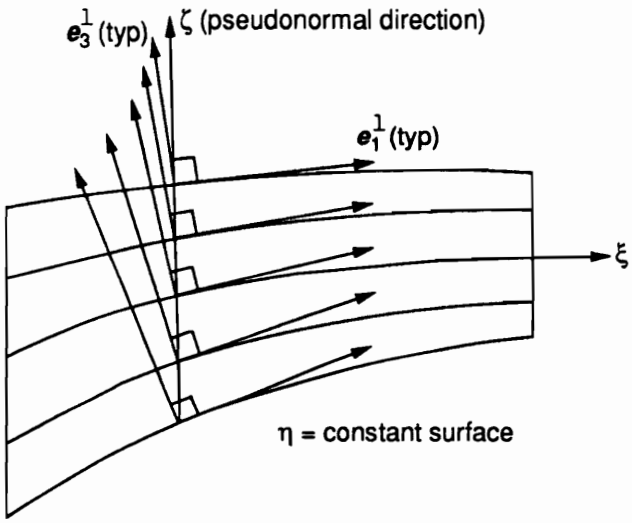

Fig. 2.3 Local Shell Material/Stress Reference Frame (after [Hughes, 1987])

Of special interest is the transformation of the gradient operator between the local and curvilinear coordinates, which is required to evaluate the strain tensor:

$$\boldsymbol{\nabla}_{x^\ell} = \mathbf{J}^{-T} \boldsymbol{\nabla}_\xi \tag{2-43}$$

where the subscript on the gradient operator indicates the reference basis, and $\mathbf{J}$ is the Jacobian matrix listed below:

$$\mathbf{J} = \begin{bmatrix} \frac{\partial x_1^\ell}{\partial \xi_1} & \frac{\partial x_1^\ell}{\partial \xi_2} & \frac{\partial x_1^\ell}{\partial \zeta} \\ \frac{\partial x_2^\ell}{\partial \xi_1} & \frac{\partial x_2^\ell}{\partial \xi_2} & \frac{\partial x_2^\ell}{\partial \zeta} \\ \frac{\partial x_3^\ell}{\partial \xi_1} & \frac{\partial x_3^\ell}{\partial \xi_2} & \frac{\partial x_3^\ell}{\partial \zeta} \end{bmatrix} \tag{2-44}$$

In general, $\mathbf{J}$ is a function of ζ, which complicates the through-thickness integration of the variational statement (see [Stanley, 1985] for a thorough treatment of this subject, especially for thick shells). However, certain simplifying assumptions and observations can be made to alleviate this problem.

First, assume that the shell is of constant thickness, h, so that all surfaces defined by ζ = constant are parallel. Then

$$J_{3\alpha} = \frac{\partial x_3^\ell}{\partial \xi_\alpha} = 0 \tag{2-45}$$

Next, the variation of the Jacobian with respect to the thickness direction can be ignored if the ratio of the shell thickness to the radius is large; in this case we assume that the local $\mathbf{e}_3^\ell$ direction is approximately equal to the shell pseudonormal direction [Stanley, 1985]. Then

$$\begin{aligned} J_{\alpha 3} &= \frac{\partial x_\alpha^\ell}{\partial \zeta} = 0 \\ J_{33} &= \frac{\partial x_3^\ell}{\partial \zeta} = \frac{h}{2} \end{aligned} \tag{2-46}$$

Then the Jacobian matrix can be written as

$$\mathbf{J} = \begin{bmatrix} \mathbf{J}^0 & \mathbf{0} \\ \mathbf{0} & \frac{h}{2} \end{bmatrix} \tag{2-47}$$

where $\mathbf{J}^0$ is the surface Jacobian matrix given by

$$J^0_{\alpha\beta} = \frac{\partial x_\alpha^\ell}{\partial \xi_\beta} = \begin{pmatrix} \mathbf{e}_1^\ell \cdot \boldsymbol{\varepsilon}_1 & \mathbf{e}_1^\ell \cdot \boldsymbol{\varepsilon}_2 \\ \mathbf{e}_2^\ell \cdot \boldsymbol{\varepsilon}_1 & \mathbf{e}_2^\ell \cdot \boldsymbol{\varepsilon}_2 \end{pmatrix} \tag{2-48}$$

2.4.3 Reduction to Resultant Form

Two-Dimensional Strain Measures

The linear strain tensor can now be expressed as an explicit function of the through-thickness z-coordinate. Substituting the incremental displacements from Eq. 2.28 in the linear strain tensor, Eq. 2.10, leads to the usual form from classical lamination theory [Jones, 1975]:

$$\begin{aligned} e_{\alpha\beta} &= e^0_{\alpha\beta} + z\kappa_{\alpha\beta} \\ e_{\alpha 3} &= k_{(\alpha)}\gamma_{(\alpha)} \qquad \text{(summation suppressed)} \end{aligned} \tag{2-49}$$

where $e^0_{\alpha\beta}, \kappa_{\alpha\beta}$ are midplane strains and curvatures, respectively, and γ_α are transverse shear strains:

$$e^0_{\alpha\beta} = \tfrac{1}{2}(\overline{u}_{\alpha,\beta} + \overline{u}_{\beta,\alpha}) \tag{2-50}$$

$$\kappa_{\alpha\beta} = \tfrac{1}{2}(\widehat{u}_{\alpha,\beta} + \widehat{u}_{\beta,\alpha}) \tag{2-51}$$

$$\gamma_\alpha = (\overline{u}_{3,\alpha} + \widehat{u}_\alpha) \tag{2-52}$$

and all derivatives are assumed to be taken with respect to the local reference frame. The k_α in Eq. 2-49 are transverse shear correction factors [Whitney, 1973], and the parenthesis around the subscripts imply that summation is suppressed.

The conversion between the three-dimensional pointwise strains and the two-dimensional strain measures can be expressed conveniently by introducing the Z-partitioning matrix [Stanley, 1985]:

$$\mathbf{e} = \mathbf{Z}\hat{\mathbf{e}} \tag{2-53}$$

where the strain vector is reordered to form membrane and transverse shear partitions:

$$\mathbf{e} = \begin{Bmatrix} \mathbf{e}^{(M)} \\ \mathbf{e}^{(S)} \end{Bmatrix}, \quad \mathbf{e}^{(M)} = \begin{Bmatrix} e_{11} \\ e_{22} \\ 2e_{12} \end{Bmatrix}, \quad \mathbf{e}^{(S)} = \begin{Bmatrix} 2e_{13} \\ 2e_{23} \end{Bmatrix} \tag{2-54}$$

and $\hat{\mathbf{e}}$ is the vector of strain measures:

$$\hat{\mathbf{e}} = \begin{Bmatrix} \mathbf{e}^0 \\ \boldsymbol{\kappa} \\ \boldsymbol{\gamma} \end{Bmatrix}, \quad \mathbf{e}^0 = \begin{Bmatrix} e^0_{11} \\ e^0_{22} \\ e^0_{12} \end{Bmatrix}, \quad \boldsymbol{\kappa} = \begin{Bmatrix} \kappa_{11} \\ \kappa_{22} \\ \kappa_{12} \end{Bmatrix}, \quad \boldsymbol{\gamma} = \begin{Bmatrix} \gamma_1 \\ \gamma_2 \end{Bmatrix}, \tag{2-55}$$

and $\mathbf{Z}$ is the Z-partitioning matrix:

$$\mathbf{Z} = \begin{bmatrix} \mathbf{I}_3 & z\mathbf{I}_3 & \mathbf{0} \\ \mathbf{0} & \mathbf{0} & \mathbf{k} \end{bmatrix} \tag{2-56}$$

where $\mathbf{k}$ is a matrix containing the shear correction factors:

$$\mathbf{k} = \begin{bmatrix} k_1 & 0 \\ 0 & k_2 \end{bmatrix} \tag{2-57}$$

Material Stiffness Operator

The material stiffness operator can be recast in matrix form as:

$$\mathcal{K}^{matl} = \int_{{}^tV} C_{ijkl} e_{ij} \delta e_{kl} \, {}^tdV = \int_{{}^tV} \delta \mathbf{e}^T \mathbf{C} \mathbf{e} \, {}^tdV \tag{2-58}$$

where the constitutive matrix $\mathbf{C}$ is partioned to form membrane and shear partitions (*cf.* Eq. F-21):

$$\mathbf{C} = \begin{bmatrix} \overline{\mathbf{Q}} & \mathbf{0} \\ \mathbf{0} & \overline{\mathbf{C}}^{(S)} \end{bmatrix} \tag{2-59}$$

Substituting the Z-partitioning matrix (Eq. 2-53) in 2-58 and integrating through the thickness yields the resultant form of the material stiffness operator:

$$\mathcal{K}^{matl} = \int_{{}^tV} \delta \hat{\mathbf{e}}^T \mathbf{Z}^T \mathbf{C} \mathbf{Z} \hat{\mathbf{e}} \, {}^tdV = \int_{{}^tS} \delta \hat{\mathbf{e}}^T \hat{\mathbf{C}} \hat{\mathbf{e}} \, {}^tdS \tag{2-60}$$

where $\hat{\mathbf{C}}$ contains the integrated constitutive matrices:

$$\hat{\mathbf{C}} = \int_h \mathbf{Z}^T \mathbf{C} \mathbf{Z} \, dz = \begin{bmatrix} \mathbf{A} & \mathbf{B} & \mathbf{0} \\ \mathbf{B} & \mathbf{D} & \mathbf{0} \\ \mathbf{0} & \mathbf{0} & \mathbf{H} \end{bmatrix} \tag{2-61}$$

and

$$(\mathbf{A}, \mathbf{B}, \mathbf{D}) = \int_h \overline{\mathbf{Q}}(1, z, z^2)\, dz \tag{2-62}$$

$$\mathbf{H} = \int_h \overline{\mathbf{C}}^{(S)}\, dz \tag{2-63}$$

Geometric Stiffness Operator

The geometric stiffness operator can be expressed in matrix form as follows:

$$\mathcal{K}^{geom} = \int_{{}^tV} {}^t\sigma_{ij} u_{r,i} \delta u_{r,j}\, {}^tdV = \int_{{}^tV} \{\nabla \delta u_i\}^T \mathbf{s} \{\nabla u_i\}\, {}^tdV \tag{2-64}$$

where $\{\nabla u_i\}$ is a vector that contains components of the displacement gradient:

$$\{\nabla u_i\}^T = \{u_{i,1}\ u_{i,2}\ u_{i,3}\} \tag{2-65}$$

and $\mathbf{s}$ is a matrix containing components of the stress tensor at time t:

$$\mathbf{s} = \begin{bmatrix} {}^t\sigma_{11} & {}^t\sigma_{12} & {}^t\sigma_{13} \\ {}^t\sigma_{12} & {}^t\sigma_{22} & {}^t\sigma_{23} \\ {}^t\sigma_{13} & {}^t\sigma_{23} & {}^t\sigma_{33} \end{bmatrix} \tag{2-66}$$

Note that due to the assumption of plane stress, ${}^t\sigma_{33} = 0$ in $\mathbf{s}$. The z-dependence of the gradient operator can be defined as before by using a smaller version of the Z-partitioning matrix [Stanley, 1985]:

$$\{\nabla u_i\} = \mathbf{Z}^{(G)} \mathbf{g}_i \tag{2-67}$$

where

$$\mathbf{Z}^{(G)} = \begin{bmatrix} \mathbf{I}_2 & z\mathbf{I}_2 & \mathbf{0} \\ \mathbf{0} & \mathbf{0} & 1 \end{bmatrix} \tag{2-68}$$

and

$$\mathbf{g}_i^T = (\overline{u}_{i,1}\ \overline{u}_{i,2}\ \widehat{u}_{i,1}\ \widehat{u}_{i,2}\ \widehat{u}_i) \tag{2-69}$$

Substituting Eq. 2-67 in 2-64 and integrating through the thickness yields the resultant form of the geometric stiffness operator:

$$\mathcal{K}^{geom} = \int_{{}^tV} \delta \mathbf{g}_i^T \mathbf{Z}^{(G)^T} \mathbf{s}\, \mathbf{Z}^{(G)} \mathbf{g}_i \, {}^t dV = \int_{{}^tS} \delta \mathbf{g}_i^T \hat{\mathbf{s}}\, \mathbf{g}_i \, {}^t dS \tag{2-70}$$

where

$$\hat{\mathbf{s}} = \int_h \mathbf{Z}^{(G)^T} \mathbf{s}\, \mathbf{Z}^{(G)}\, dz = \begin{bmatrix} \mathbf{n} & \mathbf{m} & \mathbf{q} \\ \mathbf{m}^T & \mathbf{m}' & \mathbf{q}' \\ \mathbf{q}^T & \mathbf{q}'^T & \mathbf{0} \end{bmatrix} \tag{2-71}$$

and $\mathbf{n}, \mathbf{m}, \mathbf{m}', \mathbf{q}, \mathbf{q}'$ are matrices of integrated stress resultants:

$$(\mathbf{n}, \mathbf{m}, \mathbf{m}') = \int_h \begin{bmatrix} \sigma_{11} & \sigma_{12} \\ \sigma_{12} & \sigma_{22} \end{bmatrix} (1, z, z^2)\, dz \tag{2-72}$$

$$(\mathbf{q}, \mathbf{q}') = \int_h \begin{Bmatrix} \sigma_{13} \\ \sigma_{23} \end{Bmatrix} (1, z)\, dz \tag{2-73}$$

The result in Eq. 2-71 is a general expression for the stress resultants in the geometric stiffness operator. Historically, however, only the nonlinear terms arising from the transverse deflection, $\overline{u}_3$, were considered in thin shell theories [Reissner, 1944]. Improved results can be obtained for built-up structures by considering additional terms from the other midsurface deformations, $\overline{u}_\alpha$, *e.g.*, for modeling stiffened panels in which the webs experience large shear deformations. In the present study, we neglect the effect of the relative displacements, $\widehat{u}_i$, in the displacement gradient and only consider the nonlinear terms resulting from the gradient of the midsurface displacements, $\overline{u}_i$. Then $\mathbf{g}_i$ is approximated by

$$\mathbf{g}_i^T \approx (\overline{u}_{i,1}\ \overline{u}_{i,2}\ 0\ 0\ 0) \tag{2-74}$$

which removes the bending and transverse shear contributions (*i.e.*, the second and third row and column partitions) in Eq. 2-71, leaving

$$\mathcal{K}^{geom} = \int_{{}^tS^e} \delta \tilde{\mathbf{g}}_i^T \mathbf{n} \tilde{\mathbf{g}}_i \, {}^t dS \tag{2-75}$$

where $\tilde{\mathbf{g}}_i^T = (\overline{u}_{i,1}\ \overline{u}_{i,2})$.

Internal Force Operator

The internal force operator can be expressed in matrix form as

$$\mathcal{F}^{int} = \int_{{}^tV} {}^t\sigma_{ij}\delta e_{ij}\, {}^t dV = \int_{{}^tV} \delta\mathbf{e}^T\boldsymbol{\sigma}\, {}^t dV \tag{2-76}$$

where $\boldsymbol{\sigma}$ is reordered to form membrane and transverse shear partitions (consistent with the strain vector in Eq. 2-76):

$$\boldsymbol{\sigma} = \left\{ \begin{array}{c} \boldsymbol{\sigma}^{(M)} \\ \boldsymbol{\sigma}^{(S)} \end{array} \right\}, \quad \boldsymbol{\sigma}^{(M)} = \left\{ \begin{array}{c} \sigma_{11} \\ \sigma_{22} \\ \sigma_{12} \end{array} \right\}, \quad \boldsymbol{\sigma}^{(S)} = \left\{ \begin{array}{c} \sigma_{13} \\ \sigma_{23} \end{array} \right\} \tag{2-77}$$

We can substitute the Z-partitioning matrix (Eq. 2.50), then integrate in the through-thickness direction to obtain the internal force operator in terms of the stress resultants:

$$\mathcal{F}^{int} = \int_{{}^tV} \delta\hat{\mathbf{e}}^T\mathbf{Z}^T\boldsymbol{\sigma}\, {}^t dV = \int_{{}^tS} \delta\hat{\mathbf{e}}^T\hat{\mathbf{N}}\, {}^t dS$$

where

$$\hat{\mathbf{N}} = \int_h \mathbf{Z}^T\boldsymbol{\sigma}\, dz = \left\{ \begin{array}{c} \mathbf{N} \\ \mathbf{M} \\ \mathbf{Q} \end{array} \right\} \tag{2-78}$$

and $\mathbf{N}, \mathbf{M}, \mathbf{Q}$ are vectors of integrated stress resultants:

$$(\mathbf{N}, \mathbf{M}) = \int_h \left\{ \begin{array}{c} {}^t\sigma_{11} \\ {}^t\sigma_{22} \\ {}^t\sigma_{12} \end{array} \right\} (1, z)\, dz \tag{2-79}$$

$$\mathbf{Q} = \int_h \left\{ \begin{array}{c} {}^t\sigma_{13} \\ {}^t\sigma_{23} \end{array} \right\} dz \tag{2-80}$$

CHAPTER 3
DAMAGE MODEL

The response of a laminated composite structure depends on the stiffness and structural integrity of the laminate, which is affected locally when damage develops within a ply. This chapter examines several models that predict both the initiation of damage and the subsequent constitutive behavior of the damaged material. A distinction is made between the constitutive behavior at a material point and that of the laminate. The damage models discussed in this chapter characterize the material behavior at a point within a ply in terms of pointwise strains and stresses. On the other hand, the laminate constitutive properties relate strain measure and integrated stress resultants, and are obtained by integrating the pointwise constitutive relationships through the laminate thickness. In this chapter we only consider the pointwise material behavior and postpone further discussion of the integrated laminate stiffnesses until Chapter 4.

The laminate is constructed from thin, orthotropic plies that may be rotated around their normal axis. The constitutive behavior of the undamaged ply is reviewed in Appendix F, which also introduces a contracted notation for the stress, strain, and constitutive tensors. Phenomenological failure criteria are used to predict the initiation of damage and to identify the associated damage mode for the material. These failure criteria are described in Section 3.1. The constitutive behavior of the damaged material is modeled by degrading the mechanical material

properties as a function of the damage mode to simulate the loss of load-carrying capability in the material. The damage models used in the present study are described in Section 3.2.

3.1 Damage Initiation

Analysis of the failure phenomena in composites can be considered from a mechanistic or a phenomenological point of view. Mechanistic theories model the mechanics of the composite's constituent materials to obtain the physical properties and response of the composite. Such an approach usually requires that a separate micromechanics analysis be completed at each material point (*e.g.*, see [Averill, 1992]),and is too computationally demanding for large-scale structural analysis at the current time. However, this method may become more feasible as computing power and speed increase.

Phenomenological failure theories relate mathematical models to the failure phenomenon and generally depend on empirical curve-fitting to determine the model parameters. Phenomenological failure criteria were chosen for the present study because of their computational efficiency for predicting damage initiation. The criteria are evaluated based on the current state of stress or strain, which are already available in the incremental nonlinear analysis. Thus no additional computational cost is incurred to predict the state of damage at a material point. The literature is replete with the study of phenomenological failure criteria; comprehensive reviews can be found in [Nahas, 1986] and [Sandhu, 1974]. Two commonly used phenomenological failure theories are presented in this section: the maximum strain criterion and the Tsai-Wu criterion.

The failure criteria used to predict the onset of material failure must satisfy certain requirements [Gol'denblat and Kopnov, 1965], [Wu, 1974]:

1. The criterion should be single-valued.
2. The criterion should not be path-dependent.
3. The criterion should be invariant with respect to the choice of the stress/strain reference frame.
4. The criterion should be internally consistent, *i.e.*, possess a unique transformation between stress space and strain space.
5. The criterion should be physically consistent, *i.e.*, give meaningful results compared to experimental measurements of strength.

Although any mathematical model that satisfies the above requirements is admissible as a failure criterion, contemporary research has focused on the development of a scalar (invariant) function in the form of a tensor polynomial. Gol'denblat and Kopnov [1965] were among the first to propose such a function in the following form:

$$f({}^t\boldsymbol{\sigma}, \mathbf{F}) = (F_I {}^t\sigma_I)^\alpha + (F_{IJ} {}^t\sigma_I {}^t\sigma_J)^\beta + (F_{IJK} {}^t\sigma_I {}^t\sigma_J {}^t\sigma_K)^\gamma + \cdots = 1 \qquad (3\text{-}1)$$

where the indices I, J, K range from 1–6 due to the use of contracted notation (see Appendix F), and F_I, F_{IJ}, F_{IJK} are strength tensors of rank two, four, and six, respectively.

Tsai and Wu [1971] simplified Eq. 3-1 to a slightly less general form (see also [Wu, 1974]):

$$f({}^t\boldsymbol{\sigma}, \mathbf{F}) = \underline{F_I {}^t\sigma_I} + \underline{F_{IJ} {}^t\sigma_I {}^t\sigma_J} + \underline{F_{IJK} {}^t\sigma_I {}^t\sigma_J {}^t\sigma_K} + \cdots = 1 \qquad (3\text{-}2)$$

The strength tensors obey the usual tensor transformation laws, so each underlined term in Eq. 3-2 is a scalar invariant, thus satisfying the invariance requirement for the failure criterion. To satisfy the requirement for internal consistency, Eq. 3-2 can be cast as a tensor polynomial in terms of the strain tensor

$$g({}^t\boldsymbol{\epsilon}, \mathbf{G}) = G_I {}^t\epsilon_I + G_{IJ} {}^t\epsilon_I {}^t\epsilon_J + G_{IJK} {}^t\epsilon_I {}^t\epsilon_J {}^t\epsilon_K + \cdots = 1 \qquad (3\text{-}3)$$

The consistency relationsips between Eqs. 3-3 and 3-2 can be derived for a linearly elastic material by use of the constitutive stress-strain relations. Let ${}^t\sigma_I = C_{IJ}{}^t\epsilon_J$ in Eq. 3-2, which yields

$$f({}^t\boldsymbol{\epsilon}, \mathbf{F}) = F_I C_{IL}{}^t\epsilon_L + F_{IJ}C_{IL}C_{JM}{}^t\epsilon_L{}^t\epsilon_M + F_{IJK}C_{IL}C_{JM}C_{KN}{}^t\epsilon_L{}^t\epsilon_M{}^t\epsilon_N + \cdots = 1 \tag{3-4}$$

Comparing Eqs. 3-3 and 3-4 and requiring that the coefficients of like terms be equal yields the transformation relationships between $\mathbf{F}$ and $\mathbf{G}$:

$$\begin{aligned} G_I &= F_L C_{IL} \\ G_{IJ} &= F_{LM}C_{IL}C_{JM} \\ G_{IJK} &= F_{LMN}C_{IL}C_{JM}C_{KN} \end{aligned} \tag{3-5}$$

Likewise, the inverse transformation can be deduced by substituting the compliance relations ${}^t\epsilon_I = S_{IJ}{}^t\sigma_J$ in Eq. 3-3 and comparing the result with Eq. 3-2:

$$\begin{aligned} F_I &= G_L S_{IL} \\ F_{IJ} &= G_{LM}S_{IL}S_{JM} \\ F_{IJK} &= G_{LMN}S_{IL}S_{JM}S_{KN} \end{aligned} \tag{3-6}$$

In the following subsections, two failure criteria used in the present study are examined in detail: the maximum strain criterion and the Tsai-Wu criterion.

3.1.1 Maximum Strain Criterion

The maximum strain criterion for composite materials is an extension of St. Venant's maximum principal strain criterion for isotropic materials. Although St. Venant's criterion yields poor correlation with experimental measurements of strength of ductile metals, better correlation is observed for brittle materials. In the maximum strain criterion, the material is assumed to be orthotropic with respect to the principal material directions and the strains are referred to this reference frame as well. The material directions are shown in Fig. 3.1 and have the usual connotation from classical lamination theory: x_1' is the fiber direction, x_2' is transverse to the fiber in the ply, and x_3' is normal to the ply. Material "failure" occurs when the maximum strain referred to the principal directions exceeds an experimentally determined critical strain. The allowable strain envelope for the case of plane stress is given by

$$\begin{aligned} -\epsilon_1^C < {}^t\epsilon_1 < \epsilon_1^T \\ -\epsilon_2^C < {}^t\epsilon_2 < \epsilon_2^T \\ -\epsilon_6^C < {}^t\epsilon_6 < \epsilon_6^T \end{aligned} \tag{3-7}$$

where $\epsilon_I^C, \epsilon_I^T$ are the compressive and tensile allowable strains, respectively. Usually the in-plane shear failure is assumed to be independent of the sign of the shear strain and the allowable strain envelope for ${}^t\epsilon_6$ can be written as

$$|{}^t\epsilon_6| < \epsilon_6^F \tag{3-8}$$

where $\epsilon_6^C = \epsilon_6^T = \epsilon_6^F$. The maximum strain criterion predicts both the onset of failure and the associated failure mode for a particular state of strain.

The maximum strain criterion can be cast in the form of a tensor polynomial by defining the following function:

$$g = ({}^t\epsilon_1 + \epsilon_1^C)({}^t\epsilon_1 - \epsilon_1^T)({}^t\epsilon_2 + \epsilon_2^C)({}^t\epsilon_2 - \epsilon_2^T)({}^t\epsilon_6 + \epsilon_6^C)({}^t\epsilon_6 - \epsilon_6^T) = 0 \tag{3-9}$$

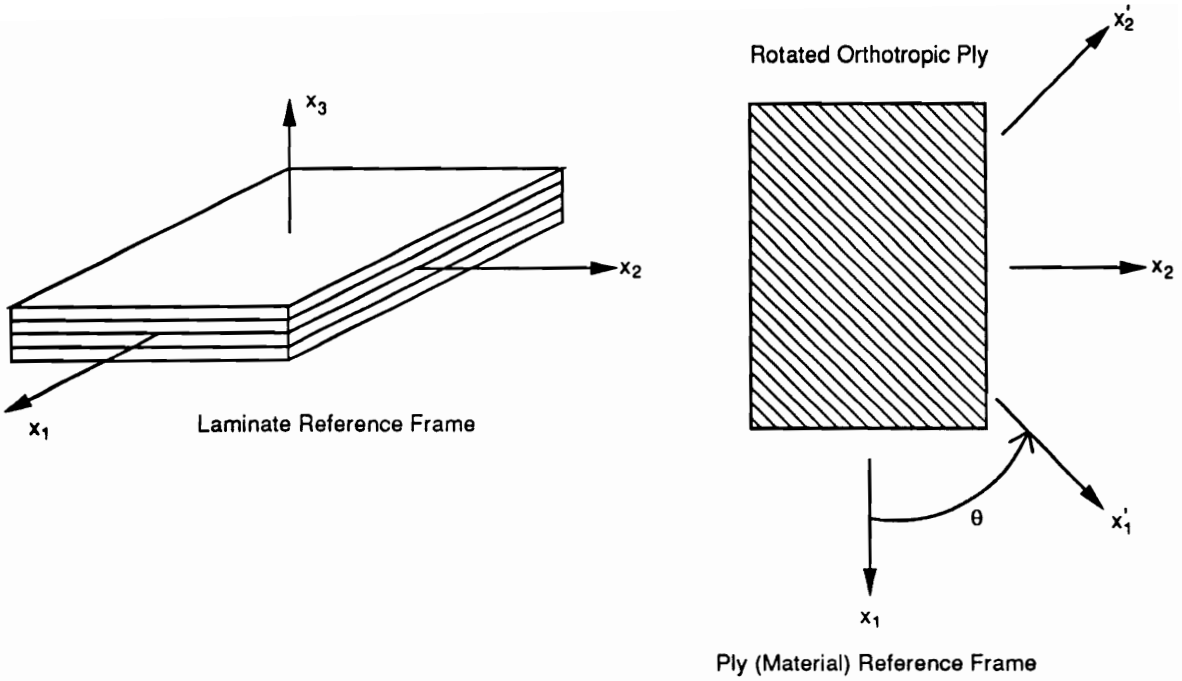

Fig. 3.1 Principal Material Directions

The roots of g correspond to material "failure" due to ${}^t\epsilon_I$ exceeding a critical value, and $g > 0$ corresponds to the allowable envelope described by Eq. 3-7. Expanding Eq. 3-9 yields a sixth order polynomial in ${}^t\epsilon_I$, the coefficients of which are components of the strength tensors up to G_{IJKLMN}, a tensor of rank twelve:

$$g = G_I {}^t\epsilon_I + G_{IJ} {}^t\epsilon_I {}^t\epsilon_J + \cdots + G_{IJKLMN} {}^t\epsilon_I {}^t\epsilon_J {}^t\epsilon_K {}^t\epsilon_L {}^t\epsilon_M {}^t\epsilon_N \qquad (3\text{-}10)$$

Although at first glance there appear to be more coefficients than can be experimentally determined, only six of the coefficients are independendent:

$$\begin{aligned} G_1 &= \frac{1}{\epsilon_1^T} - \frac{1}{\epsilon_1^C} & G_{11} &= \frac{1}{\epsilon_1^T \epsilon_1^C} \\ G_2 &= \frac{1}{\epsilon_2^T} - \frac{1}{\epsilon_2^C} & G_{22} &= \frac{1}{\epsilon_2^T \epsilon_2^C} \\ G_6 &= \frac{1}{\epsilon_6^T} - \frac{1}{\epsilon_6^C} & G_{66} &= \frac{1}{\epsilon_6^T \epsilon_6^C} \end{aligned} \qquad (3\text{-}11)$$

The remaining coefficients are a function of these independent ones [Wu, 1974].

For a linear material the maximum strain criterion can be transformed to stress space by substituting the compliance relations ${}^t\epsilon_I = S_{IJ}{}^t\sigma_J$ in Eq. 3-7:

$$\begin{aligned} -S_{11}\sigma_1^C < S_{1J}{}^t\sigma_J < S_{11}\sigma_1^T \\ -S_{22}\sigma_2^C < S_{2J}{}^t\sigma_J < S_{22}\sigma_2^T \\ -S_{66}\sigma_6^C < S_{6J}{}^t\sigma_J < S_{66}\sigma_6^T \end{aligned} \tag{3-12}$$

where σ_I^C, σ_I^T are compressive and tensile allowable stresses, respectively. This expression can be simplified by the assumption that the material is orthotropic with respect to the material axes. Then $S_{16} = S_{26} = 0$, and Eq. 3-12 becomes

$$\begin{aligned} -\sigma_1^C &< {}^t\sigma_1 + \frac{S_{12}}{S_{11}}{}^t\sigma_2 &< -\sigma_1^T \\ -\sigma_2^C &< {}^t\sigma_2 + \frac{S_{12}}{S_{22}}{}^t\sigma_1 &< -\sigma_2^T \\ -\sigma_6^C &< {}^t\sigma_6 &< -\sigma_6^T \end{aligned} \tag{3-13}$$

The allowable stress envelope can be plotted in ${}^t\sigma_1$-${}^t\sigma_2$ space as shown in Fig. 3.2 assuming $-\sigma_6^C < {}^t\sigma_6 < \sigma_6^T$. Due to the piecewise linear nature of the envelope, some restrictions must be made on the compliance coefficients to ensure the existence of a physically consistent transformation of the envelope from strain space to stress space [Wu, 1974]. For example, consider the branch of the failure envelope corresponding to ${}^t\epsilon_1 = \epsilon_1^T$, which in stress space becomes

$${}^t\sigma_1 + \frac{S_{12}}{S_{11}}{}^t\sigma_2 = \sigma_1^T \tag{3-14}$$

The compliance coefficients can be chosen such that the ${}^t\sigma_2$ intercept of Eq. 3-14 is greater than $-\sigma_2^C$, as shown in Fig. 3.3. This implies that under tension ${}^t\sigma_2$, the induced failure in the x_1-direction will cause failure for ${}^t\sigma_2 > -\sigma_2^C$, and the branch of the failure envelope corresponding to ${}^t\epsilon_2 = -\epsilon_2^C$ can never be reached! This violates the fifth requirement set forth for the failure criterion that the criterion yield physically consistent results compared to experimental measurements of strength.

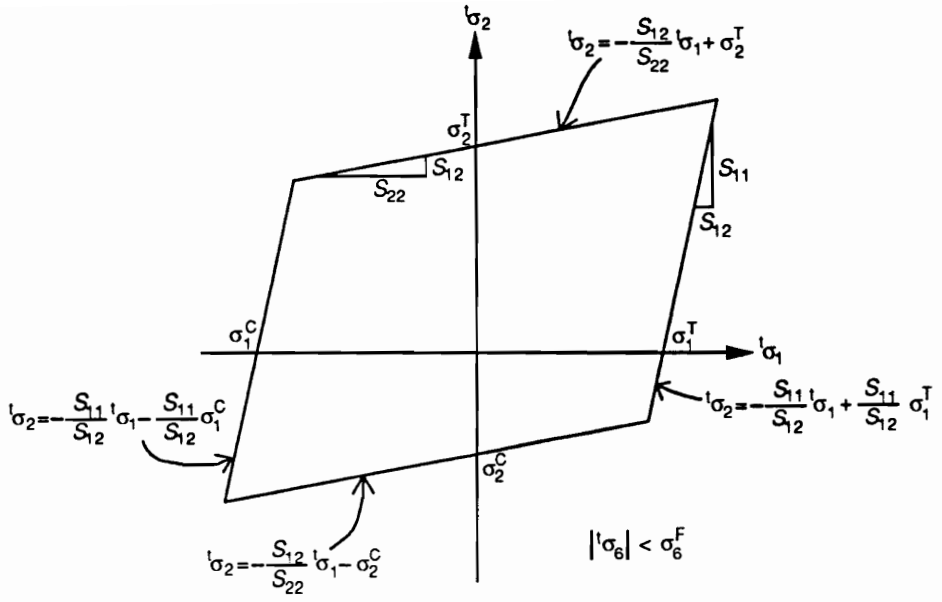

Fig. 3.2 Maximum Strain Criterion in Stress Space

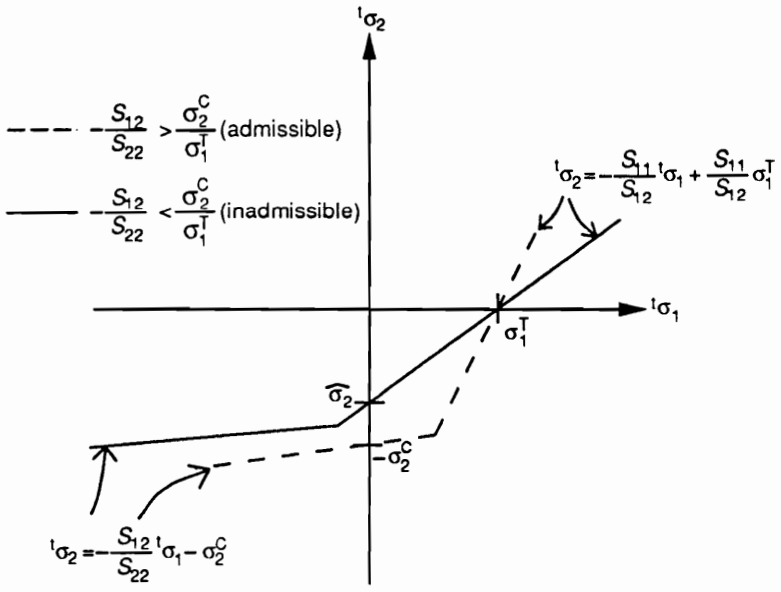

Fig. 3.3 Inadmissible Branch of Maximum Strain Criterion in Stress Space

Thus a requirement for physical consistency is that ${}^t\epsilon_2$ intercept, $\widehat{\sigma}_2$, be less than $-\sigma_2^C$:

$$\widehat{\sigma}_2 = \frac{S_{11}}{S_{12}}\sigma_1^T < -\sigma_2^C \tag{3-15}$$

which yields the following constraint on the compliance coefficients:

$$-\frac{S_{11}}{S_{12}} > \frac{\sigma_2^C}{\sigma_1^T} \tag{3-16}$$

Similar constraint equations can be derived by considering the appropriate intercepts of the three remaining branches in ${}^t\sigma_1$-${}^t\sigma_2$ space:

$$-\frac{S_{11}}{S_{12}} > \frac{\sigma_2^T}{\sigma_1^C} \tag{3-17}$$

$$-\frac{S_{22}}{S_{12}} > \frac{\sigma_1^C}{\sigma_2^T} \tag{3-18}$$

$$-\frac{S_{22}}{S_{12}} > \frac{\sigma_1^T}{\sigma_2^C} \tag{3-19}$$

3.1.2 Tsai-Wu Criterion

Tsai and Wu [1971] proposed a quadratic form of the general tensor polynomial:

$$f({}^t\boldsymbol{\sigma}, \mathbf{F}) = F_I\,{}^t\sigma_I + F_{IJ}\,{}^t\sigma_I\,{}^t\sigma_J = 1 \tag{3-20}$$

Like the general form of the tensor polynomial, Eq. 3-20 is a scalar equation and is invariant to coordinate transformations, *i.e.*, the strength tensors F_I, F_{IJ} can be transformed to an arbitrary reference frame. The conversion of the Tsai-Wu criterion from stress space to strain space for a linear material follows the transformation laws given in Eq. 3.5, repeated here for convenience:

$$\begin{aligned} G_I &= C_{IJ}F_J \\ G_{IJ} &= C_{IM}C_{JN}F_{MN} \end{aligned} \tag{3-21}$$

For the case of plane stress, Eq. 3-20 reduces to:

$$f({}^t\boldsymbol{\sigma}, \mathbf{F}) = F_1 {}^t\sigma_1 + F_2 {}^t\sigma_2 + F_6 {}^t\sigma_6 + F_{11} {}^t\sigma_1{}^2 + 2F_{12} {}^t\sigma_1 {}^t\sigma_2 + 2F_{16} {}^t\sigma_1 {}^t\sigma_6 + F_{22} {}^t\sigma_2{}^2 + 2F_{26} {}^t\sigma_2 {}^t\sigma_6 + F_{66} {}^t\sigma_6{}^2 = 1 \tag{3-22}$$

This expression can be further simplified by assuming that the failure criterion is not influenced by the sign of the shear stress. Then components of f containing linear terms ${}^t\sigma_6$ must vanish (*i.e.*, $F_6 = F_{16} = F_{26} = 0$) and Eq. 3-22 reduces to:

$$f = F_1 {}^t\sigma_1 + F_2 {}^t\sigma_2 + F_{11} {}^t\sigma_1{}^2 + 2F_{12} {}^t\sigma_1 {}^t\sigma_2 + F_{22} {}^t\sigma_2{}^2 + F_{66} {}^t\sigma_6{}^2 = 1 \tag{3-23}$$

The interaction term is constrained by a stability condition that ensures the failure surface will be ellipsoidal—not an open-ended hyperboloid—and intercept each stress axis [Tsai and Wu, 1971]:

$$F_{11} F_{22} - F_{12}^2 \geq 0 \tag{3-24}$$

The tensor components F_1, F_{11} can be related to the normal stress allowables σ_1^C, σ_1^T by assuming a uniaxial stress field that causes failure. Let ${}^t\sigma_1 = \sigma_1^T$, ${}^t\sigma_2 = {}^t\sigma_6 = 0$; then Eq. 3-23 becomes:

$$f = F_1 \sigma_1^T + F_{11} (\sigma_1^T)^2 \tag{3-25}$$

Similarly, for ${}^t\sigma_1 = -\sigma_1^C$, ${}^t\sigma_2 = {}^t\sigma_6 = 0$, Eq. 3-23 becomes:

$$f = -F_1 \sigma_1^C + F_{11} (\sigma_1^C)^2 \tag{3-26}$$

Solving Eqs 3-26 and 3-25 yield expressions for the tensor components F_1, F_{11}:

$$\begin{aligned} F_1 &= \frac{1}{\sigma_1^T} - \frac{1}{\sigma_1^C} \\ F_{11} &= \frac{1}{\sigma_1^T \sigma_1^C} \end{aligned} \tag{3-27}$$

The tensor components F_2, F_2 can be derived in a similar manner and related to the transverse stress allowables σ_2^C, σ_2^T:

$$\begin{aligned} F_2 &= \frac{1}{\sigma_2^T} - \frac{1}{\sigma_2^C} \\ F_{22} &= \frac{1}{\sigma_2^T \sigma_2^C} \end{aligned} \tag{3-28}$$

and F_{66} can be related to shear stress allowable σ_6^F:

$$F_{66} = \left(\frac{1}{\sigma_6^F}\right)^2 \tag{3-29}$$

where we assume that the shear stress failure is independent of the sign of the shear stress, *i.e.*, $\sigma_6^C = \sigma_6^T = \sigma_6^F$. It is interesting to note that the coefficients listed above for F_I, F_{IJ} have the same form as like components of the strength tensors G_I, G_{IJ} of the maximum strain criterion.

The experimental determination of the normal stress interaction term F_{12} presents some difficulty since it involves testing a specimen in a combined stress state with ${}^t\sigma_1, {}^t\sigma_2$ nonzero, and any number of combined stresses is possible. For example, consider a biaxial stress state with ${}^t\sigma_1 = {}^t\sigma_2 = P, {}^t\sigma_6 = 0$, then Eq. 3-22 becomes

$$P(F_1 + F_2) + P^2(F_{11} + 2F_{12} + F_{22}) = 1 \tag{3-30}$$

After substituting the expressions for F_I, F_{IJ} derived above, Eq. 3-30 can be solved for F_{12}:

$$F_{12} = \frac{1}{2P^2}\left[1 - P\left(\frac{1}{\sigma_1^T} - \frac{1}{\sigma_1^C} + \frac{1}{\sigma_2^T} - \frac{1}{\sigma_2^C}\right) - P^2\left(\frac{1}{\sigma_1^T \sigma_1^C} + \frac{1}{\sigma_2^T \sigma_2^C}\right)\right] \tag{3-31}$$

Another approach is to use the 45-degree off-axis specimen to determine the interaction term. In this case, the specimen is loaded to failure in uniaxial tension along a line rotated 45 degrees from the principal material axes (see Fig. 3.4); the equivalent stress state referred to the material axes is ${}^t\sigma_1 = {}^t\sigma_2 = {}^t\sigma_6 = \frac{1}{2}U$, where

U is the applied load. Substituting this stress state in Eq. 3-22 and solving for F_{12} yields [Tsai and Wu, 1971]:

$$F_{12} = \frac{2}{U^2}\left[1 - \frac{U}{2}\left(\frac{1}{\sigma_1^T} - \frac{1}{\sigma_1^C} + \frac{1}{\sigma_2^T} - \frac{1}{\sigma_2^C}\right) - \frac{U^2}{4}\left(\frac{1}{\sigma_1^T\sigma_1^C} + \frac{1}{\sigma_2^T\sigma_2^C} + \left(\frac{1}{\sigma_6^F}\right)^2\right)\right] \tag{3-32}$$

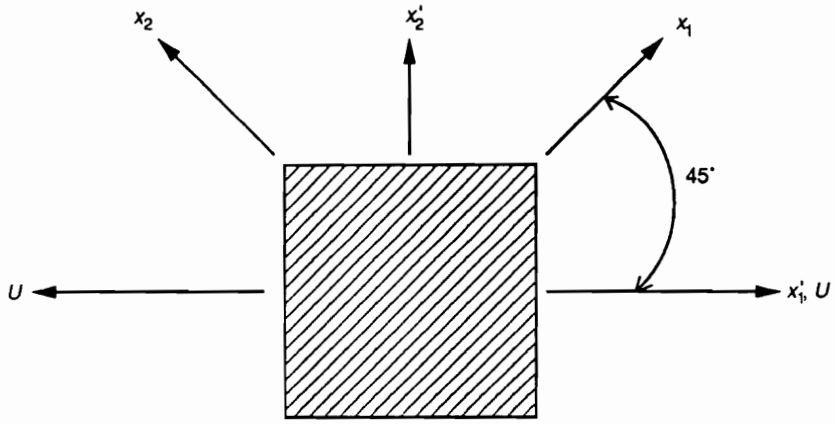

Fig. 3.4 45° Off-Axis Strength Test

Pipes and Cole [1973] showed that the off-axis test was not well suited for determining the interaction parameter F_{12} for boron-epoxy composites. Large variations in the computed value of F_{12} were found for different ply orientations due to F_{12} being a small order term compared to other terms in the tensor polynomial for the off-axis test. However, they found that these large variations in F_{12} produced small changes in the value of the failure criterion. Narayanaswami and Adelman [1977] recommended using the Tsai-Wu criterion with $F_{12} = 0$ and showed good correlation with three different material systems.

Yet another approach used is to choose F_{12} so that the Tsai-Wu theory degenerates to the von Mises-Hencky theory for isotropic plane stress:

$$\left(\frac{{}^t\sigma_1}{\sigma^F}\right)^2 - \frac{{}^t\sigma_1\,{}^t\sigma_2}{(\sigma^F)^2} + \left(\frac{{}^t\sigma_2}{\sigma^F}\right)^2 = 1 \tag{3-33}$$

where σ^F is the isotropic yield stress, and ${}^t\sigma_1, {}^t\sigma_2$ are principal stresses. To transform the Tsai-Wu criterion to this form, assume the stress allowables are equal to the

yield stress, $\sigma_1^T = \sigma_1^C = \sigma_2^T = \sigma_2^C = \sigma^F$; then the tensor components F_1, F_2 are zero. Also, assume that the stress state corresponds to the principal stresses, so σ_{12} vanishes. Then Eq. 3-22 becomes:

$$f = F_{11}{}^t\sigma_1{}^2 + 2F_{12}{}^t\sigma_1{}^t\sigma_2 + F_{22}{}^t\sigma_2{}^2 = 1 \tag{3-34}$$

Comparing Eqs. 3-33 and 3-34 and recalling the stability criterion for F_{12} given by Eq. 3-24 suggests the following form for F_{12}:

$$F_{12} = -\tfrac{1}{2}\sqrt{F_{11}F_{22}} \tag{3-35}$$

This last expression was used to compute F_{12} in the present study.

The identification of the failure mode is not provided by the Tsai-Wu criterion, which predicts only the state of stress or strain resulting in failure. However, the failure mode can be deduced by considering which components of the tensor polynomial make the largest contribution to f. Ignoring the interaction term F_{12}, the remaining terms in Eq. 3-22 can be grouped as follows and associated with a particular failure mode:

$$f_F = F_1{}^t\sigma_1 + F_{11}{}^t\sigma_1{}^2 \qquad \text{fiber failure mode}$$

$$f_M = F_2{}^t\sigma_2 + F_{22}{}^t\sigma_2{}^2 \qquad \text{matrix failure mode}$$

$$f_S = F_{66}{}^t\sigma_6{}^2 \qquad \text{shear failure mode}$$

Then $f({}^t\boldsymbol{\sigma}, \mathbf{F}) = f_F + f_M + f_S$, and $\max\{f_F, f_M, f_S\}$ identifies the failure mode.

3.2 Damage Constitutive Model

In the previous section certain failure criteria were presented to predict the onset of material failure and the associated failure mode. That information is used now to model the subsequent constitutive behavior of the damaged material. First, assume the undamaged material is linearly elastic and orthotropic with respect to the principal material directions. Then for the case of plane stress, the incremental stress-strain relations are $\boldsymbol{\sigma} = \mathbf{Q}\boldsymbol{\epsilon}$, where $\mathbf{Q}$ is the reduced stiffness matrix (see Appendix F):

$$\mathbf{Q} = \begin{bmatrix} E_1/D & \nu_{21}E_1/D & 0 \\ \nu_{12}E_2/D & E_2/D & 0 \\ 0 & 0 & G_{12} \end{bmatrix} \tag{3-36}$$

where $D = 1 - \nu_{12}\nu_{21}$. In the following subsections, two models are presented for predicting the damaged material properties E_α and G_{12}, which are then used to form the damaged stiffness matrix, $\mathbf{Q}^D$. Only in-plane damage modes are considered in the present study, corresponding to the failure modes that can be predicted by the failure criteria presented in the last section: fiber failure, matrix failure, and shear failure. Failure modes associated with transverse shear or delamination are not considered in the present study.

3.2.1 Ply Discount Model

The ply discount model is a simple model that assumes the ply unloads completely after failure in the direction associated with the failure. Much of the previous work using this model was reviewed in Section 1.2. The use of the discount model was modified in the present work in that the damage model is applied at a material point within the ply thickness; it is possible that only a portion of the ply thickness may be damaged. However the name is used herein to relate the method to previous work of the same nature.

The unloading process occurs immediately and is irreversible, and is simulated by setting certain material stiffnesses (moduli) to zero when an associated failure mode is detected. The interaction between normal stress components is assumed to vanish ($\nu_{12} = 0$) for both failure modes associated with in-plane normal stresses and shear stresses. The damage models for the three failure modes considered in the present study are listed below:

fiber failure mode: $E_1 = E_2 = G_{12} = \nu_{12} = 0$

$$\mathbf{Q}^D = \begin{bmatrix} 0 & 0 & 0 \\ 0 & 0 & 0 \\ 0 & 0 & 0 \end{bmatrix} \tag{3-37}$$

matrix failure mode: $E_2 = G_{12} = \nu_{12} = 0$

$$\mathbf{Q}^D = \begin{bmatrix} E_1 & 0 & 0 \\ 0 & 0 & 0 \\ 0 & 0 & 0 \end{bmatrix} \tag{3-38}$$

shear failure mode: $E_2 = G_{12} = \nu_{12} = 0$

$$\mathbf{Q}^D = \begin{bmatrix} E_1 & 0 & 0 \\ 0 & 0 & 0 \\ 0 & 0 & 0 \end{bmatrix} \tag{3-39}$$

3.2.2 Statistical Strength Model

The statistical strength model assumes that the stiffness loss associated with fiber tensile failure is proportional to the probability of fiber failure, an idea originally proposed by Chang [1987a, 1987b]. The stiffness loss associated with other failure modes is assumed to be the same as for the ply discount method. Rosen's [1965] "weakest-link" fiber failure model was used to determine the probability of failure of a fiber bundle. Rosen models the fiber as a chain of fiber bundles and assumes the fiber fails when the weakest fiber bundle fails. The fiber strength distribution can be determined experimentally, and an inverse method is used to find the strength distribution of an individual fiber bundle. Details of Rosen's statistical analysis of the fiber bundle strength are included in Appendix G.

Now we assume that the material stiffness associated with the fiber direction will deteriorate proportionally to the number of damaged fibers, and use the result from Appendix G for the probability of failure of a fiber bundle:

$$F({}^t\sigma_1) = 1 - \exp\left(-\left(\frac{{}^t\sigma_1}{\sigma_0}\right)^{\beta}\right) \tag{3-40}$$

where σ_0, β are experimentally determined statistical parameters of the Weibull distribution [Weibull, 1951] used to model the fiber bundle strength. The mechanical properties E_1, G_{12} are degraded using the same distribution:

$$\begin{aligned} E_1^D &= E_1 \exp\left(-\left(\frac{{}^t\sigma_1}{\sigma_0}\right)^{\beta}\right) \\ G_{12}^D &= G_{12} \exp\left(-\left(\frac{{}^t\sigma_1}{\sigma_0}\right)^{\beta}\right) \end{aligned} \tag{3-41}$$

where E_1^D, G_{12}^D denote the damaged material properties. Finally, the damaged stiffness matrix is obtained by using E_1^D, G_{12}^D in Eq. 3-37, and assuming the interaction between normal stress components vanishes:

fiber failure mode: $E_1 = E_1^D, G_{12} = G_{12}^D,\ \nu_{12} = 0$

$$\mathbf{Q}^D = \begin{bmatrix} E_1^D & 0 & 0 \\ 0 & E_2 & 0 \\ 0 & 0 & G_{12}^D \end{bmatrix} \tag{3-42}$$

CHAPTER 4
FINITE ELEMENT FORMULATION

An approximate solution to the nonlinear shell equations is sought via the finite element method (*e.g.*, see [Bathe, 1982], [Zienkiewicz, 1977]). The solution domain is divided into a number of "elements" and an approximate solution is obtained over the element domain. Equilibrium and continuity are enforced by "assembling" the element solutions for the entire structural model. This chapter presents a derivation of the equations for the shell element used to model the structure. For the sake of brevity, the element equations are derived herein using a symbolic matrix notation.

In the present study, the structure is limited to thin, curved structures that can be modeled by shell finite elements, including built-up structures such as stiffened panels. In Section 4.1, the finite element approximations for a thin, curved shell are developed based on kinematic assumptions analogous to the Reissner-Mindlin theory for flat plates ([Reissner, 1944 and 1945] and [Mindlin, 1951]). The finite element matrix equations are derived from the resultant form of the principle of virtual work in Section 4.2. The numerical integration of the element equations is discussed in Section 4.3. The transformation of the element equations to the nodal reference frame is derived in Section 4.4. The solution of the nonlinear algebraic equations via the Newton-Raphson method is covered in Section 4.5.

4.1 Finite Element Approximation

The curved, quadrilateral shell element used in the analysis possesses the following characteristics:

(1) the element deformation is described by a first-order shear-deformation theory,

(2) the kinematic variables possess C^0 continuity,

(3) an isoparametric formulation is employed in which both the deformation and geometry approximations use the same interpolating functions.

This element was selected due to its computational simplicity and ability to capture shear deformation effects which may be significant for composite structures. The kinematic assumptions for a first-order shear deformation theory allow the use of a C^0 element formulation, which admits the use of Lagrangian interpolation for the kinematic variables.

The finite element equations are derived from the resultant form of the linearized, incremental form of the principle of virtual work:

$$\mathcal{K}^{matl} + {}^{t}\mathcal{K}^{geom} = {}^{t+\Delta t}\mathcal{F}^{ext} - {}^{t}\mathcal{F}^{int} \tag{4-1}$$

where $\mathcal{K}^{matl}, \mathcal{K}^{geom}, \mathcal{F}^{int}$ are variational operators derived in Chapter 2.4.3:

$$\begin{aligned} \mathcal{K}^{matl} &= \int_{{}^{t}S_e} \delta\hat{\mathbf{e}}^T \hat{\mathbf{C}}\, \hat{\mathbf{e}}\, {}^{t}dS \\ \mathcal{K}^{geom} &= \int_{{}^{t}S_e} \mathbf{g}_i^T \hat{\mathbf{s}}\, \mathbf{g}_i\, {}^{t}dS \\ \mathcal{F}^{int} &= \int_{{}^{t}S_e} \delta\hat{\mathbf{e}}^T \hat{\mathbf{N}}\, {}^{t}dS \end{aligned} \tag{4-2}$$

The variational operators are evaluated on the element domain ${}^{t}S_e$ at time t. All quantities are referred to this configuration unless otherwise stated. The left hand side of Eq. 4-1 represents the virtual work due to actual stresses acting through

(incremental) virtual strains; the right hand side represents an "out-of-balance" virtual work term resulting from the difference between the virtual work due to applied forces and that due to internal stresses.

4.1.1 Geometric Approximation

The shell geometry is defined by a reference surface and the normal to the reference surface (*cf.* Eq. 2.25):

$$\mathbf{x} = \sum_{a=1}^{nen} (\overline{\mathbf{x}}^a + \overline{z}\,\widehat{\mathbf{x}}^a) N_a \tag{4-3}$$

where nen is the number of element nodes, $\overline{\mathbf{x}}^a$ are the nodal coordinates defining the reference surface, $\widehat{\mathbf{x}}^a$ are the components of the vector normal to the reference surface at node a, and $\overline{z}$ is the through-thickness coordinate measured along $\widehat{\mathbf{x}}^a$:

$$\overline{z} = z + z_{ref} \tag{4-4}$$

where z_{ref} defines the eccentricity between the reference surface and the shell midsurface. The Lagrangian interpolation functions, $N_a(\xi_1, \xi_2)$, map the three-dimensional surface to a two-dimensional "master" element as illustrated in Fig. 4.1. The ξ_α coordinates of the master element define the surface-oriented coordinates of the (discretized) reference surface:

$$\boldsymbol{\epsilon}_\alpha = \frac{\partial \mathbf{x}}{\partial \xi_\alpha} = \sum_{a=1}^{nen} \overline{\mathbf{x}}^a \frac{\partial N}{\partial \xi_\alpha} \tag{4-5}$$

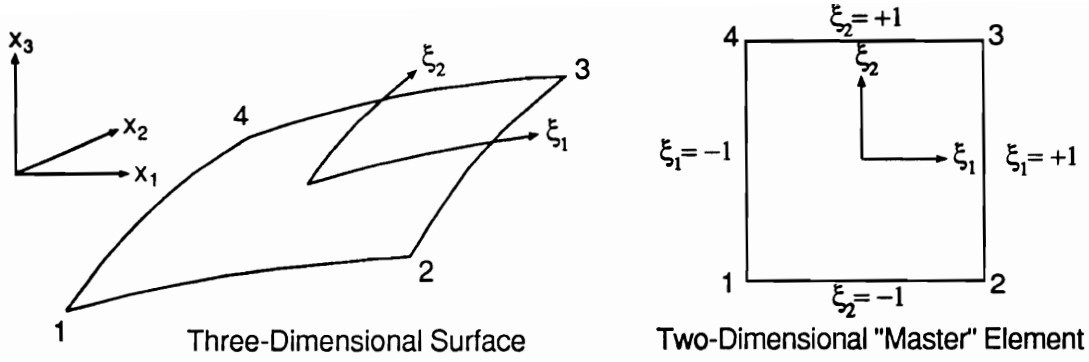

Fig. 4.1 Mapping of 3D Surface to 2D "Master" Element

4.1.2 Kinematic Approximation

In Section 2.4.1 the shell kinematics were described by the incremental midsurface displacements, $\overline{\mathbf{u}}$, and relative displacements of the shell normal $\widehat{\mathbf{u}}$ (*cf.* Eq. 2.28):

$$\begin{aligned} u_i &= \overline{u}_i + \overline{z}\widehat{u}_i \\ \mathbf{u} &= \overline{\mathbf{u}} + \overline{z}\widehat{\mathbf{u}} \end{aligned} \tag{4-6}$$

The kinematic relationships may be expressed in a convenient matrix form as:

$$\mathbf{u} = \mathbf{Z}^{(U)}\mathbf{d} \tag{4-7}$$

where

$$\mathbf{Z}^{(U)} = [\mathbf{I}_3 \ \overline{z}\mathbf{I}_3] \tag{4-8}$$

and $\mathbf{d}$ is the vector of kinematic variables

$$\mathbf{d} = \left\{ \begin{array}{c} \overline{\mathbf{u}} \\ \widehat{\mathbf{u}} \end{array} \right\}, \qquad \overline{\mathbf{u}} = \left\{ \begin{array}{c} \overline{u}_1 \\ \overline{u}_2 \\ \overline{u}_3 \end{array} \right\}, \qquad \widehat{\mathbf{u}} = \left\{ \begin{array}{c} \widehat{u}_1 \\ \widehat{u}_2 \\ \widehat{u}_3 \end{array} \right\} \tag{4-9}$$

In the isoparametric finite element formulation both the geometry and kinematic variables are approximated by the same order interpolation functions. Thus the kinematic variables are approximated by:

$$\begin{aligned} \overline{\mathbf{u}} &= \sum_{a=1}^{nen} N_a \overline{\mathbf{u}}^a \\ \widehat{\mathbf{u}} &= \sum_{a=1}^{nen} N_a \widehat{\mathbf{u}}^a \end{aligned} \tag{4-10}$$

where $\overline{\mathbf{u}}^a$, $\widehat{\mathbf{u}}^a$ are the incremental midsurface and relative displacements at node a. The kinematic variables can be written in a compact matrix form that will be used extensively in the sequel:

$$\mathbf{d} = \mathbf{N}\mathbf{q} \tag{4-11}$$

where $\mathbf{N}$ is an interpolation matrix

$$\mathbf{N} = \begin{bmatrix} N_1\mathbf{I}_6 & N_2\mathbf{I}_6 & \dots & N_1\mathbf{I}_6 \end{bmatrix} \tag{4-12}$$

and $\mathbf{q}$ is the vector of *element* kinematic variables:

$$\mathbf{q}^T = (\mathbf{d}_1^T \ \mathbf{d}_2^T \ \dots \ \mathbf{d}_N^T) \tag{4-13}$$

in which $\mathbf{d}_a$ are the *nodal* kinematic variables:

$$\mathbf{d}_a = \begin{Bmatrix} \overline{\mathbf{u}}^a \\ \widehat{\mathbf{u}}^a \end{Bmatrix}, \qquad \overline{\mathbf{u}}^a = \begin{Bmatrix} \overline{u}_1^a \\ \overline{u}_2^a \\ \overline{u}_3^a \end{Bmatrix}, \qquad \widehat{\mathbf{u}}^a = \begin{Bmatrix} \widehat{u}_1^a \\ \widehat{u}_2^a \\ \widehat{u}_3^a \end{Bmatrix}, \qquad a = 1, 2, \dots, nen \tag{4-14}$$

4.1.3 Strain Measures

The strain-displacement relations for the linear strain measures and curvatures can be written as

$$\begin{aligned} \mathbf{e}^0 &= \mathbf{L}_e\mathbf{d} \\ \boldsymbol{\kappa} &= \mathbf{L}_\kappa\mathbf{d} \\ \boldsymbol{\gamma} &= \mathbf{L}_\gamma\mathbf{d} \end{aligned} \tag{4-15}$$

where $\mathbf{L}_e, \mathbf{L}_\kappa, \mathbf{L}_\gamma$ are matrices of linear differential operators

$$\mathbf{L}_e = \begin{bmatrix} \partial/\partial x_1^\ell & 0 & 0 & 0 & 0 & 0 \\ 0 & \partial/\partial x_2^\ell & 0 & 0 & 0 & 0 \\ \partial/\partial x_2^\ell & \partial/\partial x_1^\ell & 0 & 0 & 0 & 0 \end{bmatrix}$$

$$\mathbf{L}_\kappa = \begin{bmatrix} 0 & 0 & 0 & \partial/\partial x_1^\ell & 0 & 0 \\ 0 & 0 & 0 & 0 & \partial/\partial x_2^\ell & 0 \\ 0 & 0 & 0 & \partial/\partial x_2^\ell & \partial/\partial x_1^\ell & 0 \end{bmatrix} \tag{4-16}$$

$$\mathbf{L}_\gamma = \begin{bmatrix} 0 & 0 & \partial/\partial x_1^\ell & 1 & 0 & 0 \\ 0 & 0 & \partial/\partial x_2^\ell & 0 & 1 & 0 \end{bmatrix}$$

Recall that the gradient operator is referred to a local coordinate system, $\mathbf{x}_i^\ell$, that is tangent to the shell surface defined by ζ=constant. However, the derivatives of the interpolation functions are most naturally computed with respect to the isoparametric coordinates ξ_α that define the "master" element. The transformation between the isoparametric and local reference frame takes the same form as the Jacobian transformation derived in Section 2.4.2:

$$\begin{Bmatrix} \partial/\partial x_1^\ell \\ \partial/\partial x_2^\ell \end{Bmatrix} = \left[J^0\right]^{-T} \begin{Bmatrix} \partial/\partial \xi_1 \\ \partial/\partial \xi_2 \end{Bmatrix} \tag{4-17}$$

where $\mathbf{J}^0$ is the surface Jacobian matrix (Eq. 2-45).

The strain-displacement relations in Eq. 4-16 can be expressed more compactly as

$$\hat{\boldsymbol{\epsilon}} = \begin{Bmatrix} \mathbf{e}^0 \\ \boldsymbol{\kappa} \\ \boldsymbol{\gamma} \end{Bmatrix} = \mathbf{L}\mathbf{d} \tag{4-18}$$

where

$$\mathbf{L} = \begin{bmatrix} \mathbf{L}_e \\ \mathbf{L}_\kappa \\ \mathbf{L}_\gamma \end{bmatrix} \tag{4-19}$$

Substituting Eq. 4-12 in Eq. 4-18 gives the strain-displacement relations in terms of the nodal displacements

$$\hat{\boldsymbol{\epsilon}} = \mathbf{L}\mathbf{N}\mathbf{q} = \mathbf{B}_L\mathbf{q} \tag{4-20}$$

where the matrix $\mathbf{B}_L = \mathbf{L}\mathbf{N}$ contains derivatives of the interpolation functions.

4.1.4 Deformation Gradient

The deformation gradient appears in the geometric stiffness operator and was introduced in Section 2.4.3 using:

$$\tilde{\mathbf{g}}_i^T = (\overline{u}_{i,1}\ \overline{u}_{i,2}) \tag{4-21}$$

Define a deformation gradient vector, $\mathbf{g}$, that contains components of the deformation gradient:

$$\mathbf{g}^T = \{\overline{u}_{1,1}\ \overline{u}_{1,2}\ \overline{u}_{2,1}\ \overline{u}_{2,2}\ \overline{u}_{3,1}\ \overline{u}_{3,2}\ \} \tag{4-22}$$

or

$$\mathbf{g} = \mathbf{L}_g \mathbf{d} \tag{4-23}$$

where

$$\mathbf{L}_g = \begin{bmatrix} \partial/\partial x_1^\ell & 0 & 0 & 0 & 0 & 0 \\ \partial/\partial x_2^\ell & 0 & 0 & 0 & 0 & 0 \\ 0 & \partial/\partial x_1^\ell & 0 & 0 & 0 & 0 \\ 0 & \partial/\partial x_2^\ell & 0 & 0 & 0 & 0 \\ 0 & 0 & \partial/\partial x_1^\ell & 0 & 0 & 0 \\ 0 & 0 & \partial/\partial x_2^\ell & 0 & 0 & 0 \end{bmatrix} \tag{4-24}$$

Then the finite element approximation for the deformation gradient vector is obtained by substituting Eq. 4-10 in Eq. 4-23:

$$\mathbf{g} = \mathbf{L}_g \mathbf{N} \mathbf{q} = \mathcal{G} \mathbf{q} \tag{4-25}$$

where the matrix $\mathcal{G} = \mathbf{L}_g \mathbf{N}$ contains derivatives of the interpolation functions.

4.2 Finite Element Matrices

The finite element equations are obtained by substituting the finite element approximation for the strain tensor and deformation gradient in the variational operators:

$$\delta\hat{\mathbf{e}} = \mathbf{B}_L\,\delta\mathbf{q} \tag{4-26}$$

$$\mathbf{g} = \mathcal{G}\,\delta\mathbf{q} \tag{4-27}$$

Each of the variational operators is considered separately in the following subsections.

4.2.1 Material Stiffness Matrix

The material stiffness variational operator was derived in Section 2.4.3:

$$\mathcal{K}^{matl} = \int_{{}^tS^e} \delta\hat{\mathbf{e}}^T\,\widehat{\mathbf{C}}\,\hat{\mathbf{e}}\,{}^tdS^e \tag{4-28}$$

The finite element approximation is obtained by substituting the strain-displacement relationships Eq. 4-26, which leads to:

$$\mathcal{K}^{matl} = \int_{{}^tS^e} \delta\mathbf{q}^T\mathbf{B}_L^T\widehat{\mathbf{C}}\mathbf{B}_L\mathbf{q}\,{}^tdS^e \tag{4-29}$$

The vector $\mathbf{q}$ contains independent element DOFs and can moved outside the integral. Then the material stiffness operator becomes:

$$\mathcal{K}^{matl} = \delta\mathbf{q}^T\mathbf{K}^{matl}\mathbf{q} \tag{4-30}$$

where $\mathbf{K}^{matl}$ is the finite element material stiffness matrix

$$\mathbf{K}^{matl} = \int_{{}^tS^e} \mathbf{B}_L^T\widehat{\mathbf{C}}\mathbf{B}_L\,{}^tdS^e \tag{4-31}$$

4.2.2 Geometric Stiffness Matrix

The geometric stiffness variational operator was derived in Section 2.4.3, and is rewritten here in terms of the deformation gradient vector **g**:

$$\mathcal{K}^{geom} = \int_{{}^tS^e} \delta\mathbf{g}^T \boldsymbol{\mathcal{N}} \mathbf{g}\, {}^tdS^e \tag{4-32}$$

where $\boldsymbol{\mathcal{N}}$ contains the stress resultant matrix **n** (Eq. 2-72) on diagonal partitions:

$$\boldsymbol{\mathcal{N}} = \begin{bmatrix} \mathbf{n} & \mathbf{0} & \mathbf{0} \\ \mathbf{0} & \mathbf{n} & \mathbf{0} \\ \mathbf{0} & \mathbf{0} & \mathbf{n} \end{bmatrix} \tag{4-33}$$

The finite element approximation is obtained by substituting the gradient-displacement relationships Eq. 4-27, which leads to:

$$\mathcal{K}^{geom} = \int_{{}^tS^e} \delta\mathbf{q}^T \boldsymbol{\mathcal{G}}^T \boldsymbol{\mathcal{N}} \boldsymbol{\mathcal{G}} \mathbf{q}\, {}^tdS^e \tag{4-34}$$

The vector **q** contains independent element DOFs and can be moved outside the integral. Then the geometric stiffness operator becomes:

$$\mathcal{K}^{geom} = \delta\mathbf{q}^T \mathbf{K}^{geom} \mathbf{q} \tag{4-35}$$

where $\mathbf{K}^{geom}$ is the finite element geometric stiffness matrix

$$\mathbf{K}^{geom} = \int_{{}^tS^e} \boldsymbol{\mathcal{G}}^T \boldsymbol{\mathcal{N}} \boldsymbol{\mathcal{G}}\, {}^tdS^e \tag{4-36}$$

4.2.3 External Force Vector

Surface tractions and body loads were not considered in the present study and a simplified form was assumed for the external force variational operator:

$$\mathcal{F}^{ext} = \mathbf{q}^T \mathbf{F}^{ext} \tag{4-37}$$

where $\mathbf{F}^{ext}$ are nodal forces that are energetically conjugant to **q**.

4.2.4 Internal Force Vector

The internal force variational operator was derived in Section 2.4.3:

$$\mathcal{F}^{int} = \int_{{}^tS^e} \delta\hat{\mathbf{e}}^T \widehat{\mathbf{N}}\, {}^tdS^e \tag{4-38}$$

The finite element approximation is obtained by substituting the strain-displacement relationships Eq. 4-25, which leads to:

$$\mathcal{F}^{int} = \int_{{}^tS^e} \delta\mathbf{q}^T \mathbf{B}_L^T \widehat{\mathbf{N}}\, {}^tdS^e \tag{4-39}$$

The vector $\mathbf{q}$ contains independent element DOFs and can be moved outside the integral. Then the internal force operator becomes:

$$\mathcal{F}^{int} = \delta\mathbf{q}^T \mathbf{F}^{int} \tag{4-40}$$

where $\mathbf{F}^{int}$ is the finite element internal force vector

$$\mathbf{F}^{int} = \int_{{}^tS^e} \mathbf{B}_L^T \widehat{\mathbf{N}}\, {}^tdS^e \tag{4-41}$$

4.2.5 Finite Element Equations

The finite element approximation to the principle of virtual work can now be written as:

$$\delta\mathbf{q}^T \mathbf{K}^{matl}\mathbf{q} + \delta\mathbf{q}^T \mathbf{K}^{geom}\mathbf{q} = \delta\mathbf{q}^T \mathbf{F}^{ext} - \delta\mathbf{q}^T \mathbf{F}^{int} \tag{4-42}$$

or

$$\delta\mathbf{q}^T \Big(\big[\mathbf{K}^{matl} + \mathbf{K}^{geom}\big]\mathbf{q} = \mathbf{F}^{ext} - \mathbf{F}^{int} \Big) \tag{4-43}$$

We require that Eq. 4-43 be valid for any arbitrary, kinematically admissible $\delta\mathbf{q}$, which leads to the final form of the incremental, finite element equations for the curved, composite shell:

$$\big[\mathbf{K}^{matl} + \mathbf{K}^{geom}\big]\mathbf{q} = \mathbf{F}^{ext} - \mathbf{F}^{int} \tag{4-44}$$

4.3 Numerical Integration

The variational operators were derived based on first principles in elasticity that resulted in three dimensional integrals over the current volume. Then kinematic assumptions were introduced for the shell theory that allowed the separation of the volume integral into through-thickness and surface integrals. The quadrature formulae for the through-thickness and surface integrals are discussed next in Sections 4.3.1 and 4.3.2, respectively.

4.3.1 Through-Thickness (Constitutive) Integration

The laminate strain measures and integrated stress resultants and constitutive matrices were introduced in Section 2.4.3:

$$\begin{Bmatrix} \mathbf{N} \\ \mathbf{M} \\ \mathbf{Q} \end{Bmatrix} = \begin{bmatrix} \mathbf{A} & \mathbf{B} & \mathbf{0} \\ \mathbf{B} & \mathbf{D} & \mathbf{0} \\ \mathbf{0} & \mathbf{0} & \mathbf{H} \end{bmatrix} \begin{Bmatrix} \boldsymbol{\epsilon}^0 \\ \boldsymbol{\kappa} \\ \boldsymbol{\gamma} \end{Bmatrix} \tag{4-45}$$

where $\mathbf{N}, \mathbf{M}, \mathbf{Q}$ are the stress resultants, stress couples, and transverse shear stress resultants, respectively,

$$\begin{aligned} \mathbf{N} &= \int_h \boldsymbol{\sigma}\, dz \\ \mathbf{M} &= \int_h \boldsymbol{\sigma}\overline{z}\, dz \\ \mathbf{Q} &= \begin{Bmatrix} Q_1 \\ Q_2 \end{Bmatrix} = \int_h \begin{Bmatrix} \sigma_5 \\ \sigma_4 \end{Bmatrix} dz \end{aligned} \tag{4-46}$$

and $\mathbf{A}, \mathbf{B}, \mathbf{D}, \mathbf{H}$ are the integrated laminate stiffness coefficients for extension, extension-bending coupling, bending, and transverse shear, respectively:

$$\begin{aligned} \Big(\mathbf{A}, \mathbf{B}, \mathbf{D}\Big) &= \int_h \overline{\mathbf{Q}}(1, \overline{z}, \overline{z}^2)\, dz \\ \mathbf{H} &= \int_h \overline{\mathbf{C}}^{(S)}\, dz \end{aligned} \tag{4-47}$$

The usual technique from classical lamination theory (CLT) is to treat the integrals in Eqs. 4-46 and 4-47 as piecewise integrals over each layer, *e.g.*,

$$\mathcal{I} = \int_h f(\overline{z})\, dz = \sum_{k=1}^{nlyr} \int_{\overline{z}_{k-1}}^{\overline{z}_k} f(\overline{z})\, dz \tag{4-48}$$

where $\overline{z}_{k-1}, \overline{z}_k$ are the coordinates of the bottom and top of layer k, respectively, and $nlyr$ is the number of layers in the laminate. In CLT, $\overline{Q}$ is assumed to be constant within each layer and Eq. 4-48 can be evaluated explicitly (*e.g.*, see [Jones, 1975]). However, the presence of damage at a material point may locally degrade the ply-level constitutive matrix, thus $\overline{Q}$ is no longer constant within the layer. The integrals in the form of Eq. 4-48 were evaluated numerically using a repeated Simpson's rule [Johnson and Reiss, 1982] with n_k integration points for layer k:

$$\mathcal{I} = \sum_{k=1}^{nlyr} \int_{\overline{z}_{k-1}}^{\overline{z}_k} f(\overline{z})\, dz = \sum_{k=1}^{nlyr} \sum_{i=1}^{n_k} \frac{h_k}{3} c_{ik} f(\overline{z}_{ik}) \tag{4-49}$$

where h_k is the thickness for layer k

$$h_k = \frac{\overline{z}_k - \overline{z}_{k-1}}{n_k - 1} \tag{4-50}$$

and c_{ik}, z_{ik} are the quadrature weights and coordinates, respectively, associated with node i in the layer-wise integrations:

$$\overline{z}_{ik} = \overline{z}_{k-1} + (i-1)h_k$$

$$c_{ik} = \begin{cases} 1 & \text{if } i = 1 \text{ or } n_k; \\ 2 & \text{if } i \text{ is odd, } i \neq 1, n_k; \\ 4 & \text{if } i \text{ is even.} \end{cases}$$

The number of integration points, n_k, must be odd and greater than or equal to three. The index k on the weights and nodes of the quadrature formula implies that a different number of quadrature nodes may be used in each layer.

4.3.2 Two-Dimensional (Element) Integration

The components of the stiffness matrices and force vectors were expressed as two-dimensional integrals over the element reference surface that can be expressed in the general form

$$\mathcal{I} = \int_{\Omega_e} f(x_1^\ell, x_2^\ell)\, dx_1^\ell\, dx_2^\ell \tag{4-51}$$

where f is a scalar that is evaluated in the (local) x_α^ℓ reference frame. The finite element approximation of the reference surface maps the three-dimensional reference surface to the two-dimensional "master element" surface described by the isoparametric ξ_α-coordinates (see Fig. 4.1). Then the generic integral given by Eq. 4-51 can be written as:

$$\mathcal{I} = \int_{-1}^{1}\int_{-1}^{1} f\big(x_1^\ell(\xi_\alpha), x_2^\ell(\xi_\alpha)\big)|\mathbf{J}^0|\, d\xi_1\, d\xi_2 \tag{4-52}$$

where

$$dx_1^\ell\, dx_2^\ell = |\mathbf{J}^0|\, d\xi_1\, d\xi_2 \tag{4-53}$$

and $|\mathbf{J}^0|$ is the determinant of the surface Jacobian matrix, Eq. 2.45. Let $\hat{f}(\xi_1, \xi_2) = |\mathbf{J}^0| f\big((x_1^\ell(\xi_\alpha), x_2^\ell(\xi_\alpha)\big)$, so the generic integral becomes

$$\mathcal{I} = \int_{-1}^{1}\int_{-1}^{1} \hat{f}(\xi_1, \xi_2)\, d\xi_1\, d\xi_2 \tag{4-54}$$

The double integral in Eq. 4-54 can be computed using two nested one-dimensional quadrature rules:

$$\begin{aligned}
\mathcal{I} &= \int_{-1}^{1} \left(\int_{-1}^{1} \hat{f}(\xi_1, \xi_2)\, d\xi_1 \right) d\xi_2 \\
&= \int_{-1}^{1} \left(\sum_{i=1}^{L} w_i \hat{f}(\xi_i, \xi_2) \right) d\xi_2 \\
&= \sum_{j=1}^{M}\sum_{i=1}^{L} w_j w_i \hat{f}(\xi_i, \xi_j)
\end{aligned} \tag{4-55}$$

where L, M are the number of quadrature nodes in the ξ_1-, ξ_2-directions, respectively (usually $L = M$), and w_i, ξ_i are the weights and coordinates associated with node i. Gaussian quadrature was used to compute the element matrices; the quadrature weights and coordinates are listed in Table 4.1 for different order quadrature formulae. The one-dimensional Gauss quadrature rule requires M nodes to exactly integrate a polynomial of order p [Reddy, 1984], where

$$M = \begin{cases} (\text{p+1})/2 & \text{if } p \text{ is odd} \\ \text{p}/2+1 & \text{if } p \text{ is even} \end{cases} \tag{4-56}$$

A 2×2 quadrature rule was used for the 4-node quadrilateral element, a 3×3 quadrature rule was used for the 9-node element, *etc.*

Table 4.1 Nodal Coordinates and Weights for Gaussian Quadrature

N	Nodal Coordinates ξ_i	Weight Coefficients w_i
1	0.000000000000000	2.000000000000000
2	± 0.577350269189626	1.000000000000000
3	± 0.774596669241483	0.555555555555556
	0.000000000000000	0.888888888888889
4	± 0.861136311594053	0.347854845137454
	± 0.339981043584856	0.652145154862546

4.3.3 Selective Reduced Integration

Shear deformable shell elements become overly stiff as the shell becomes thin. This locking behavior has been widely studied, see [Averill, 1989] for an excellent review. Selective reduced integration has been used on membrane and transverse-shear stiffness terms to avoid locking. Using this approach, selected terms in the strain-displacement matrix, $\mathbf{B}_L$, are treated with a reduced integration rule. The

method presented by Hughes [1987] was used in the present study and is described next.

Let b be a typical term in $\mathbf{B}_L$ that is to be replaced by its reduced quadrature counterpart, $\overline{b}$. The reduced quadrature rule is defined by $\overline{N}$ nodes with coordinates $\overline{\xi}_i, \overline{\eta}_i$. A special set of shape functions is defined with nodes at the reduced quadrature points:

$$N_i(\overline{\xi}_j, \overline{\eta}_j) = \delta_{ij}, \qquad 1 \leq i, j \leq \overline{N} \tag{4-57}$$

The reduced quadrature term, $\overline{b}$, is obtained by extrapolating b—evaluated at the reduced quadrature nodes—to the normal quadrature nodes:

$$\overline{b}(\xi, \eta) = \sum_{i=1}^{\overline{N}} N(\xi, \eta) b(\overline{\xi}_i, \overline{\eta}_i) \tag{4-58}$$

The membrane- and transverse-shear terms in $\mathbf{B}_L$ were selectively under-integrated using $\overline{N} = (M-1)(M-1)$, where M is the order of the (one-dimensional) normal quadrature rule.

4.4 Finite Element Transformations

In many structural applications, the geometry will be described by a general, three-dimensional curvilinear coordinate system (*e.g.*, cylindrical or spherical), and boundary conditions and loads are most naturally specified in this system. In order for the finite element analysis to correctly model these boundary conditions and loads, it is necessary to transform the finite element equations to the local reference frame associated with each node, herein referred to as the computational reference frame.

We also want to transform the element equations to a "standard" form (possessing rotational degrees of freedom, θ_i) by making use of the rotational equivalence of the shell relative displacements, $\widehat{u}_i$. This was necessary to implement the element in the CSM Testbed via the Generic Element Processor (GEP, see [Stanley and Nour-Omid, 1990]), used for the numerical experiments in the present study. The GEP expects elements to possess the standard shell degrees of freedom, $\mathbf{d}^T = (\overline{u}_i\ \theta_i)$.

Both these transformations can be completed effectively at the element level. Let $\boldsymbol{\epsilon}_i$ be the element intrinsic basis vectors, and $\boldsymbol{\epsilon}_i^a$ be the computational basis vectors at node a. The transformation between the element and computational bases is given by $\mathbf{b} = \mathbf{t}^a \mathbf{b}^C$, where the superscript C indicates a quantity referred to the computational basis, superscript a denotes node a, and $\mathbf{t}^a$ is the transformation matrix $t_{ij}^a = \boldsymbol{\epsilon}_i \cdot \boldsymbol{\epsilon}_j^a$.

The kinematic variables transform as:

$$\overline{\mathbf{u}}^a = \mathbf{t}^a \overline{\mathbf{u}}^{aC} \tag{4-59}$$

$$\widehat{\mathbf{u}}^a = \boldsymbol{\chi} \mathbf{t}^a \boldsymbol{\theta}^C \tag{4-60}$$

where $\boldsymbol{\chi}$ is the skew-symmetric matrix defined by Eq. 2-36. Note that Eq. 4-60 is identical to the expression of rotational equivalence expressed by Eq. 2-35, except that the pseudonormal basis has been replaced by the computational basis at node a [Stanley, 1985].

The transformation of the *nodal* kinematic variables can be expressed compactly as:

$$\mathbf{d}_a = \mathbf{L}^a \mathbf{d}_a^C$$

where

$$\mathbf{L}^a = \begin{bmatrix} \mathbf{t}^a & \mathbf{0} \\ \mathbf{0} & \boldsymbol{\chi}\mathbf{t}^a \end{bmatrix} \tag{4-61}$$

The transformation for all the *element* kinematic variables can be constructed as:

$$\mathbf{q} = \mathbf{T}\mathbf{q}^C \tag{4-62}$$

where

$$\mathbf{T} = \begin{bmatrix} \mathbf{L}^1 & \mathbf{0} & \dots & \mathbf{0} \\ \mathbf{0} & \mathbf{L}^2 & \dots & \mathbf{0} \\ \vdots & \vdots & \ddots & \vdots \\ \mathbf{0} & \mathbf{0} & \dots & \mathbf{L}^{nen} \end{bmatrix} \tag{4-63}$$

The transformation of the element matrices is obtained by requiring that the incremental virtual work be invariant with respect to the choice of the reference frame [Zienciewicz, 1977]. This requirement can be achieved by applying the element transformation, Eq. 4-62, to each term in the variational statement given by Eq. 4-42. Starting with the stiffness terms on the left hand side of Eq. 4-42, the invariance of the variational statement can be expressed as:

$$\delta\mathbf{q}^{C^T}\overline{\mathbf{K}}\delta\mathbf{q}^C = \delta\mathbf{q}^T\mathbf{K}\delta\mathbf{q} \tag{4-64}$$

where $\mathbf{K}$ is either $\mathbf{K}^{matl}$ or $\mathbf{K}^{geom}$, and the overbar indicates the matrix is referred to the computational basis. Substituting Eq. 4-62 in 4-64 yields

$$\delta\mathbf{q}^{C^T}\underline{\overline{\mathbf{K}}}\delta\mathbf{q}^C = \delta\mathbf{q}^{C^T}\underline{\mathbf{T}^T\mathbf{K}\mathbf{T}}\delta\mathbf{q}^C \tag{4-65}$$

The underlined terms must be equal which yields the transformation relationship for the stiffness matrix:

$$\overline{\mathbf{K}} = \mathbf{T}^T\mathbf{K}\mathbf{T} \tag{4-66}$$

The "out-of-balance forces" on the right hand side of Eq. 4-42 are transformed in a similar manner. The invariance of the variational statement is expressed as:

$$\delta\mathbf{q}^{C^T}\overline{\mathbf{F}} = \delta\mathbf{q}^T\mathbf{F} \tag{4-67}$$

where $\mathbf{F}$ is either $\mathbf{F}^{ext}$ or $\mathbf{F}^{int}$, and the overbar indicates the vector is referred to the computational basis. Substituting Eq. 4-62 in 4-67 yields

$$\delta\mathbf{q}^{C^T}\underline{\overline{\mathbf{F}}} = \delta\mathbf{q}^{C^T}\underline{\mathbf{T}^T\mathbf{F}} \tag{4-68}$$

and once again the underlined terms must be equal which yields the transformation relationship for the force vector:

$$\overline{\mathbf{F}} = \mathbf{T}^T\mathbf{F} \tag{4-69}$$

Finally, note that $\mathbf{T}$ is a sparse matrix composed of 3×3 matrix partitions on the diagonal. Let $\mathbf{K}^{ab}$ be the 6×6 matrix partition (or nodal block) relating the forces at node a to the kinematic variables at node b. Furthermore, let $\mathbf{k}^{ab}_{\alpha\beta}$ be the 3×3 partitions of the a,bth nodal block associated with the displacement or rotation kinematic variables, *i.e.*,

$$\begin{bmatrix} \mathbf{k}^{ab}_{11} & \mathbf{k}^{ab}_{21} \\ \mathbf{k}^{ab}_{12} & \mathbf{k}^{ab}_{22} \end{bmatrix} \begin{Bmatrix} \overline{\mathbf{u}}_b \\ \boldsymbol{\theta}_b \end{Bmatrix} = \begin{Bmatrix} \mathbf{f}^a_1 \\ \mathbf{f}^a_2 \end{Bmatrix} \qquad a,b = 1,2,\ldots,nen \tag{4-70}$$

Then the transformation equations 4-66 and 4-69 reduce to a set of efficient 3×3 matrix multiplications:

$$\overline{\mathbf{k}}^{ab}_{\alpha\beta} = (\mathbf{t}^a)^T\,\mathbf{k}^{ab}_{\alpha\beta}\mathbf{t}^b \qquad a,b = 1,2,\ldots,nen \tag{4-71}$$

$$\overline{\mathbf{f}}^a_\alpha = (\mathbf{t}^a)^T\,\mathbf{f}^a_\alpha \tag{4-72}$$

4.5 Nonlinear Solution Procedure

The finite element equations form a system of nonlinear algebraic equations, including geometrically nonlinear effects arising from large deformations and material nonlinearities due to the development of damage in the shell composite laminate. The Newton-Raphson method has been widely studied for solving systems of nonlinear equations, *e.g.*, see [Stricklin et al., 1973], [Bergan et al., 1978], [Bathe and Cimento, 1980] and [Ramm, 1980]. The method is described next, along with an automated load-stepping algorithm to optimize the solution procedure.

4.5.1 Newton-Raphson Method

The Newton-Raphson method seeks an iterative solution of the system of nonlinear equations in the form:

$$\mathbf{r}({}^{t+\Delta t}\mathbf{u}) = 0 \tag{4-73}$$

where $\mathbf{r}$ represents the equilibrium equations

$$\mathbf{r}({}^{t+\Delta t}\mathbf{u}) = \mathbf{F}^{ext}({}^{t+\Delta t}\mathbf{u}) - \mathbf{F}^{int}({}^{t+\Delta t}\mathbf{u}) \tag{4-74}$$

We assume that a previous iterate solution ${}^{t+\Delta t}\mathbf{u}^{i-1}$ is available and perform a Taylor series expansion about the previous solution:

$$\mathbf{r}({}^{t+\Delta t}\mathbf{u}) = \mathbf{r}({}^{t+\Delta t}\mathbf{u}^{i-1}) + \frac{\partial \mathbf{r}}{\partial \mathbf{u}}\Delta\mathbf{u}^i + \mathcal{O}(\Delta\mathbf{u}^i)^2 = 0 \tag{4-75}$$

where $\Delta\mathbf{u}^i$ is the displacement increment correction and we neglect the higher order terms in $\Delta\mathbf{u}^i$. The term $\partial\mathbf{r}/\partial\mathbf{u}$ is the directional derivative and in the absence of displacement-dependent external loads is related to the tangent stiffness matrix as follows:

$$\frac{\partial \mathbf{r}}{\partial \mathbf{u}}\Big|_{{}^{t+\Delta t}\mathbf{u}^{i-1}} = -\frac{\partial {}^{t+\Delta t}\mathbf{F}^{i-1}}{\partial \mathbf{u}} = -{}^{t+\Delta t}\mathbf{K}^{i-1} \tag{4-76}$$

where we introduce the shorthand notation ${}^{t+\Delta t}\mathbf{F}^{i-1}$ and ${}^{t+\Delta t}\mathbf{K}^{i-1}$ for the $i-1$ iterate of the internal force vector and tangent stiffness matrix, respectively. Substituting Eq. 5.4 in 5.3 yields:

$$ {}^{t+\Delta t}\mathbf{K}^{i-1}\Delta\mathbf{u}^{i} = {}^{t+\Delta t}\mathbf{r}^{i-1} \tag{4-77} $$

or

$$ \Delta\mathbf{u}^{i} = \left({}^{t+\Delta t}\mathbf{K}^{i-1}\right)^{-1}\left({}^{t+\Delta t}\mathbf{r}^{i-1}\right) \tag{4-78} $$

where ${}^{t+\Delta t}\mathbf{r}^{i-1}$ is the out-of-balance force vector corresponding to the configuration ${}^{t+\Delta t}\mathbf{u}^{i-1}$. The displacement increment (for the load step) is updated using

$$ {}^{t+\Delta t}\mathbf{u}^{i} = {}^{t+\Delta t}\mathbf{u}^{i-1} + \Delta\mathbf{u}^{i} \tag{4-79} $$

Equations 4-78 and 4-79 constitute the Newton-Raphson method for solving the system of nonlinear equations given by Eq. 4-74. The iteration is continued until the iterative change in displacement becomes small and equilibrium is approximately satisfied, *i.e.*, $\mathbf{F}^{ext} \approx \mathbf{F}^{int}$. An energy norm convergence criterion was used in the present study to determine when to terminate the iteration:

$$ \frac{{}^{t+\Delta t}\mathbf{r}^{i} \cdot \Delta\mathbf{u}^{i}}{U^{ref}} < \epsilon, \qquad \epsilon \ll 1 \tag{4-80} $$

where U^{ref} is the total strain energy at the start of the load step, and ϵ is typically in the range of $10^{-4} < \epsilon < 10^{-3}$.

4.5.2 Automatic Load Stepping Algorithm

Introduce a scalar load parameter λ defined as:

$$^{t}\mathbf{F}^{ext} = {}^{t}\lambda\overline{\mathbf{F}} \tag{4-81}$$

where $\overline{\mathbf{F}}$ is a "base" external load vector that is scaled by ${}^{t}\lambda$. The load parameter is updated at each step by ${}^{t+\Delta t}\lambda = {}^{t}\lambda + \Delta\lambda$, where $\Delta\lambda$ is the load step. The step size is important in determining the overall efficiency of the nonlinear solution algorithm for tracing the equilibrium path. For instance if $\Delta\lambda$ is small many steps will be required to trace the equilibrium path resulting in a large number of factorizations of the tangent stiffness matrix. Alternatively if $\Delta\lambda$ is too large many iterations may be required for the solution to converge. Ideally $\Delta\lambda$ is adjusted automatically to remove the need for manual interaction with the solution algorithm.

In Crisfield's arc-length control method [1981] the arc-length for the increment from time t to $t + \Delta t$ is computed based on a ratio of the number of iterations required to achieve convergence for the previous configuration (at time t) and the desired number of iterations specified by the user:

$$^{t+\Delta t}\Delta l = (I_D/I_A)\,{}^{t}\Delta l \tag{4-82}$$

where I_D, I_A are the desired and actual number of iterations, respectively, to achieve convergence for the configuration at time t. Usually I_D is chosen as 4 or 5. Bergan and Soreide [1977] reported that Eq. 4-82 led to oscillatory behavior of the arc-length and obtained improved results with

$$^{t+\Delta t}\Delta l = (I_D/I_A)^{\frac{1}{2}}\,{}^{t}\Delta l \tag{4-83}$$

Equation 4-83 was modified for the present study to scale the load parameter increment instead of the path length increment:

$$^{t+\Delta t}\Delta\lambda = (I_D/I_A)^{\frac{1}{2}}\,{}^{t}\Delta\lambda \tag{4-84}$$

Two other automatic step size controls were available in the nonlinear solution procedure: MAX_ITERS set the maximum number of iterations allowed during a step; and MAX_DIV limited the number of times the solution error was allowed to increase within a step to prevent the solution from diverging.[1] If either of these parameters was exceeded, the step size was halved. A maximum number of step size reductions was allowed, MAX_CUTS, after which the analysis was terminated.

[1] This parameter was set to a constant MAX_DIV=2 in the original NL_STATIC_1 nonlinear solution procedure [*Computational Structural Mechanics Testbed Procedures Manual*, 1991]; the parameter was added as a procedure argument for the present study.

CHAPTER 5
EXPERIMENTAL PROGRAM

Experimental crush tests were conducted to verify the analytical methods described in Chapters 2–4. Curved, graphite/epoxy frames, representative of ring stiffeners in rotorcraft, were crushed in quasi-static tests to determine their response to vertical, crash-type loads. The frame crushing occurred in a progressive manner, thus the experiments provided data that can be correlated with the progressive failure analysis. The frame specimens are described in Section 6.1, including detailed measurements of the frames; the test setup is discussed in Section 6.2; and Section 6.3 describes the instrumentation used in the tests.

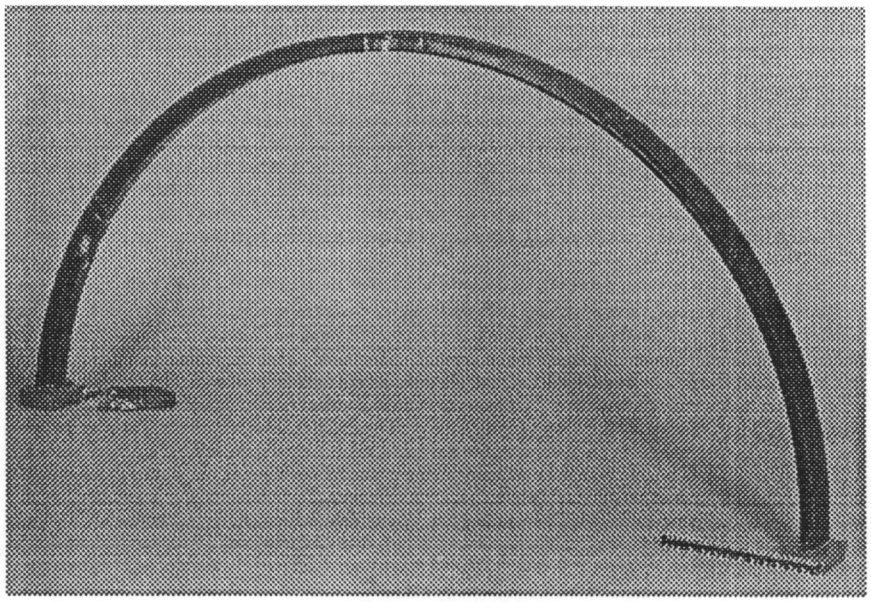

Fig. 5.1 Typical Frame Specimen

5.1 Test Specimen Description

The frames were fabricated by Skyline Industries under a subcontract from Bell Helicopter Textron, Inc. The frame cross-section, illustrated in Fig. 5.2, was constructed using two channel sections co-cured with cap plies and the skin section. The fabrication technique is illustrated in Fig. 5.3. Each channel section was formed by wrapping plies around a semicircular tool, and cap plies were added to the top and bottom of the joined channels so the flanges of the resulting I-frame would have an equal number of plies as the web. The orientation of the plies in the channel section and cap were such that the I-frame flanges were symmetric and the web was unsymmetric.

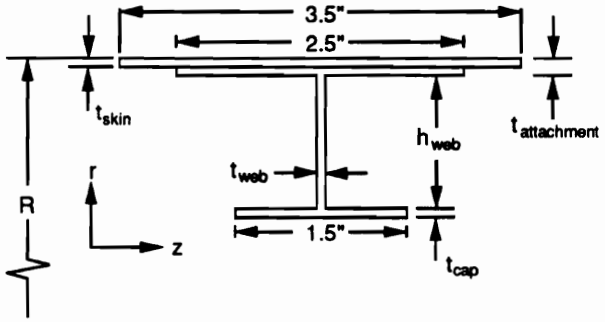

Fig. 5.2 I-Frame Cross-Section

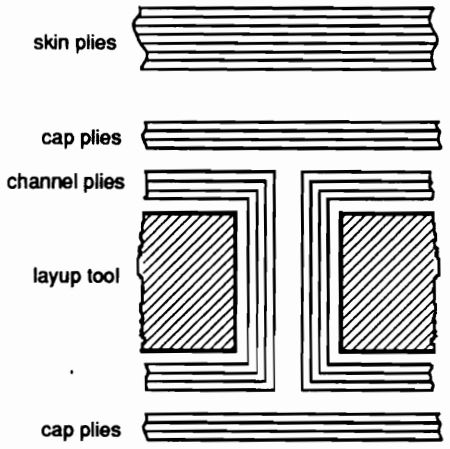

Fig. 5.3 Illustration of I-Frame Fabrication Technique

The frames were manufactured with three different configurations of laminate stacking sequences for the web and flanges, as listed in Table 5.1. The skin's laminate stacking sequence for all specimens was a quasi-isotropic layup: $[\pm 45/0/90]_{2S}$. The ply orientation was specified relative to the frame's circumferential direction, *i.e.*, 0° plies ran circumferentially.

Table 5.1 Laminate Stacking Sequence for the Frame Flange and Web

Frame ID	Flange	Web
FR001I/4I	$[\pm 45/0/90]_S$	$[\pm 45/0/90_2/0/\pm 45]$
FR002I/5I	$[\pm 45/0/90]_{S2}$	$[\pm 45/0/90_2/0/\mp 45/\mp 45/0/90_2/0/\pm 45]$
FR003I/6I	$[\pm 45/\mp 45/90/0_3]_S$	$[\pm 45/\mp 45/90/0_6/90/\mp 45/\pm 45]$

Each of the different laminate configurations was manufactured in two web heights ($h_{web} = 0.75$ and 1.25 inches) for a total of six frame configurations. These were labeled FR001I, FR002I, ..., FR006I, where "I" denotes the I-frame cross-section (frames were also manufactured with C- and J-channel cross-sections). Three specimens were manufactured for each of the six configurations, denoted by a serial number appended to the frame identification number, *e.g.*, FR002I-1, FR002I-2, and FR002I-3. A subset of the 18 I-frames was tested in the present study; data from additional tests conducted by NASA is also included herein for comparison.

Because of dimensional variations in the specimens, the cross-sectional geometry of each specimen was measured, including skin and flange thicknesses, and web height (see Fig. 5.2). The measurements were made at ten equally spaced locations around the circumference of the specimen and averaged values were computed for use in the analysis. The average thicknesses for the skin, skin/attachment flange, web, and cap flange are listed in Table 5.2, along with the measured web height. Additionally, the outermost radius at the midspan and frame end, R_0 and R_β, respectively (see Fig. 5.4), as well as the frame arc length a were measured. These

values are listed in Table 5.3. The frame arc span angle 2β was computed using the average radius: $2\beta = a/R_{\text{avg}}$, where $R_{\text{avg}} = \frac{1}{2}(R_0 + R_\beta)$. The values for R_{avg} and β also are listed in Table 5.3.

Table 5.2 Average Flange Thickness and Web Height Measurements

Frame ID	t_{skin} (in)	$t_{\text{attachment}}$ (in)	t_{web} (in)	t_{cap} (in)	h_{web} (in)
FR001I-2	0.089	0.117	0.042	0.048	1.240
FR001I-3	0.082	0.112	0.040	0.042	1.258
FR002I-2	0.083	0.162	0.081	0.083	1.258
FR002I-3	0.083	0.161	0.081	0.084	1.251
FR003I-2	0.082	0.161	0.082	0.086	1.256
FR004I-1	0.083	0.124	0.046	0.042	0.752
F00R4I-2	0.084	0.125	0.053	0.046	0.758
FR005I-1†	0.083	0.168	0.08	0.084	0.75
FR006I-1	0.084	0.166	0.081	0.083	0.748

† Frame measurements incomplete, nominal dimensions used for t_{web} and h_{web}.

The frame and skin sections were fabricated using a NARMCO prepreg tape made with Hercules AS4 graphite fibers in a NARMCO 5208 epoxy resin. The nominal thickness of the prepreg tape was 0.05 inches and the average volume fraction was 60 percent. The nominal material properties for AS4/5208 are listed below [Collins and Johnson, 1989].

$$E_1 = 18.4\ (10^6)\ \text{psi}$$

$$E_2 = 1.64\ (10^6)\ \text{psi}$$

$$\nu_{12} = 0.30$$

$$G_{12} = 0.87\ (10^6)\ \text{psi}$$

$$G_{13} = 0.87\ (10^6)\ \text{psi}$$

$$G_{23} = 0.49\ (10^6)\ \text{psi}$$

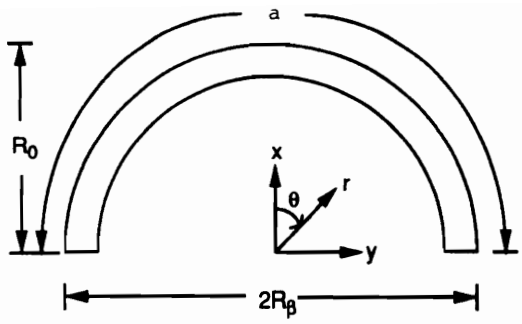

Fig. 5.4 Frame Specimen Geometry

Table 5.3 Frame Radius and Arc Length Measurements

Frame ID	R_{avg} (in)	a (in)	$\beta^{\dagger}$ (deg)	R_0 (in)	R_β (in)
FR001I-2	36.063	110.125	87.48	36.063	36.063
FR001I-3	36.078	110.563	87.79	36.250	35.906
FR002I-2	36.219	110.250	87.20	36.125	36.313
FR002I-3	36.094	110.625	87.80	36.000	36.188
FR003I-2	35.454	111.188	89.84	33.688	37.219
FR004I-1	35.689	112.500	90.30	35.550	35.828
FR004I-2	36.532	112.375	88.12	37.250	35.813
FR005I-1‡	36.	n/a	90.	36.	36.
FR006I-1	36.407	111.625	87.84	36.438	36.375

† Span angle computed by $2\beta = \frac{a}{R_{avg}} \frac{180}{\pi}$.

‡ Frame measurements unavailable, nominal dimensions used for analysis.

where E_1, E_2 are the ply elastic moduli in the longitudinal (fiber) and transverse direction, respectively; ν_{12} is the major Poisson's ratio; G_{12}, G_{13} and G_{23} are the in-plane and transverse shear moduli, respectively.

The material properties satisfy the constraint equations derived from the maximum strain criterion in Section 3.1.1 given by Eqs. 3-16 through 3-19. For the in-plane properties listed above, the compliance matrix can be written as

$$\mathbf{S} = \begin{bmatrix} \frac{1}{E_1} & \frac{-\nu_{21}}{E_2} & 0 \\ \frac{-\nu_{12}}{E_1} & \frac{1}{E_2} & 0 \\ 0 & 0 & \frac{1}{G_{12}} \end{bmatrix} = \begin{bmatrix} 5.43 & -1.63 & 0 \\ -1.63 & 61.0 & 0 \\ 0 & 0 & 115. \end{bmatrix} 10^{-8} \frac{\text{in}^2}{\text{lb}} \qquad (5\text{-}1)$$

Substituting the compliance values S_{ij} and the failure strains in Eqs. 3-16 through 3-19 yields:

$$-\frac{S_{11}}{S_{12}} > \frac{\sigma_2^C}{\sigma_1^T} \quad \Longrightarrow \quad 3.33 > 0.181 \tag{5-2}$$

$$-\frac{S_{11}}{S_{12}} > \frac{\sigma_2^T}{\sigma_1^C} \quad \Longrightarrow \quad 3.33 > 0.0563 \tag{5-3}$$

$$-\frac{S_{22}}{S_{12}} > \frac{\sigma_1^C}{\sigma_2^T} \quad \Longrightarrow \quad 37.7 > 17.7 \tag{5-4}$$

$$-\frac{S_{22}}{S_{12}} > \frac{\sigma_1^T}{\sigma_2^C} \quad \Longrightarrow \quad 37.7 > 5.51 \tag{5-5}$$

The AS4/5208 material strength data was estimated using average strength data measured for AS4/3502 prepreg tape [Sensmeier, Griffin, and Johnson, 1988]:

$$\sigma_1^T = 178.1\ (10^3)\ \text{psi}$$

$$\sigma_1^C = 132.4\ (10^3)\ \text{psi}$$

$$\sigma_2^T = 7.46\ (10^3)\ \text{psi}$$

$$\sigma_2^C = 32.3\ (10^3)\ \text{psi}$$

$$\sigma_6^F = 12.5\ (10^3)\ \text{psi}$$

5.2 Test Setup and Fixtures

The testing machine used was a hydraulic Baldwin machine with a maximum capacity of 120,000 pounds. A typical specimen mounted in the machine prior to testing is shown in Fig. 5.5. A steel I-beam (W6×12) was bolted to the stationary crosshead of the testing machine to support the frame/skin specimen. The I-beam was sized so that the deflection of the beam under load would be less than one percent of the deflection of the specimen. The I-beam was mounted diagonally in the test machine in order for the steel I-beam and attached six-foot wide specimen to clear the load frame of the testing machine (see Fig. 5.5). This orientation also allowed for the maximum contact area between the specimen and table along the table diagonal. The table measured approximately 36× 36 inches, and the table diagonal was 41 inches.

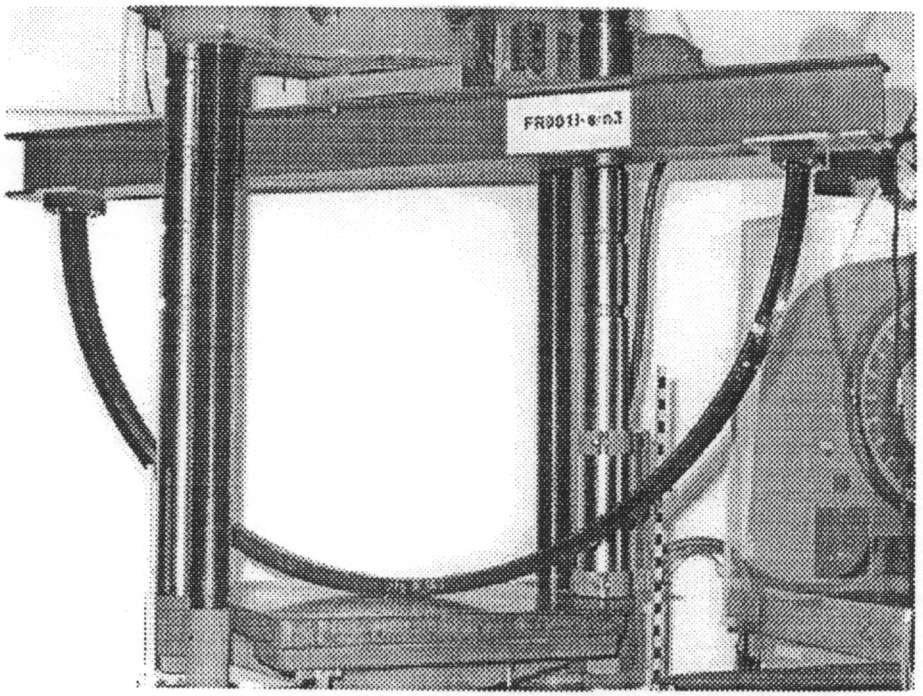

Fig. 5.5 Typical Frame Specimen in Testing Machine

The specimens were potted using Hysol-934 compound in rigid steel housing measuring 5 inches wide by 3.5 inches deep by 1.5 inches thick, shown in Fig. 5.6. The block was machined such that a typical specimen would fit in the block with approximately 0.1 inches of clearance between the block and the specimen. This fixture was designed to maximize the clamping rigidity by minimizing the amount of potting material used. Glass beads were added to the potting compound to increase the rigidity: the potting compound was mixed using 60 percent epoxy, 20 percent catalyst, and 20 percent glass beads. The mixture was poured into the slot and the specimen was immediately inserted into the potting compound and secured until the mixture cured.

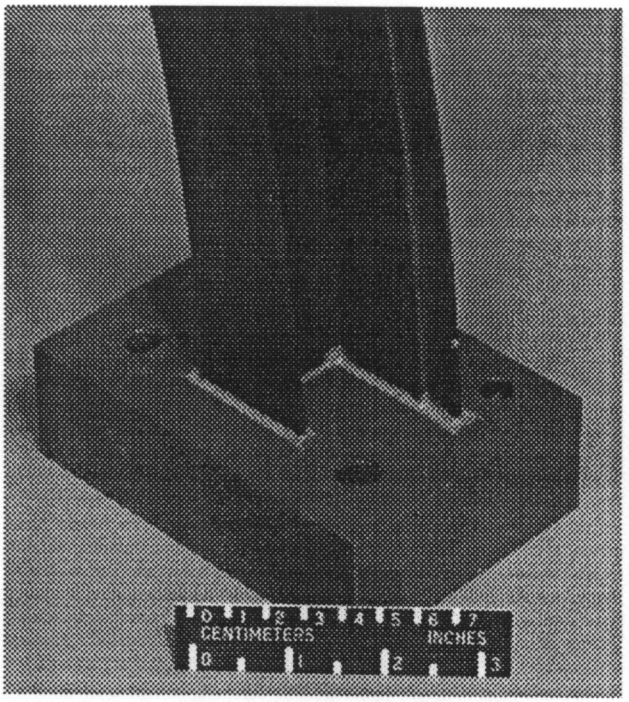

Fig. 5.6 Frame Clamping Fixture—Steel Housing

Earlier frame tests (FR001I-2, FR002I-2, FR004I-1) used a different fixture shown in Fig. 5.7. The frames were potted in a block of epoxy measuring approximately 4 inches wide by 2.5 inches deep by 1.5 inches thick, and held in place by an

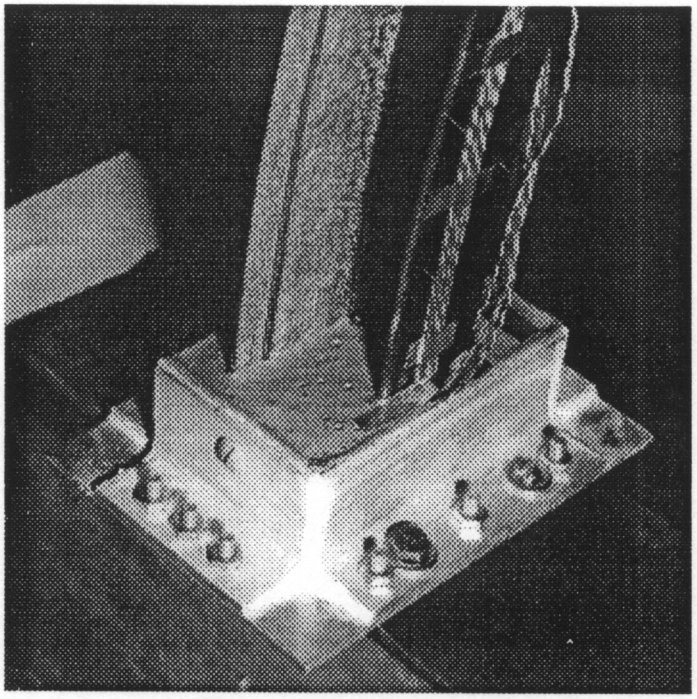

Fig. 5.7 Frame Clamping Fixture—Aluminum Housing

aluminum housing constructed from 1.5 inch angle. These angles were not welded together, but bolts attached to the angles were embedded in the epoxy.

The specimen was loaded in compression by hydraulically raising the lower table. The tests were conducted using displacement-control, and the table speed was adjusted throughout the tests to maintain a loading rate of approximately 1000 pounds per minute. Multiple fractures were allowed to occur in a specimen while the fractured ends of the specimen remained in contact with the table. The stroke of the hydraulic load capsule was limited to approximately six inches which was sufficient to record data for several fractures in each test.

5.3 Instrumentation

Data collected during tests consisted of vertical crushing load, vertical crushing displacement, and strains. The data were recorded on magnetic tape, digitized, and plotted. The measuring sensors and data acquisition system are described in detail next.

5.3.1 Load Measurement

The load cell output was displayed by a dial indicator attached to the testing machine. Also, a slide wire potentiometer and full bridge completion circuit were attached to the bellows of the dial indicator to provide an output voltage proportional to the load. The voltage was amplified and recorded using the data acquisition system described in Section 6.3.4.

5.3.2 Displacement Measurement

A Celesco Displacement Transducer (model number PT 101-0040-111-5110) was used to measure the displacement of the table relative to the test machine base. This measurement is equivalent to the deflection of the specimen relative to the I-beam support. The transducer output voltage was amplified and recorded using the data acquisition system described in Section 6.3.4.

5.3.3 Strain Measurement

Both uniaxial strain gages and rosettes were used to measure the strain distribution along the specimen during the crush test. A typical installation of gages on the web is shown in Fig. 5.8. The translucent plastic tubes taped to the web contain coiled strain gage leads which easily fed out as breakage of the specimen occurred. This mechanism allowed strain data collection over large crushing distances, past multiple failures and throughout the entire test deflection range.

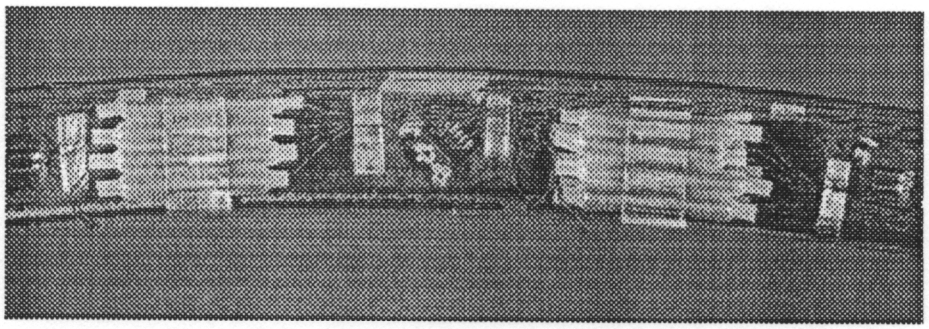

Fig. 5.8 Typical Strain Gage Installation

Standard structural 350 ohm unidirectional strain gages with a 0.187 inch gage length were used for most areas of the frame (Micro-Measurements type CEA-06-187UW-350). Smaller 350 ohm rosettes with a 0.062 inch gage length were used in areas of high strain gradient (Micro-Measurements type CEA-06-062UR-350). All the unidirectional gages were aligned along the circumferential axis. The rosettes were aligned at 0, 45, and 90 degrees from the circumferential axis. The gages were connected to a full-bridge completion circuit and the output voltage was amplified and recorded by the data acquisition system described next. Some of the strain gage data was smoothed to eliminate high frequency noise.

5.3.4 Data Acquisition System

The data acquisition system is an analog system designed for use in short duration crash tests [McCormick, et al., 1982]. The voltage signals were amplified using amplifiers designed and built at NASA Langley Research Center (LaRC), and recorded onto a magnetic tape using a constant bandwidth FM multiplexing technique. The amplified signal was first converted to a discrete FM signal using a Metraplex High Level Voltage Control Oscillator (model number 114). Then the FM signal was recorded by a 28 track Honeywell Magnetic Tape Recorder/Reproducer System (model number 96). The analog data on the tape was de-multiplexed and digitized by the Analysis and Computation Division at LaRC. The digitized data was filtered and plotted by Unisys Corporation under a NASA support contract.

CHAPTER 6
COMPARISON OF ANALYSIS AND EXPERIMENT

The progressive failure methodology described in Chapters 2–4 was used to analytically predict the nonlinear response of the frames described in Chapter 5; the analytical predictions are compared to the experimental results in this chapter. The finite element model is described in Section 6.1, followed by results from a linear analysis of the frames (used to validate the model) in Section 6.2. The nonlinear analysis of the frames without damage is described in Section 6.3, then the damage model is added to the analysis in Section 6.4. Several parameters affecting the nonlinear analysis with damage are investigated in this last section, including:

6.4.1 nonlinear analysis control parameters

6.4.2 material failure data

6.4.3 mesh effects

6.4.4 damage model

All the figures have been placed at the end of the chapter due to the large number and size of the figures.

6.1 Frame Finite Element Model

The frame was analyzed using the shell elements described in Chapter 4. The frame cross-section was treated as a "branched-shell," and each component was discretized in the finite element model, *i.e.*, the skin, skin/attachment flange, web, and cap flange were each discretized. Common nodes along component interfaces served to enforce continuity of displacements and rotations between the components. The eccentricity of the skin/attachment flange was accounted for by using the skin midsurface as the reference surface, *i.e.*, $e = \frac{1}{2}(t_{skin} - t_{attach})$, see Fig. 5.2. The radius along the arc of the frame was varied according to:

$$R(\theta) = R_0\left(1 - \frac{\theta}{\beta}\right) + R_\beta \frac{\theta}{\beta} \tag{6-1}$$

where R_0 and R_β were measured values of the outermost radius at the frame midspan and clamped end, respectively (Table 5.3).

A convergence study was conducted to determine the appropriate mesh for the model using 4-node (bilinear) elements. As a result, the frame was discretized at 181 locations around the circumference of the frame, *i.e.*, each element cut an arc angle of approximately one degree. Eight elements were used to model the skin (with six elements in the skin/attachment flange region), three elements were used in the web and six elements in the cap flange. The resulting model consisted of 3258 nodes, 3060 elements, and 16,652 active (unconstrained) degrees-of-freedom. The finite element discretization of the frame cross-section is shown in Fig. 6.1.

The potted ends of the frame were treated as fixed for the purpose of this analysis. The contact between the frame and table was modeled using specified radial displacements at $\theta = 0°$. The reactions corresponding to these constraints were summed to obtain the load reacted by the frame. Additional constraints on the cross-sectional deformation may have been introduced as the contact area between

the table and frame grew during the experiments. This effect was not modeled in the present study, but could be incorporated using contact elements.

6.2 Linear Response (Prior to Failure)

The experimental results for the reacted load versus frame midspan displacement are plotted in Fig. 6.2 for the various specimens tested in the present study. In some cases the load-deflection curve was recorded during unloading as well, as seen in Fig. 6.2. The frame stiffness—defined as $K = P/u_r$, the reacted load divided by the midspan deflection—was determined from the initial slope of the load-deflection curve and is tabulated in Table 6.1.

The linear stiffness results from the finite element analysis were compared to the experimental results to provide some measure of verification of the finite element model; these results are listed in Table 6.1, along with the percentage of the difference between the analytical and experimental results. The linear response for the finite element model is plotted in Fig. 6.2 with the experimental results as well.

Generally good correlation was observed between the analytical and the experimental results in the linear regime before the initiation of damage—most cases were within ten percent. Two factors affected this comparison: (1) the availability of accurate frame measurements, which was important for obtaining a good model, and (2) the reliability of the experimental data, which was suspect in some cases, as discussed below. When both good measurements and data were available, excellent correlation was observed, *e.g.*, for frames FR001I-3, FR002I-3, FR003I-2, and FR004I-2, where the difference between the analysis and experiments was on the order of three percent or less. It is instructive to look at those cases were poorer correlation was observed.

Table 6.1. Comparison of Analytical and Experimental Frame Stiffness

Frame ID	K_{exp} (lb/in)	K_{fea} (lb/in)	$\Delta^{\dagger}$ (%)
FR001I-2	1440	1590	10
FR001I-3	1500	1450	3.3
FR002I-2	2060	3010	46
FR002I-3	2930	2970	1.4
FR003I-2	3140	3140	0
FR004I-1	482	546	13
FR004I-2	622	635	2.1
FR005I-1	765	974	27
FR006I-1	1270	1400	10

† Difference between linear and experimental stiffness, $\Delta = \frac{|(K_{fea} - K_{exp})|}{K_{exp}} \times 100\%$.

Frame FR001I-2, tested at Virginia Tech, used a different data aquisition system than the frames tested at NASA LaRC. During the test, the load transducer signal exhibited some drift, *i.e.*, it did not return to zero after the specimen was unloaded at the end of the test. Thus this load data was deemed unreliable. Fortunately, the load readings were recorded visually from the dial indicator; deflection data was visually recorded simultaneously, providing some load-deflection data for the test (Fig. 6.2a). However, this data was subject to human error in simultaneously reading two indicators while the test was in progress.

The results for frame FR002I-2 (Fig. 6.2b) showed the most difference between the analysis and experiment. The difference in the experimental stiffness between frames FR002I-2 and FR002I-3—which nominally have the same geometry—suggests that an instrumentation error may have occurred during the test of FR002I-2. The experimental procedures were reviewed in order to resolve this discrepancy, including checking the calibrations of the displacement transducer and load cell with NASA personnel, and the data reduction techniques with Unisys personnel. Despite

these efforts, this discrepancy was not resolved. Another possibility, which was not investigated at the time, was the presence of some significant manufacturing defect.

The difference observed between the analytical predictions for frames FR004I-1 and FR004I-2 (see Table 6.1) shows the sensitivity of the analysis to the frame measurements. While these two frames have the same nominal configuration, the (linear) stiffness calculations based upon actual measurements are 16 percent different. Obtaining careful measurements of the frame specimens was essential to getting good correlation with the experiments, as seen with frame FR004I-2 where the analytical and experimental stiffness were within two percent. Worse correlation was observed for frame FR004I-1 which was tested by NASA using a different data acquisition system than described in Chapter 5. The load and deflection data were sampled at a lower resolution, resulting in noisy signals (Fig. 6.2d). This was especially evident at lower loads in the linear range, making it difficult to estimate the experimental stiffness.

Frame FR005I-1 (Fig. 6.2e) was also tested by NASA, and the measurements of the specimen were incomplete. Nominal frame dimensions were used in the analysis, resulting in extremely poor correlation with the experiment, and demonstrating again the importance of using accurate specimen dimesions in the model.

6.3 Nonlinear Response (without Damage)

The nonlinear response of the frames (without damage) was predicted using the Newton-Raphson method as described in Section 4.5. The reacted load versus table displacement is shown in Fig. 6.3 for the various frames tested (FR002I-2 and FR005I-1 are not shown due to problems noted in the previous section). Generally

good agreement was observed with the experimental results before frame failure occurred.

The measured and computed strains are compared in Figs. 6.4–7 for the specimens tested at NASA LaRC. Three curves are presented for each frame, representing the circumferential strain distribution on different parts of the frame: the convex surface of the skin at the center of the skin-attachment flange region; the center of the web; and the center of the concave surface of the cap flange. The strain distributions correspond to the table deflection just prior to the initiation of damage, as predicted by the analysis; the corresponding point in the load-deflection point is shown in each strain plot.

The analytical strain distribution was computed at the optimal stress points of the element, which are unique points within an element where the stresses have the same accuracy as the displacements [Barlow, 1976 and 1989]. For the 4-node quadrilateral elements used in the present study, the optimal stress point is the center of the element.

Excellent agreement was observed between the experimental results and the finite element analysis. The finite element results correctly predicted the shape of the strain distribution and good correlation was obtained with the strain gage data at the maximum near 50 degrees.

Poorer correlation was obtained near the midspan, which may be explained by one of several possible reasons. First, the strain gage placement is critical in this localized area of high strain gradients; just a minor misalignment of the gage could result in significantly different strain readings. Another possibility is that the material exhibits nonlinear stress/strain behavior in this region of high strains. Incorporating a nonlinear material model may lead to improved results, *e.g.*, see the work by Hahn and Tsai [1973] which includes a nonlinear shear stress/strain relationship. Finally, differences at the midspan may be due to modeling the frame/table contact

as only a line load instead of a distributed load over the contact surface. Improved results may be obtained by introducing contact elements to model the frame/table contact region.

The analysis of the two frame configurations with thin laminates (the FR001I and FR004I series) exhibited difficulties converging near the failure point, *e.g.*, see Fig. 6.8. The convergence problems were accompanied by the presence of multiple negative roots in the tangent matrix, indicating the presence of a bifurcation point and that the analysis was on an unstable equilibrium path. Generally, structural imperfections are used to "guide" the nonlinear response onto a stable equilibrium path away from the bifurcation.

Imperfections in the form of the buckling mode shapes were added to the frame models. A Lanczos algorithm was used to calculate the eigenvalue and eigenvector pairs (see Processor LAN, *Computational Structural Mechanics Testbed User's Manual* [1989]). The first several modes are tabulated in Table 6.2 along with the experimental failure load.

Table 6.2. Comparison of Analytical and Experimental Critical Loads

Frame ID	λ_1 (in)	λ_2 (in)	λ_3 (in)	Experiment (in)
FR001I-2	0.654	0.775	0.836	0.842
FR001I-3	0.623	0.634	0.684	0.856
FR004I-1	1.15	1.25	1.35	1.50
FR004I-2	1.33	1.43	1.50	1.79

The first two mode shapes for FR00I-3 are shown in Fig 6.9 and 6.10. The first mode is a global bending/twisting mode; the second mode is a local crippling mode involving the web and cap flange (the third mode, not pictured, is another crippling mode similar to mode two). The local buckling occurs in the region of the flange where the strains reach a maximum compressive value of approximately 2000 μin

(see Fig. 6.10). Note that the strain in the skin reached similar levels, however the skin/attachment flange construction is three times as thick as the cap flange (24 plies vs. 8 plies), providing significantly more resistance to local buckling.

The bifurcation appears to be related to the crippling modes. The response of frame FR001I-3 with a single imperfection mode (the bending/twisting mode) is shown in Fig. 6.11; two amplitudes were tried equal to 0.1% and 1.0% of the nominal radius, R=36 inches. The analysis still was unable to converge and the number of negative roots was not reduced. However the addition of the second (crippling) mode did result in a stable equlibrium path with no negative roots, shown in Fig. 6.12. In spite of correcting the instability, the nonlinear analysis continued to experience numerical difficulties, requiring very small load steps to traverse this point. Similar results were obtained with FR001I-2, FR004I-1, and FR004I-2.

The local crippling mode did not appear in the other frames, which used thicker cap flanges (16 plies vs. 8 plies in the FR001I and FR004I series). No negative roots were observed in the analysis of these other frames, thus no additional imperfections were necessary to produce a stable equilibrium path. As an aside, the first mode for these frames was similar to the bending/twisting mode shown in Fig. 6.9.

6.4 Nonlinear Response Including Damage

Next we consider the effect of damage in the nonlinear response using the damage models described in Chapter 3. Phenomenological failure criteria are used to predict the initiation of damage in the material; subsequently damage constitutive models are used to redistribute the stresses in the damaged material. This section

compares the results from different failure criteria and damage models, as well as considering some further aspects of the nonlinear solution procedure.

We begin by comparing typical analytical results (including damage) from several frames to the experimental data in Fig. 6.13. These analyses use the maximum strain failure criterion and the ply discount damage model. The analysis captured several key components of the response curve, including the failure load, the magnitude of the unloading and the residual stiffness of the frames after failure. The analysis was able to consistently predict these response characteristics for many of the frame configurations.

The development of the failure patterns predicted by the progressive failure analysis was similar for the different frames. A typical case is illustrated in Fig. 6.14 for frame FR004I-1 and described below.

Typical Failure Pattern Predicted by Progressive Failure Analysis

Step 8 The damage was initiated by matrix cracking in the 90° plies of the web and cap flange (audible "popping" sounds occurred in the experiment around this point). The matrix cracking initiated at the center of the web and spread circumferentially outward over the next several steps.

Step 12 The matrix cracking spread to the off-axis 45° plies in the cap flange near the midspan; matrix cracking also initiated in the 90° plies of the cap flange near the base of the frames.

Step 14 Shear failure was indicated in the 90° and 45° plies of the cap flange near the midspan; note that the shear stiffness is already discounted by the matrix failure model (see Eq. 3-38).

Step 15 Matrix cracking in the off-axis plies was initiated in the web. Also, matrix and shear failures were indicated in the load-bearing 0° plies of the cap flange at the point where local crippling occurs (see Fig. 6.10).

Step 16 Frame failure occurred due to fiber failures in the load-bearing plies in the web and cap flange. Matrix cracking started in the attachment flange, which was undamaged up to this point.

The analytical prediction of the load drop after the frame failure was generally less than observed in the experiments. High speed video of the frame tests showed that the frame response after the load-bearing plies failed was dynamic, *i.e.* the frame exhibited vibratory motion in the plane of the frame. This may have led to the development of additional damage (and subsequent load drop) as the motion was damped out; the static nonlinear solution procedure used for the analysis would not capture this dynamic effect.

Another possible explanation for the reduced load drop is that delaminations were observed in the experiments that were not included in the analysis. Usually these delaminations occured where cap plies where co-cured with the frame cross-section (see Fig. 5.3); a typical failed, delaminated specimen is shown in Fig. 6.15. These delaminations may have increased the load drop at frame failure; the analysis assumed that the damaged plies remained perfectly bonded.

A final, general observation can be made about the damage analysis: the analytical results both with and without damage yielded almost identical results up to the point where the load-bearing plies start to fail, as illustrated in Fig. 6.16. This is not surprising since the loss of stiffness in the off-axis plies due to matrix cracking is relatively small compared to the overall frame stiffness. This result has some significance in the choice of the damage model, as will be discussed in Section 6.4.3.

6.4.1 Nonlinear Analysis Control Parameters

Several parameters available to control the step size in the nonlinear solution procedure were described in Section 4.5.2. The objective of these controls is to provide an adequate description (or resolution) of the equilibrium path, especially in the vicinity of the frame failure, while minimizing the number of steps required to trace the path. The parameters include (1) desired number of iterations

(DES_ITERS); (2) maximum number of iterations (MAX_ITERS); (3) maximum number of divergences (MAX_DIV); and (4) maximum number of step cuts (MAX_CUT). Recall the DES_ITERS parameter was used to automatically scale the step size and the MAX_ITERS and MAX_DIV parameters triggered step cuts that automatically halved the step size. These parameters had to be used carefully to avoid unpredictable results, as described below. While these controls were meant to optimize the nonlinear solution procedure, it was often necessary to disable them to avoid problems.

DES_ITERS. The DES_ITERS parameter used to scale the step size was generally effective except at the point where the load-bearing plies fail; this point can take many iterations to converge compared to points in the response with no damage or just matrix cracking. For example in Fig. 6.14, an average of three iterations was required for steps 1–7 (no damage); six iterations for steps 8–15 (matrix cracking); and 40 iterations for step 16 (load-bearing plies fail). Picking a low value for DES_ITERS (*e.g.* DES_ITERS=3) suitable for the undamaged portion of the response curve would lead to increasingly smaller steps as damage started to accumulate. Coupled with the step cuts described next, it was possible for the analysis to bog down since the step size would become too small, requiring a restart of the analysis. Nevertheless, this provided the best prediction of the actual failure load, since that is where the analysis would stop; Fig. 6.17 shows the response of Frame FR002I-3 using DES_ITERS=3. Note how the step size becomes very small near the failure load.

If DES_ITERS was set to a larger value suitable for the damaged region (*e.g.* DES_ITERS=8), then the step size would increase quickly earlier in the analysis, where the analysis converged in fewer than DES_ITERS iterations. The larger step size would make it difficult to capture any details of the load-deflection path around the failure point, as shown in Fig. 6.17 for DES_ITERS=8.

Disabling the automatic step scaling feature allowed the analysis to run through the frame failure in many cases without a restart. However this presents a similar problem to using a large value for DES_ITERS: potentially poor resolution of the load-deflection response around the failure point. This is illustrated in Fig. 6.18, which compares an analysis with a constant load step to the analysis with DES_ITERS=3. While the load-deflection curve is reproduced accurately, the peak load at the failure point is missed by the constant load step analysis. Of course this may be improved by decreasing the step size, with the tradeoff being increased analysis cost.

Finally, note that in all the cases shown in Figs. 6.17 and 6.18, the load-deflection curve was reproducible. Only the resolution of the curve in certain areas of interest—such as the failure point—changed for different parameter settings.

MAX_ITERS. This parameter sets the maximum number of iterations allowed in a step; if exceeded the step size is automatically halved (a maximum number of step cuts is allowed as discussed below). In the absence of damage a small number of iterations usually was sufficient to achieve convergence (*e.g.* MAX_ITERS<10). However when damage occurred, especially in the load-bearing plies, a greater number of iterations was required. Many cases required up to 50 iterations to converge, the maximum allowed in the present study.

Interestingly, a large number of iterations might be required even with a small load step when damage was accumulating. As damage is detected in the element the stresses are relieved and redistributed locally. This may cause new failures to develop, and the process repeats until equilibrium is achieved. In the case of the load-bearing plies failing, more load is shed than during matrix cracking, and a greater number of iterations is required to reach equilibrium. Thus even if a small step is taken that initiates failure of the load-bearing plies, it will take many iterations to converge. As may be expected, the 0°-dominated layup in the FR003I

series required a greater number of iterations to converge than the quasi-isotropic layups used in the FR001I and FR002I series.

MAX_DIV. This control was designed to limit the number of times the convergence criterion was allowed to increase within a step to prevent the solution from diverging. However the convergence criterion tended to fluctuate (*i.e.*, occasionally rise) due to stress redistribution when damage was developing, especially during failure of the load-bearing plies. Figure 6.19 illustrates a typical case where the error appears to be converging but then rises after a couple of iterations, repeating this pattern until finally converging. In this case, the MAX_DIV parameter would have cut the step size unnecessarily, since the solution converges despite the fluctuations in the convergence criterion.

Cutting the load step did not guarantee eliminating the fluctuations of the convergence criterion. Recall that even for a small step, failure of the load-bearing plies could require a large number of iterations to converge. The fluctuations in the convergence criterion would still appear as the load step size was decreased, leading to more cuts due to MAX_DIV and increasingly smaller steps.

This parameter was generally not helpful and was disabled for most cases.

MAX_CUT. This paramater limited the number of step cuts due to MAX_ITERS or MAX_DIV being exceeded. A value of MAX_CUT=3 was found to be adequate for most cases.

6.4.2 Effect of Material Failure Data

One of the more significant factors affecting the damage response was the lack of available failure data for the AS4/5208 material system used to construct the frames. Data is not available for AS4/5208 in standard data sources (*e.g.*, MIL-HDBK-17-2C [1994]). Failure data used in the present study was from tests of a similar material system, AS4/3502 [Sensmeier, et al., 1988], which used the same carbon fiber but a different epoxy resin system. The current manufacturer of the 5208 prepreg system is CYTEK Engineered Materials, who provided data for a T300/5208 unidirectional carbon/epoxy prepreg system [Stuart, 1996]. The failure data is listed in Table 6.3; the AS4/3502 data for σ_2^C was substituted for the missing T300/5208 value in the actual analysis.

Table 6.3. Material Failure Data Representative of AS4/5208

Failure Load	AS4/3502 [Sensmeier, et al., 1988] (KSI)	T300/5208 [Stuart, 1996] (KSI)
σ_1^T	178.1	221
σ_1^C	132.4	215
σ_2^T	7.46	7.6
σ_2^C	32.3	n/a
σ_6^F	12.5	16.7

The damage analysis results are compared in Fig. 6.20 with these two sets of failure data. The results obtained with Sensmeier's AS4/3502 data yielded significantly better correlation with the experiments than the CYTEK T300/5208 data, probably since the AS4/3502 material used the same fiber as in the frame specimen. The T300 fibers are stronger than the AS4 fibers, as evidenced by T300/5208 having a tensile yield strength σ_1^T 24 percent higher than AS4/3502. Since the frame failure is due to fiber failures in the web and cap flange, the failure predicted using the T300/5208 material is much higher than with AS4/3502 .

6.4.3 Mesh Sensitivity

The damage models are evaluated within each element so some sensitivity to the finite element discretization is expected. However, unlike traditional ply discount models where properties are degraded in an entire ply, the damage models are evaluated at several material points within each ply (in the through-thickness integration) at each integration point (in the 2-D element integration). This allows damage to be localized at an element integration point, and mitigates the mesh sensitivity.

Comparisons are made in Fig. 6.21 between three frame models: the nominal mesh used in the present study, a refined mesh, and a coarse mesh. The refined mesh used a finer dicretization of the frame cross-section with the same circumferential discretization; the refined model had 20,030 unconstrained degrees-of-freedom (DOF), 22 percent more than the 16,450 DOF in the nominal model. Both the refined nominal models predicted similar failure loads and unloading after failure. However the refined model showed some improvement in predicting the residual frame stiffness, as compared to the experimental response.

The coarse model used a coarser discretization of the frame cross-section and also a coarser discretization in the circumferential direction; the resulting model had only 7959 unconstrained DOF, less than half of the nominal model. The coarse model predicted the same failure load, however the mesh sensitivity becomes evident in the post-failure response. Since the predicted damage affects a greater portion of the finite element model due to the large element size, the level of unloading is higher. Also the residual stiffness prediction is poor compared to the experimental data.

6.4.4 Comparison of Damage Models

The damage model consists of two parts: a failure criterion that predicts the initiation of damage in the material, and a constitutive model that provides a mechanism for stress redistribution in the composite material after damage is initiated. Two failure criteria were tested in the progressive failure analysis, the Maximum Strain criterion and the Tsai-Wu criterion. Results for the two criteria are compared in Fig. 6.22 for two different frames. The Tsai-Wu criterion is a combined stress criterion and yielded a lower, more accurate failure load for the quasi-isotropic frame FR002I-3. In this case failure is predicted due to contributions from high transverse and shear stresses in the 0° plies, and the failure mode is identified as a fiber failure mode ($\max\{f_f, f_m, f_s\}$, see Section 3.1.2). The result is that fiber failure is predicted earlier in the load-bearing plies compared to the Maximum Strain criterion, which requires that $\sigma_1 > \sigma_1^T$. In the fiber-dominated frame, FR003I-2, little difference was observed between the failure load predictions from the Tsai-Wu and Maximum Strain criteria, however the Tsai-Wu criterion yielded better prediction of the magnitude of the unloading and residual frame stiffness.

Two damage constitutive models were compared for the progressive failure analysis (see Section 3.2): a discount method in which the material properties are set to zero, and a statistical model where the properties are reduced more gradually. Figure 6.23 compares results from the progressive failure analysis for Frame FR003I-2 (with the maximum strain crierion) using the discount method and the statistical model with different values of the Weibull strength distribution factor, β. Similar results were obtained between the damage models for $\beta > 2$, and both models showed good correlation with the experiment. The statistical model with $\beta = 2$ showed poorer correlation with the experiment, since the properties degrade faster at low stress for lower values of β, as illustrated in Fig. 6.24.

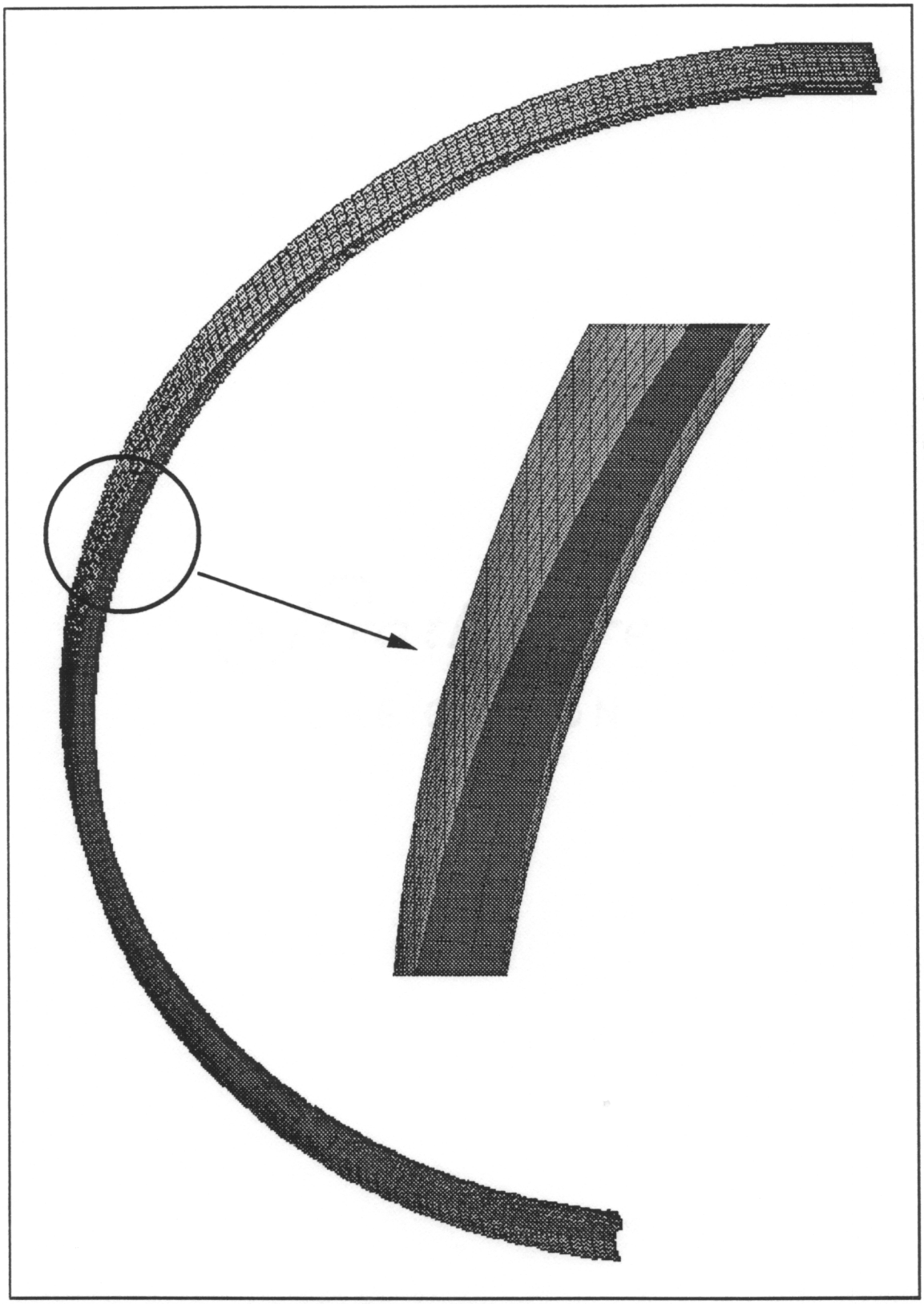

Fig. 6.1 Finite Element Discretization of Frame Specimen

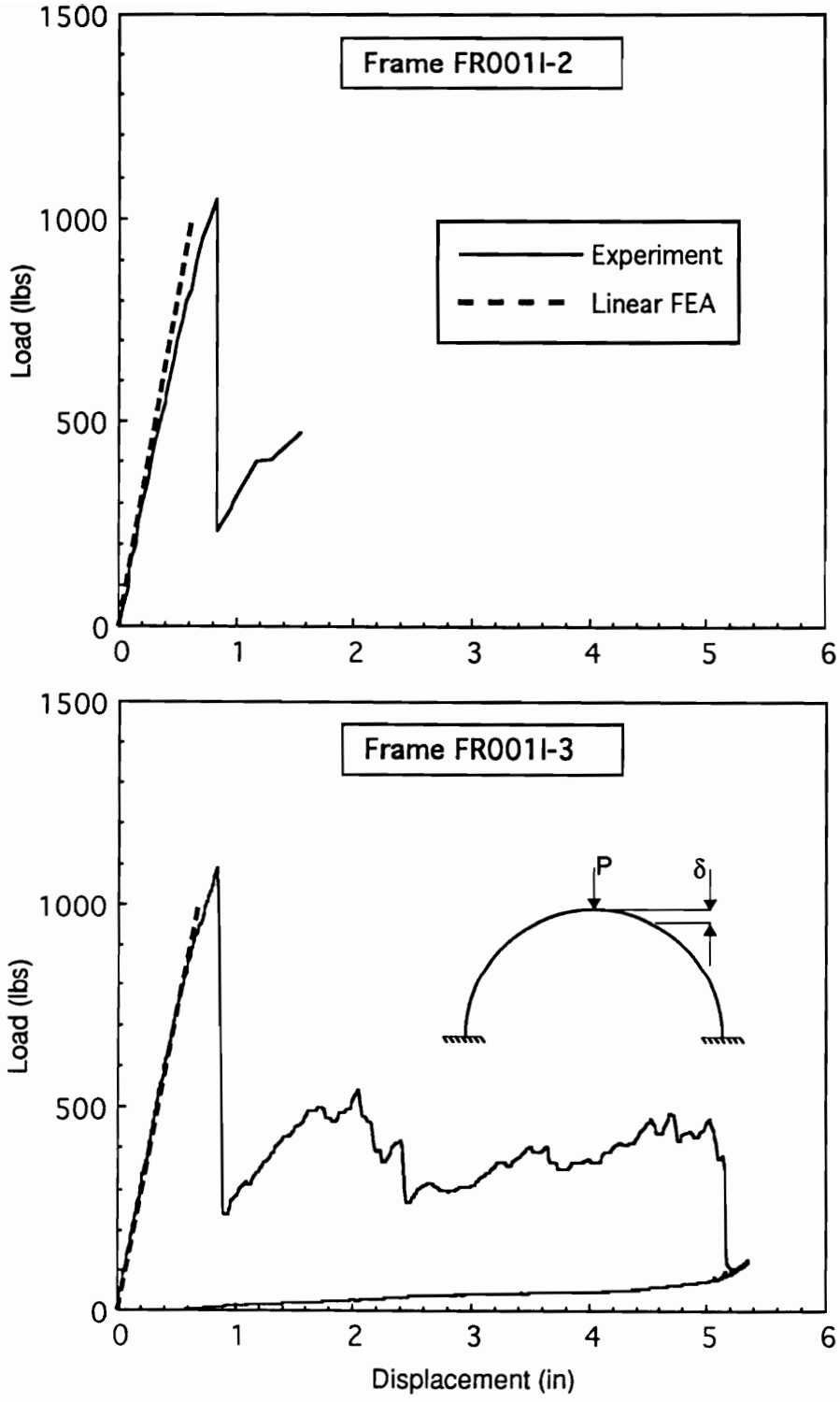

Figure 6.2a Load-Deflection Curves—FR001I-2 and FR001I-3

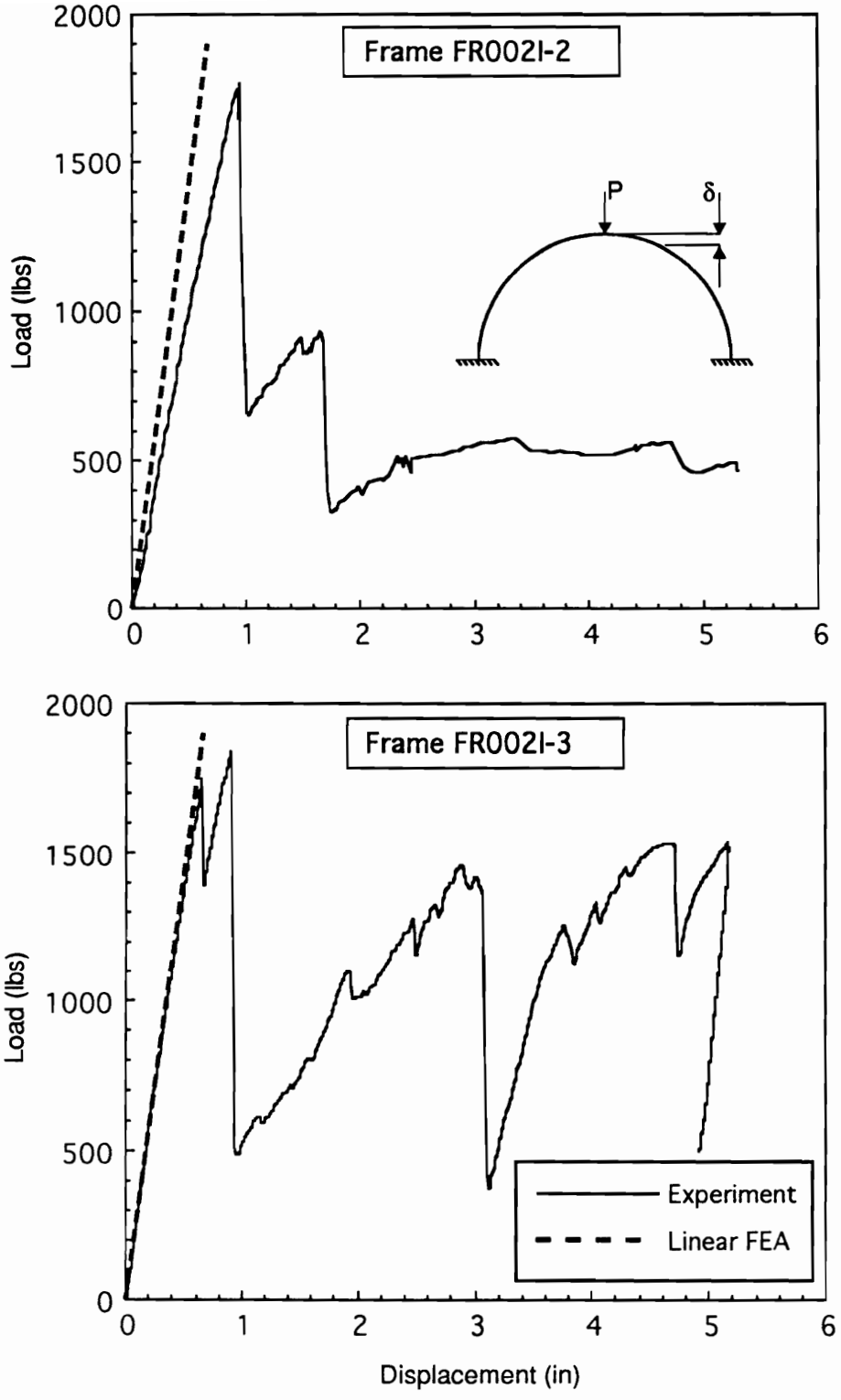

Figure 6.2b Load-Deflection Curves—FR002I-2 and FR002I-3

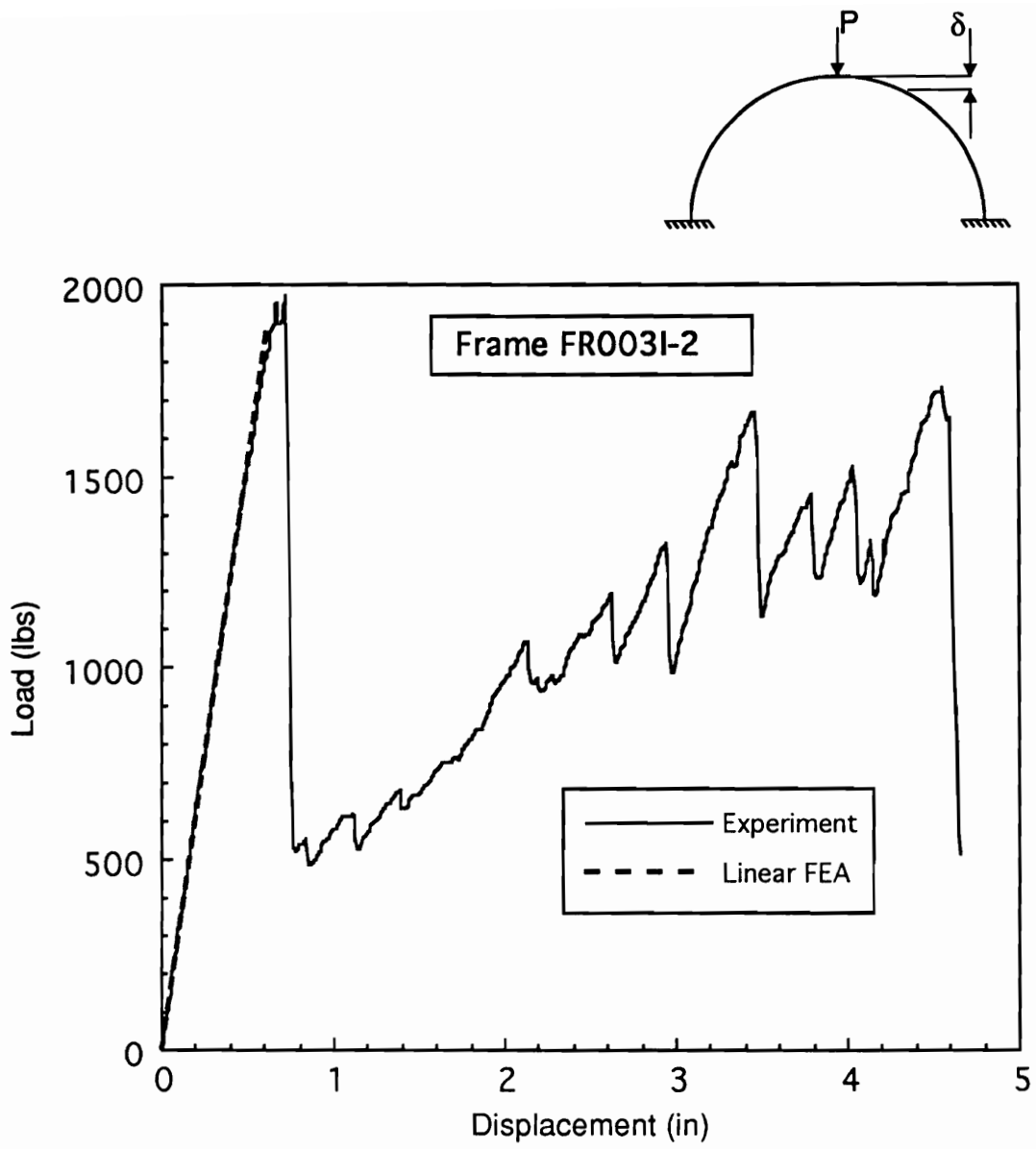

Figure 6.2c Load-Deflection Curve—FR003I-2

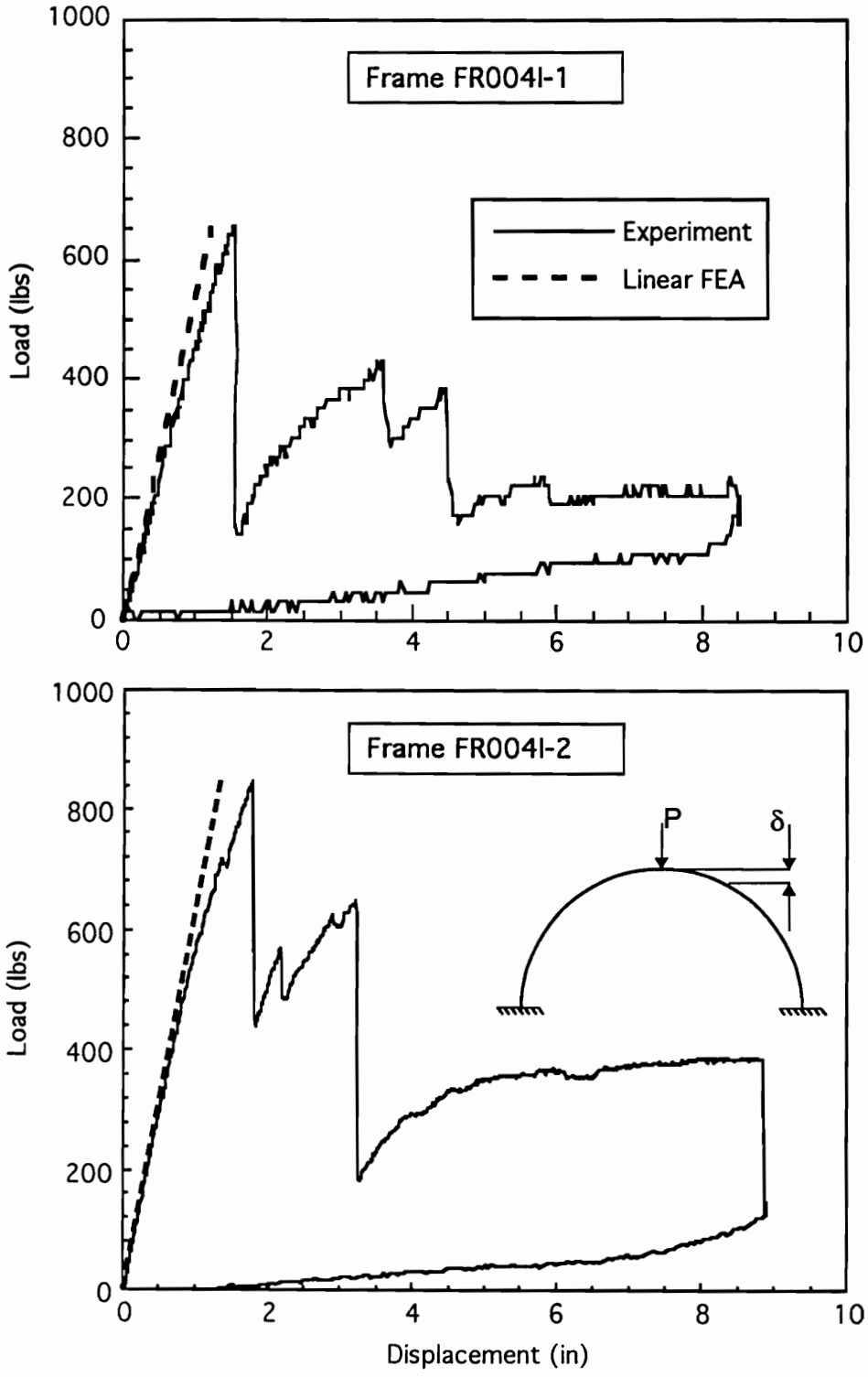

Figure 6.2d Load-Deflection Curves—FR004I-1 and FR004I-2

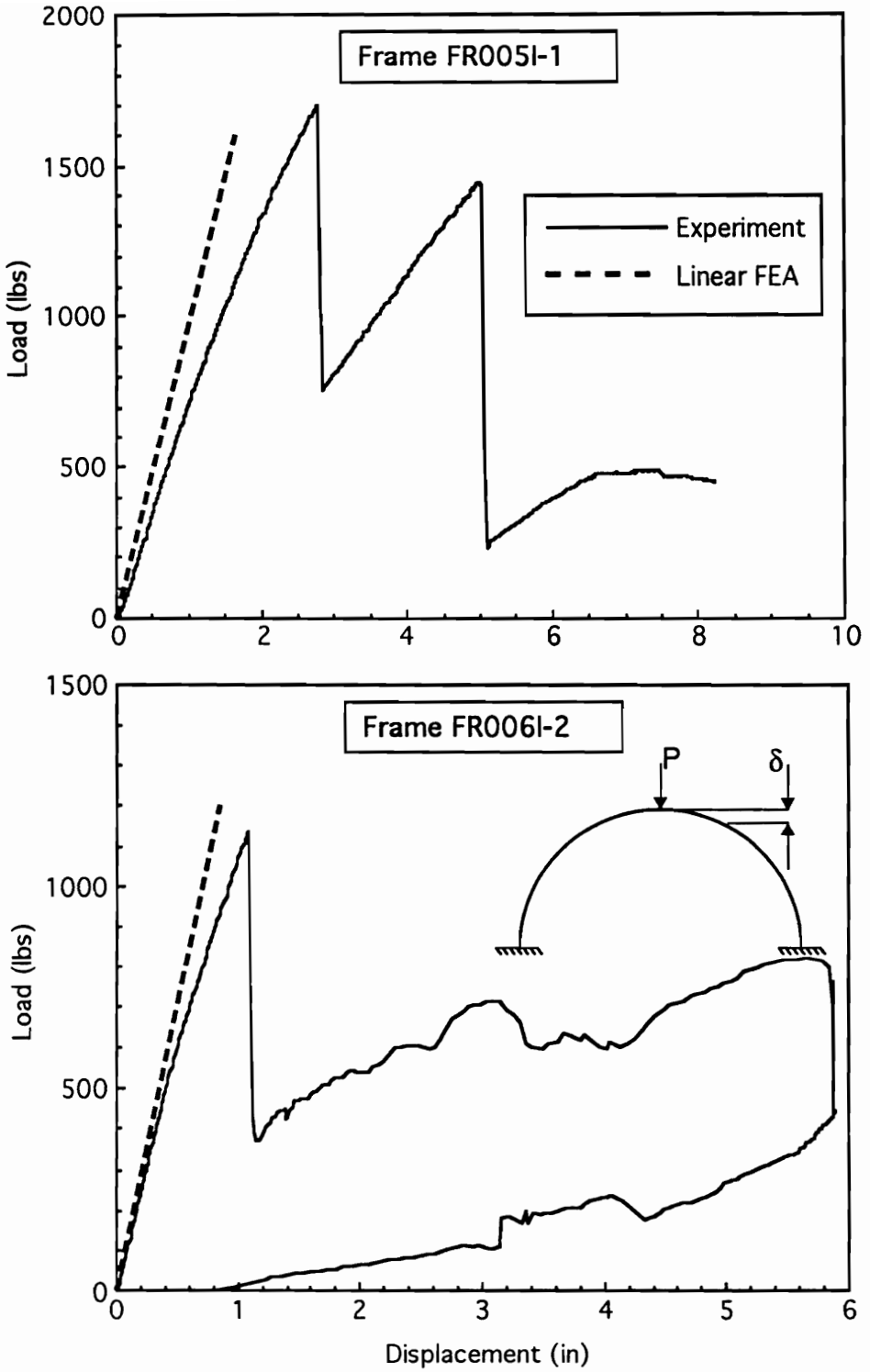

Figure 6.2e Load-Deflection Curves—FR005I-1 and FR006I-2

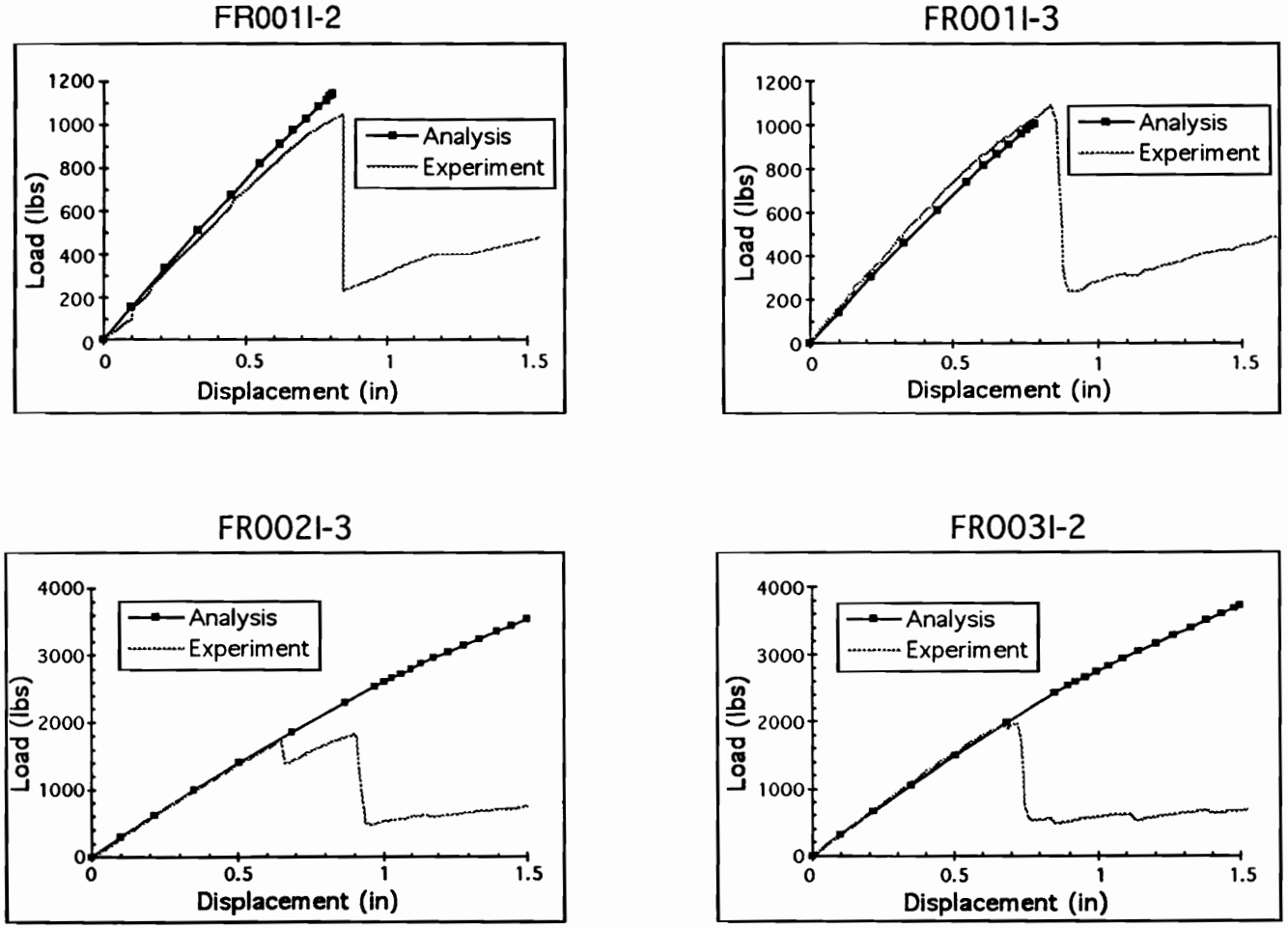

Fig. 6.3 Nonlinear Response Predicted by Analysis (without Damage) Matches Experiments Prior to Failure

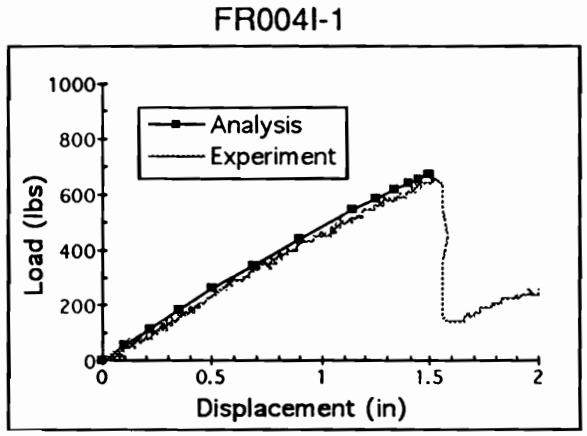

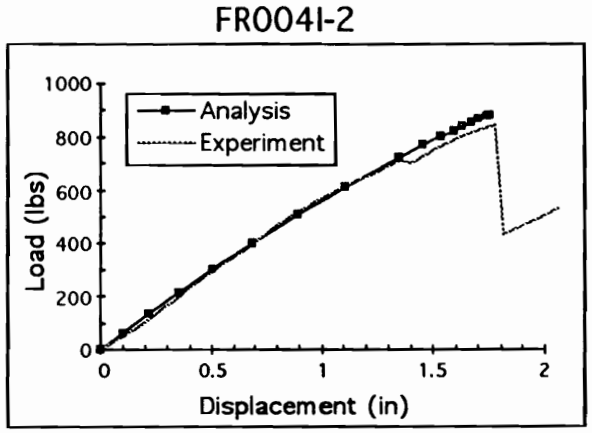

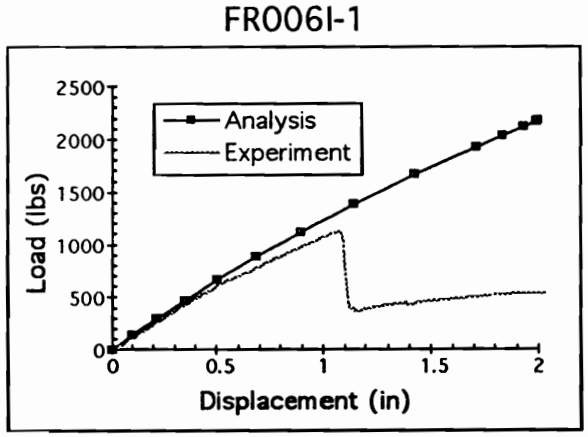

Fig. 6.3 (cont.) Nonlinear Response Predicted by Analysis (without Damage) Matches Experiments Prior to Failure

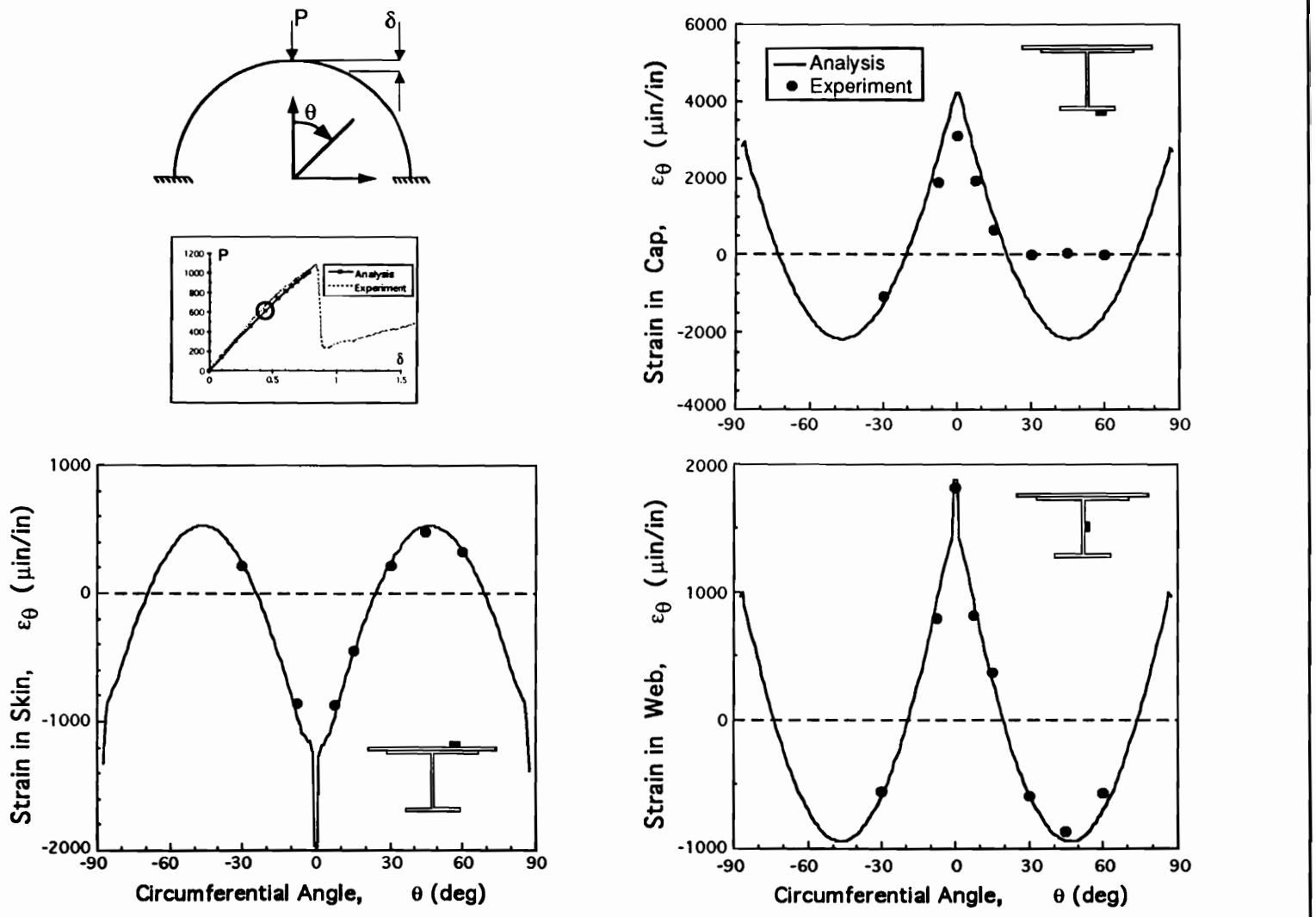

Fig. 6.4 Comparison of Analytical and Experimental Circumferential Strain Distribution—FR001I-3

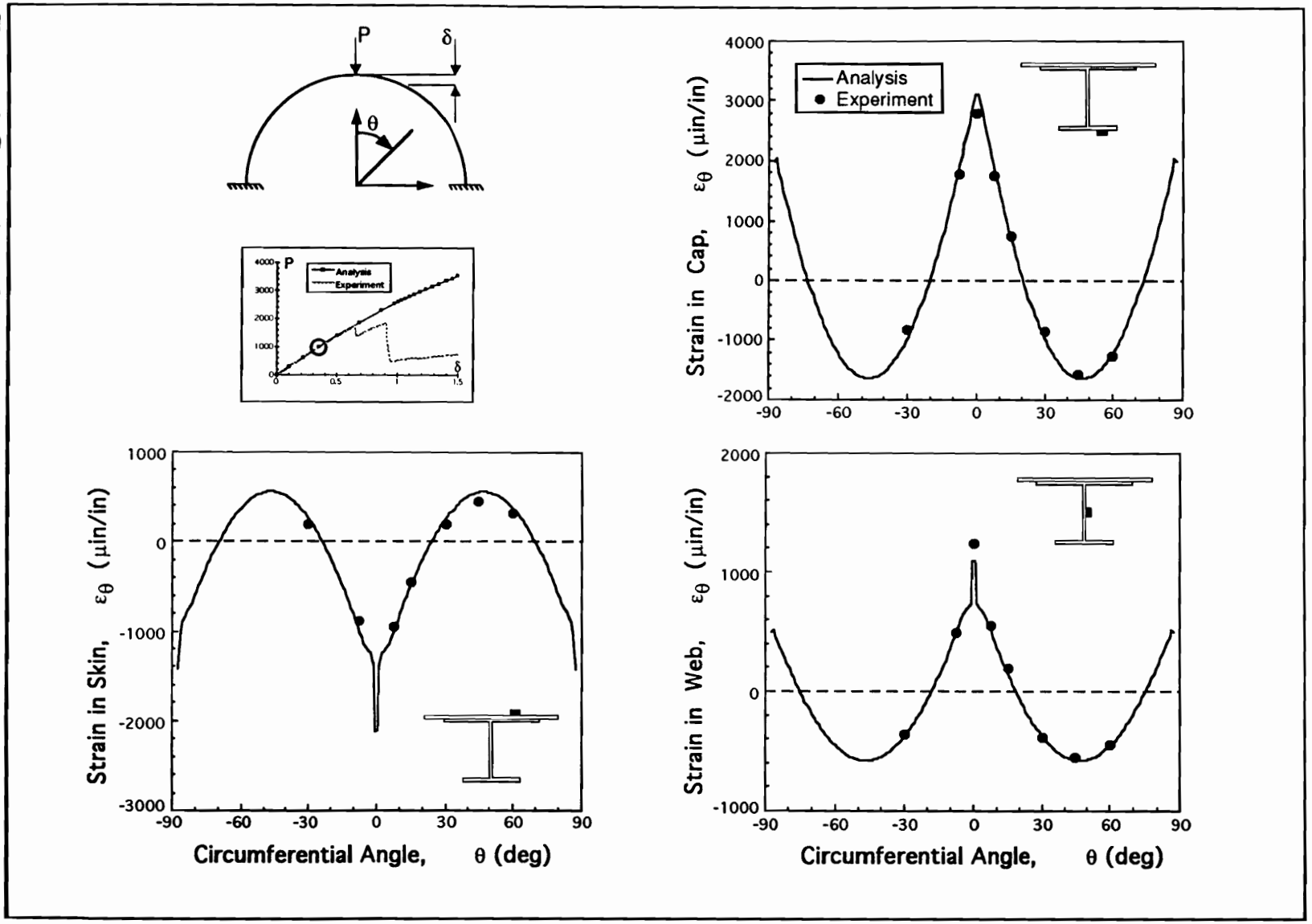

Fig. 6.5 Comparison of Analytical and Experimental Circumferential Strain Distribution—FR002I-3

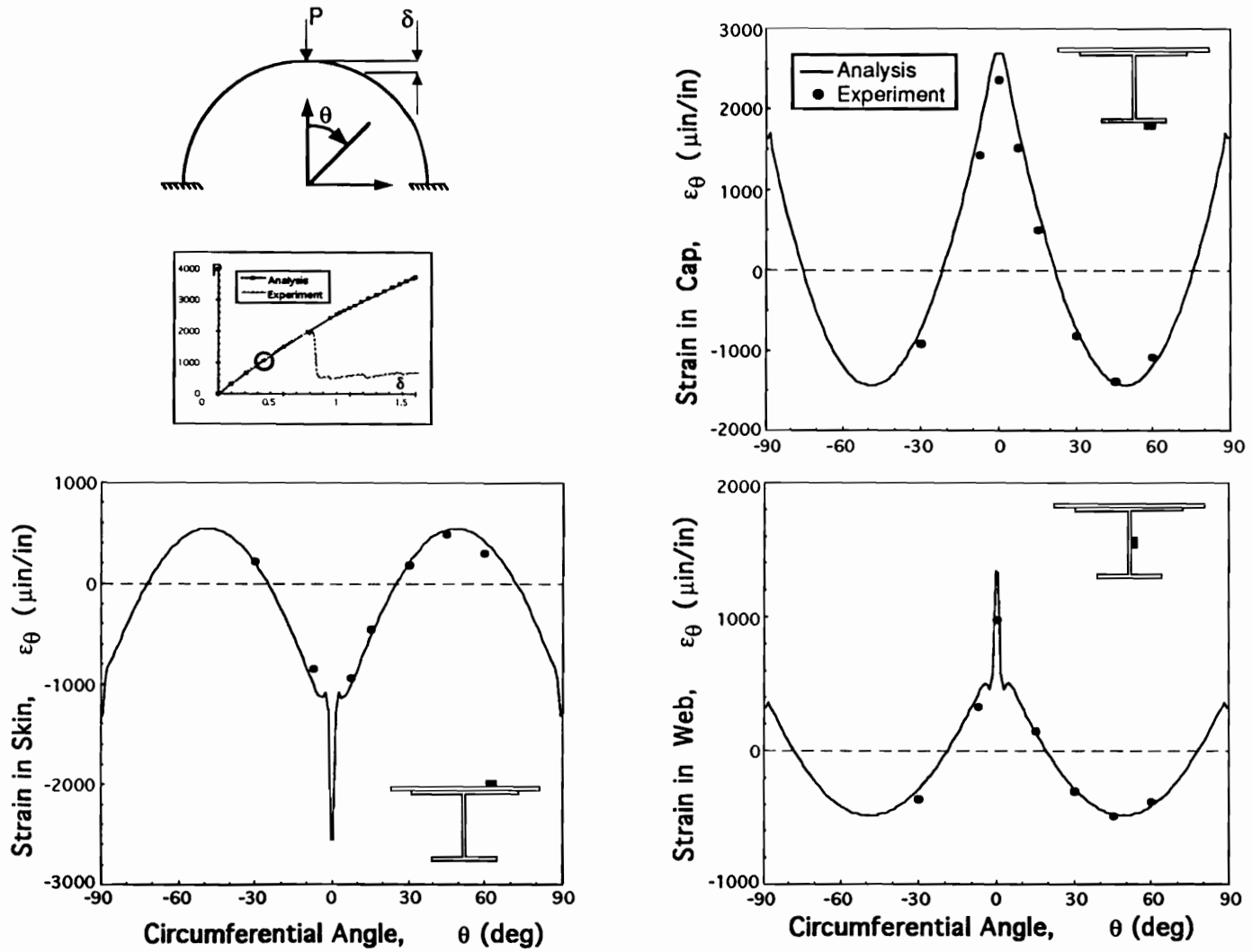

Fig. 6.6 Comparison of Analytical and Experimental Circumferential Strain Distribution—FR003I-2

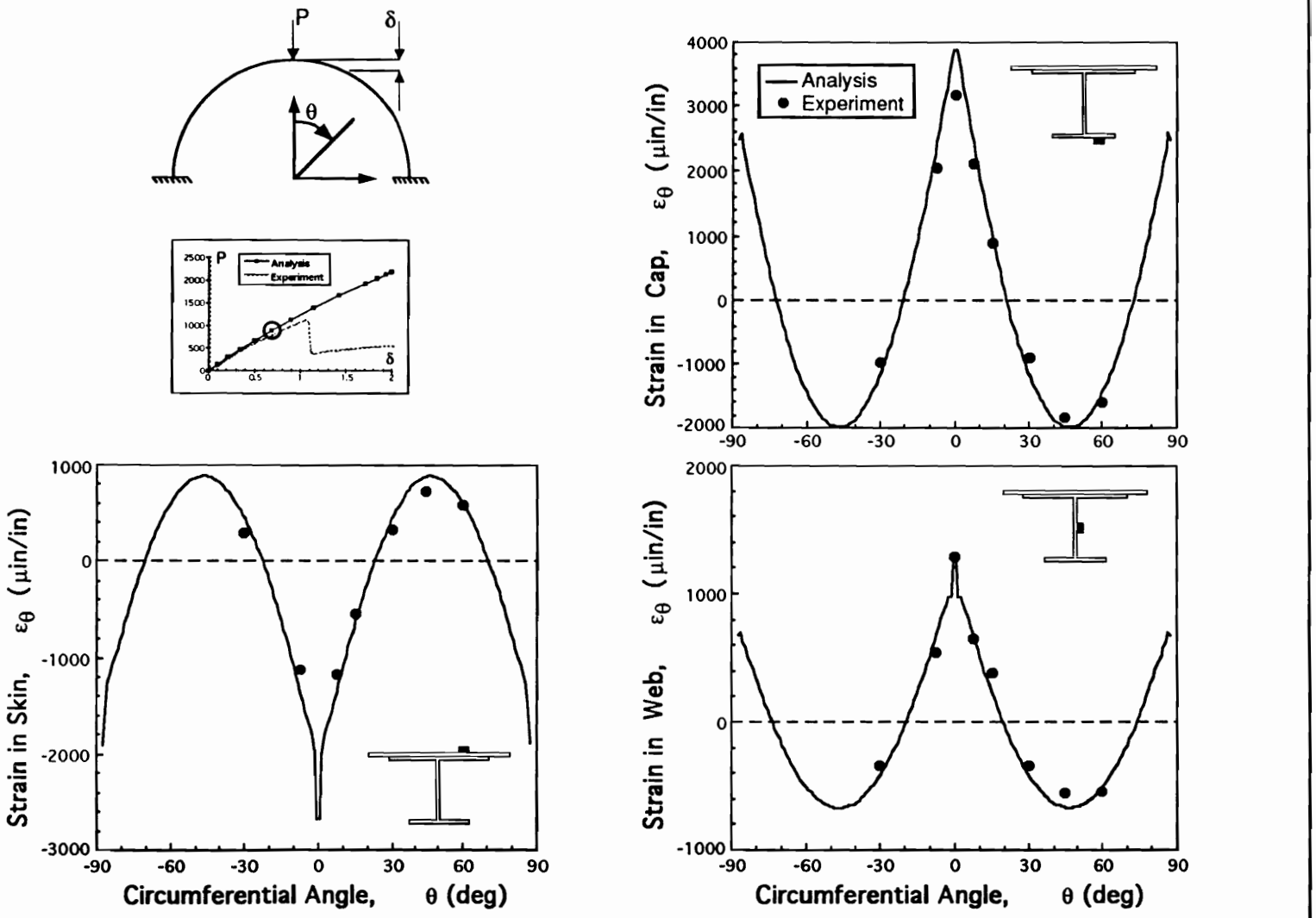

Fig. 6.7 Comparison of Analytical and Experimental Circumferential Strain Distribution—FR006I-1

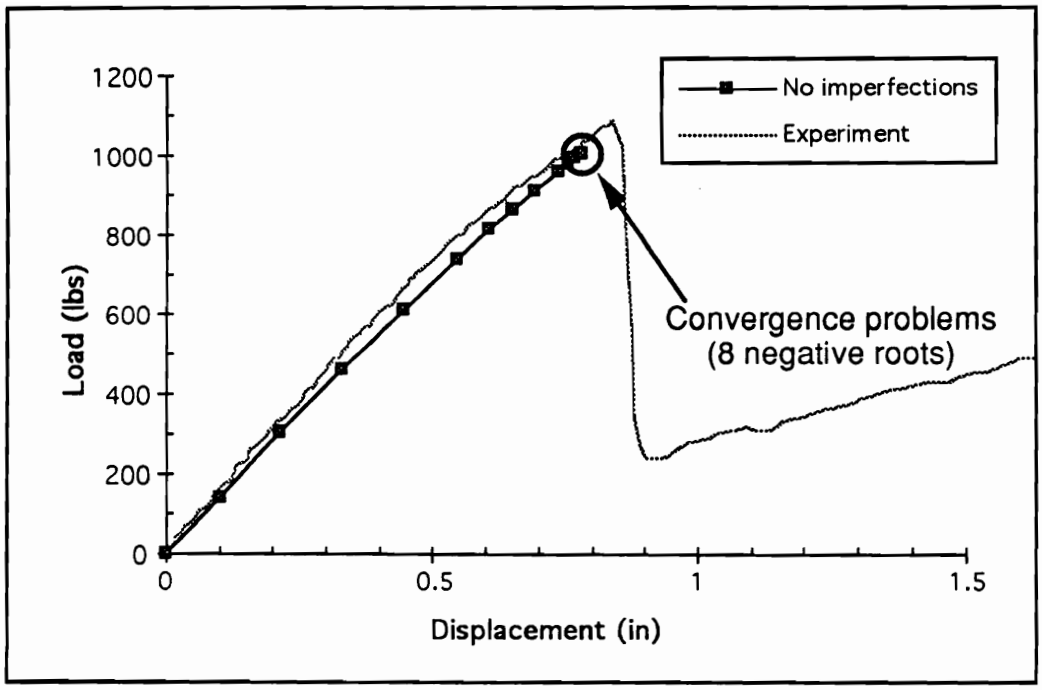

Fig. 6.8 Nonlinear Response of FR001I-3 Exhibits Convergence Problems

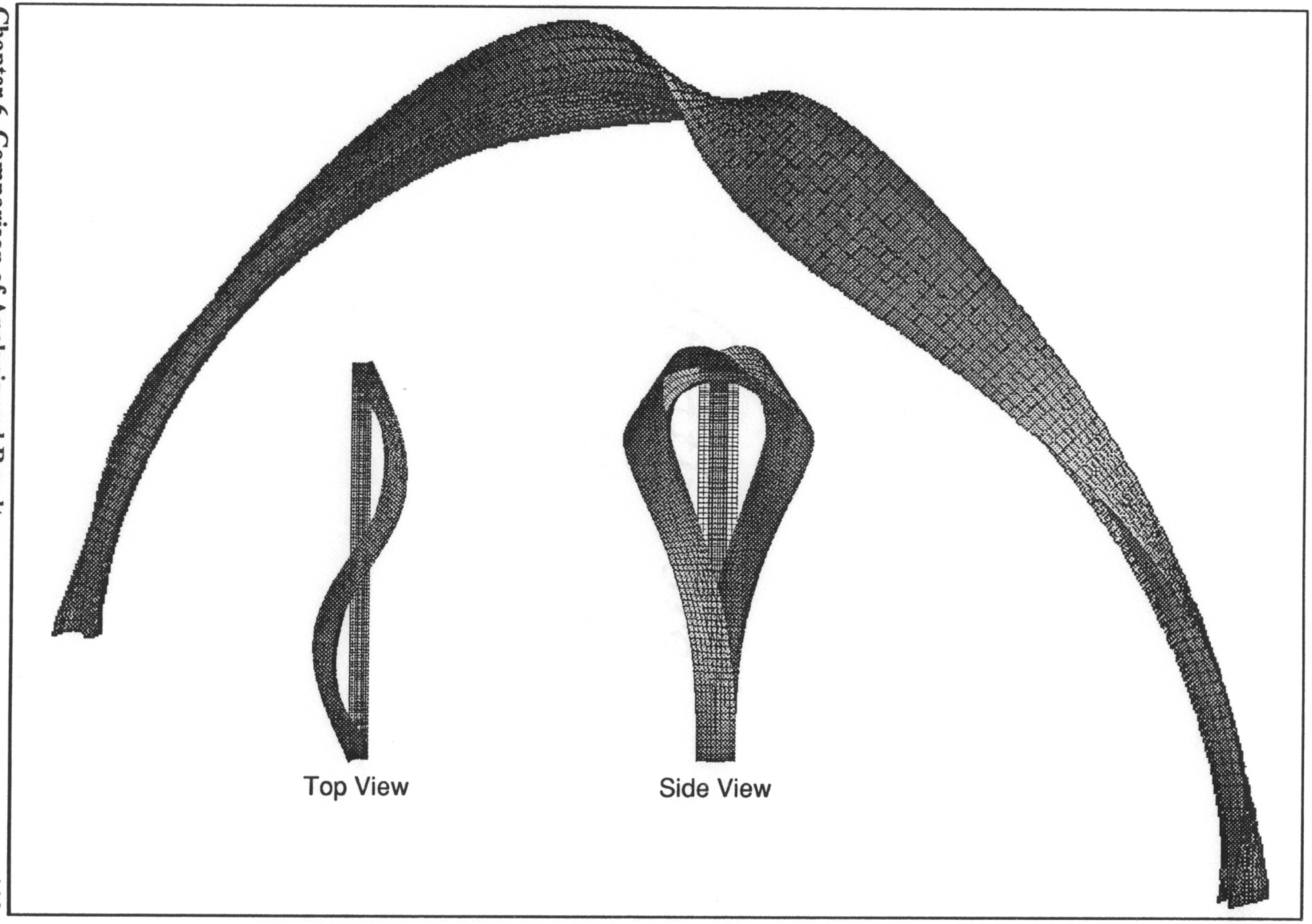

Fig. 6.9 FR001I-3 First Buckling Mode—Out-of-Plane Bending/Twisting

Fig. 6.10 FR0011-3 Second Buckling Mode—Localized Web/Cap Flange Crippling

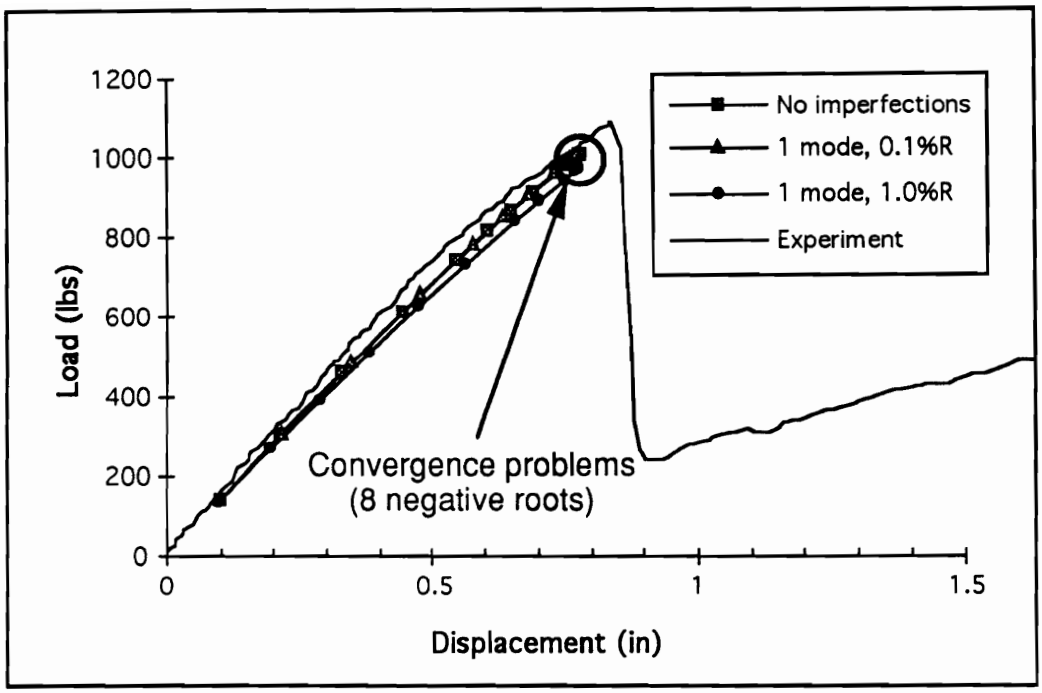

Fig. 6.11 Addition of Mode I Imperfections Does Not Stabilize FR001I-3 Response

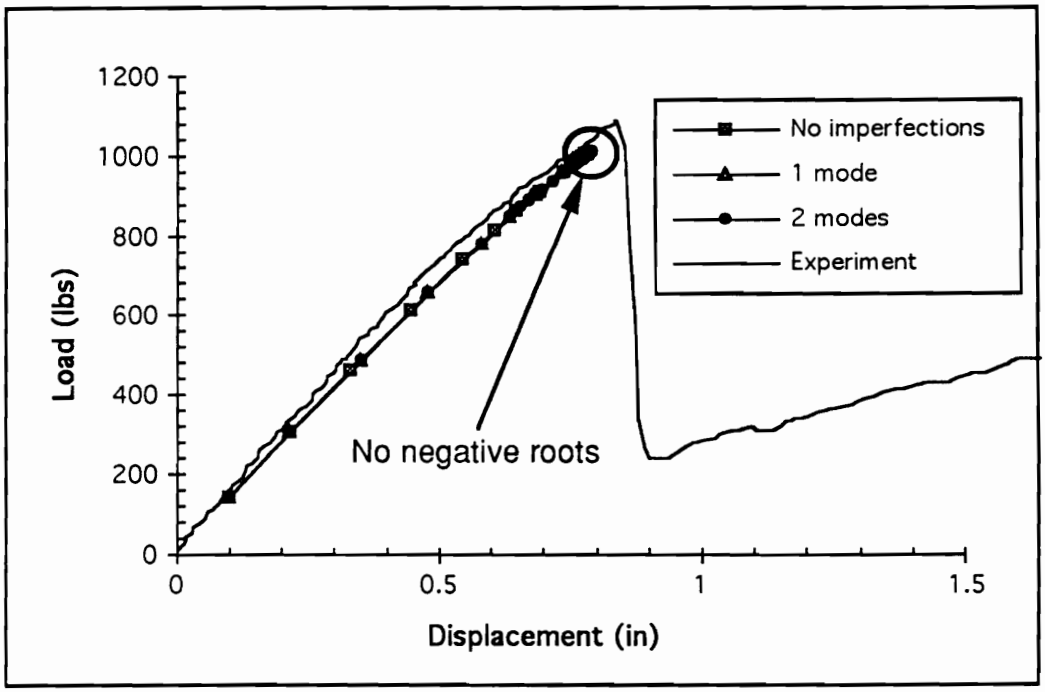

Fig. 6.12 Addition of Mode II Stabilizes FR001I-3 Response

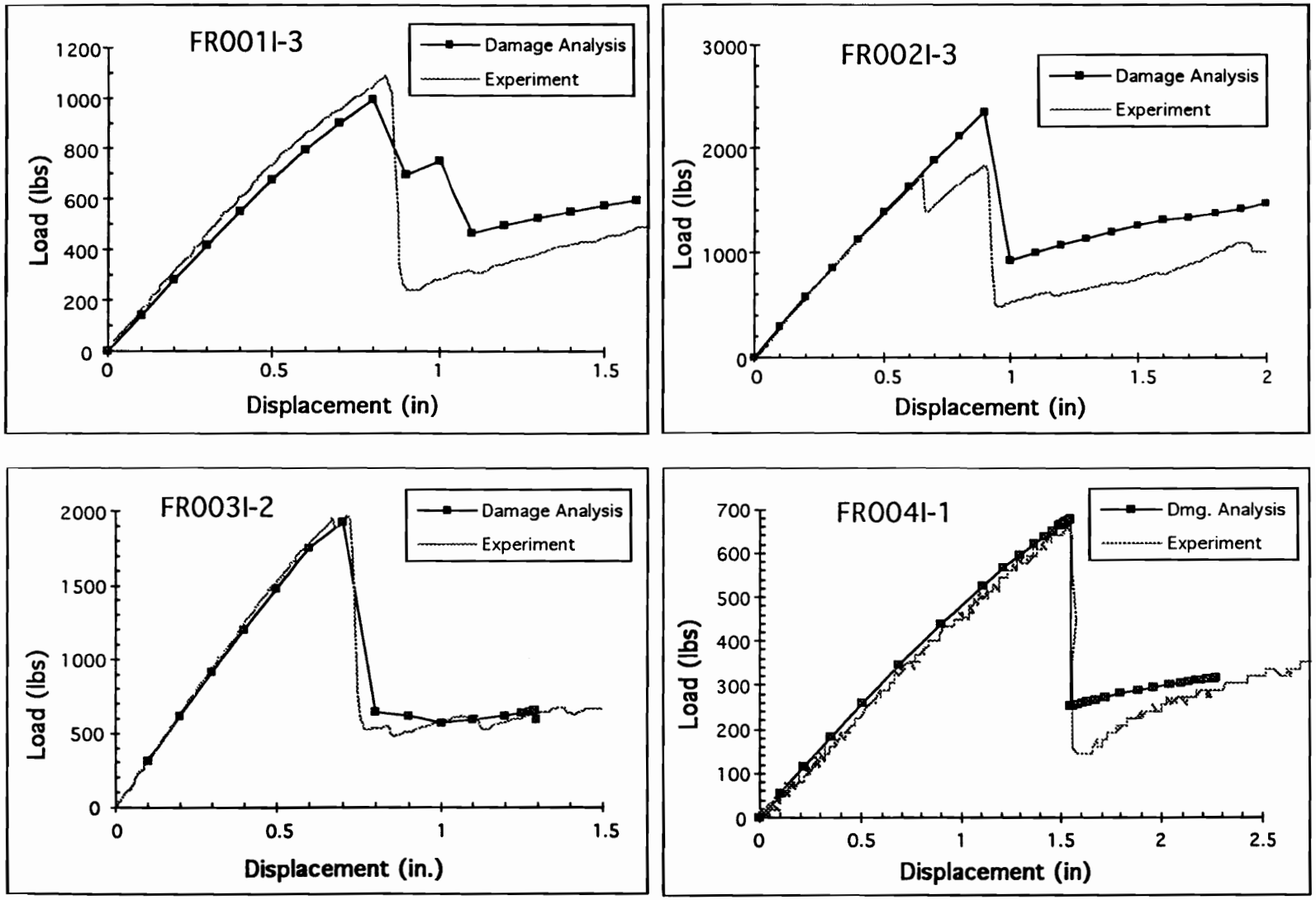

Fig. 6.13 Progressive Faiulure Analysis Compared to Experiment

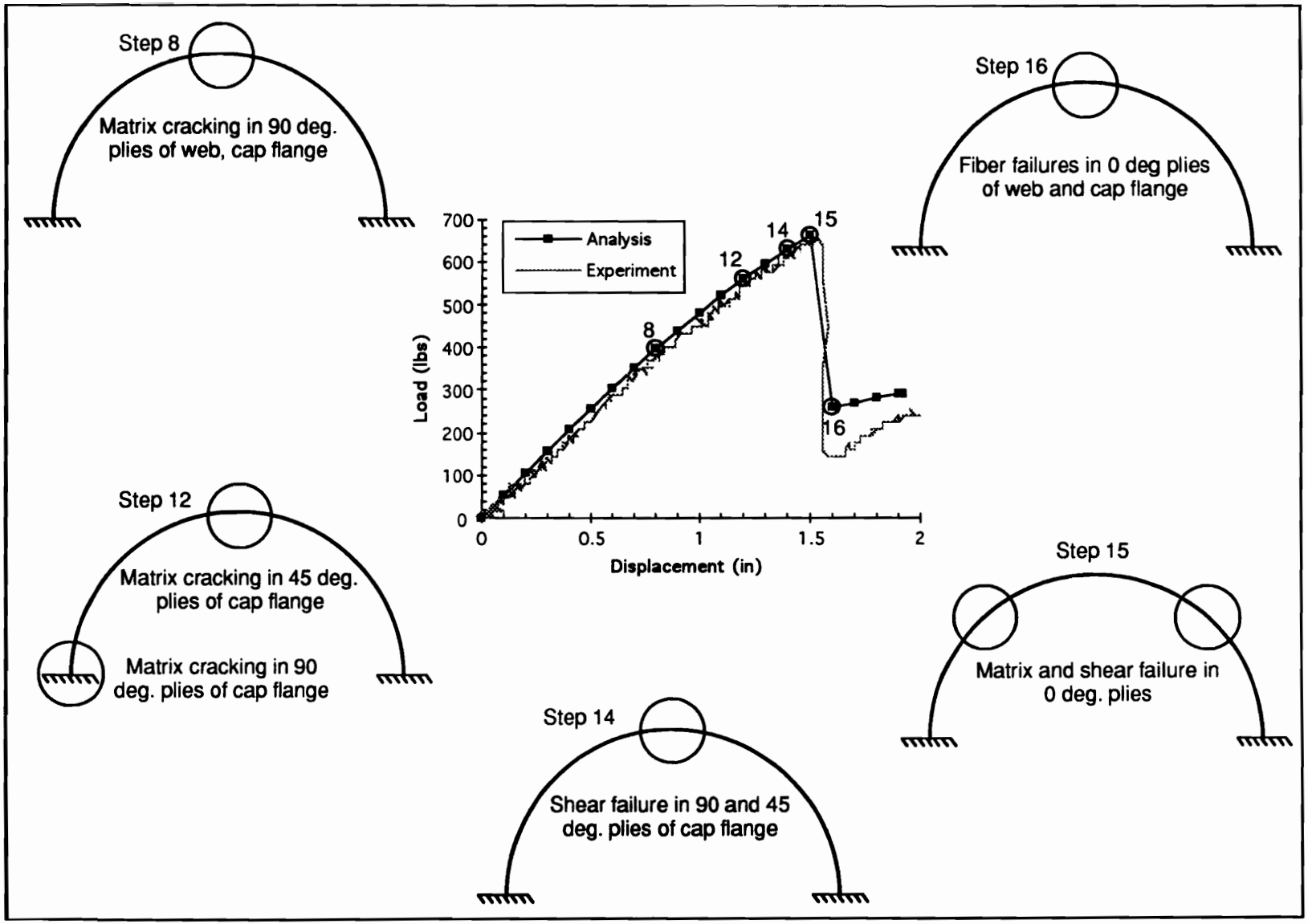

Fig. 6.14 Damage Development Predicted by Progressive Failure Analysis for Frame FR004I-1 (Maximum Strain Criterion with Ply Discount)

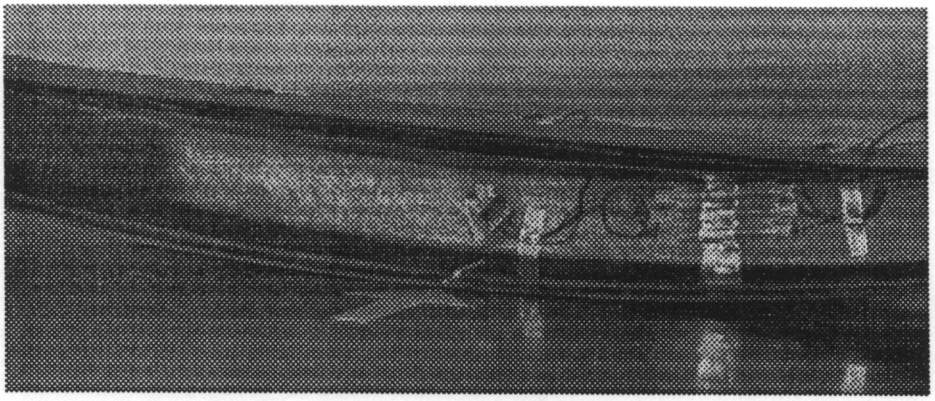

Fig. 6.15 Cap Flange Delamination

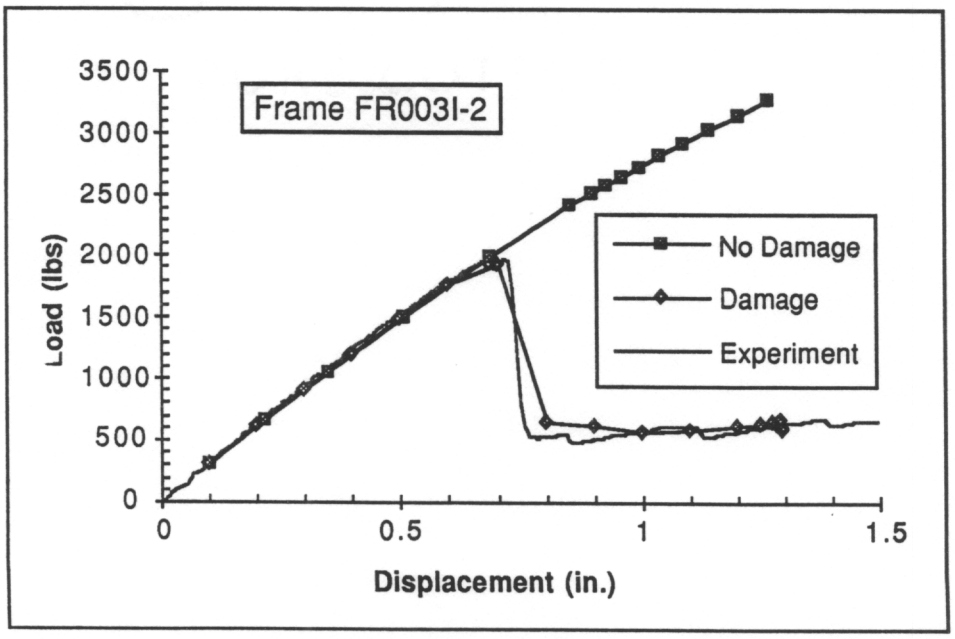

Fig. 6.16 Comparison of Analysis Results With and Without Damage

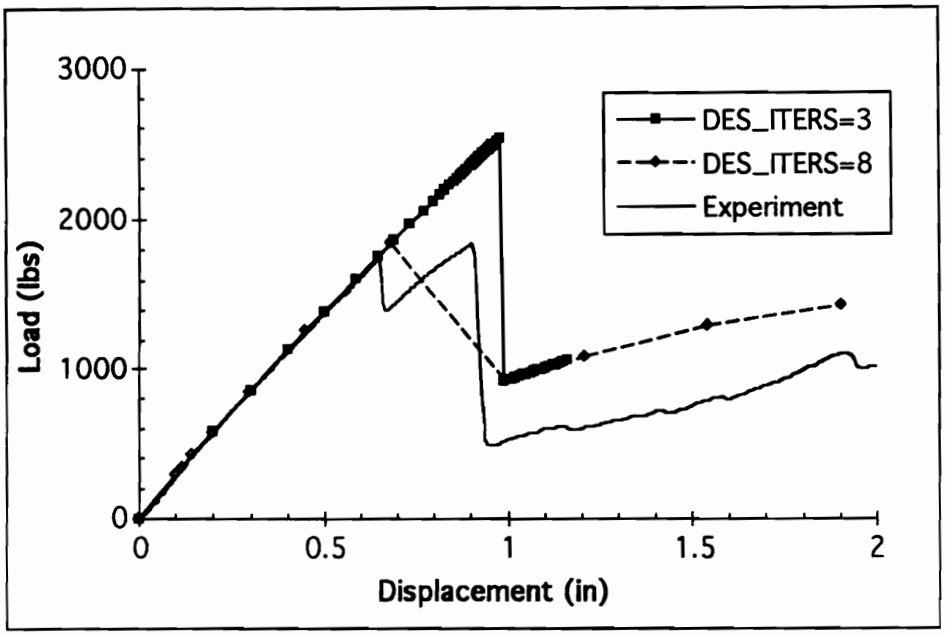

Fig. 6.17 Effect of DES_ITERS Nonlinear Analysis Contol Parameter

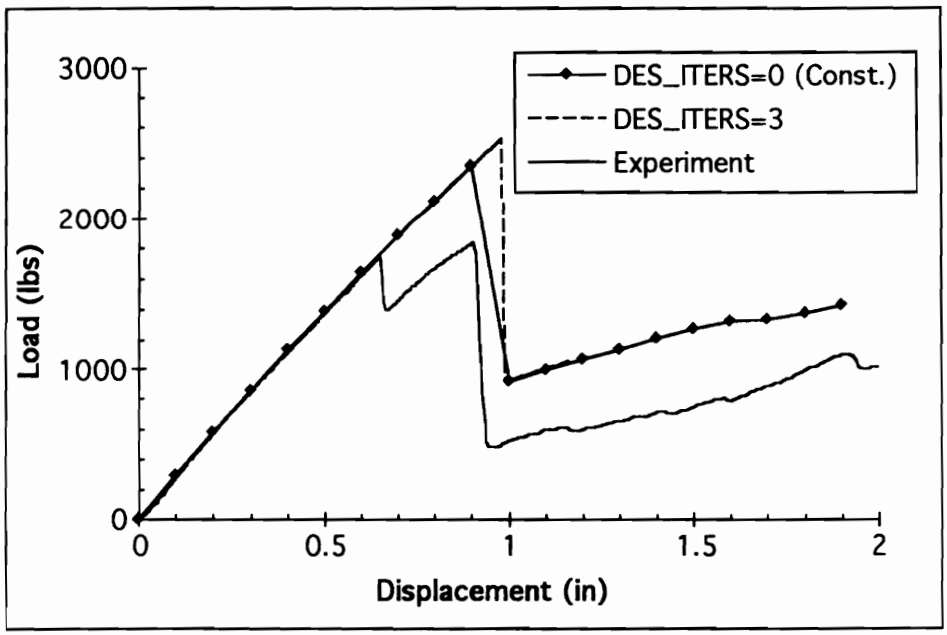

Fig. 6.18 Constant Load Step (DES_ITERS=0) Can Result in Poor Failure Load Prediction

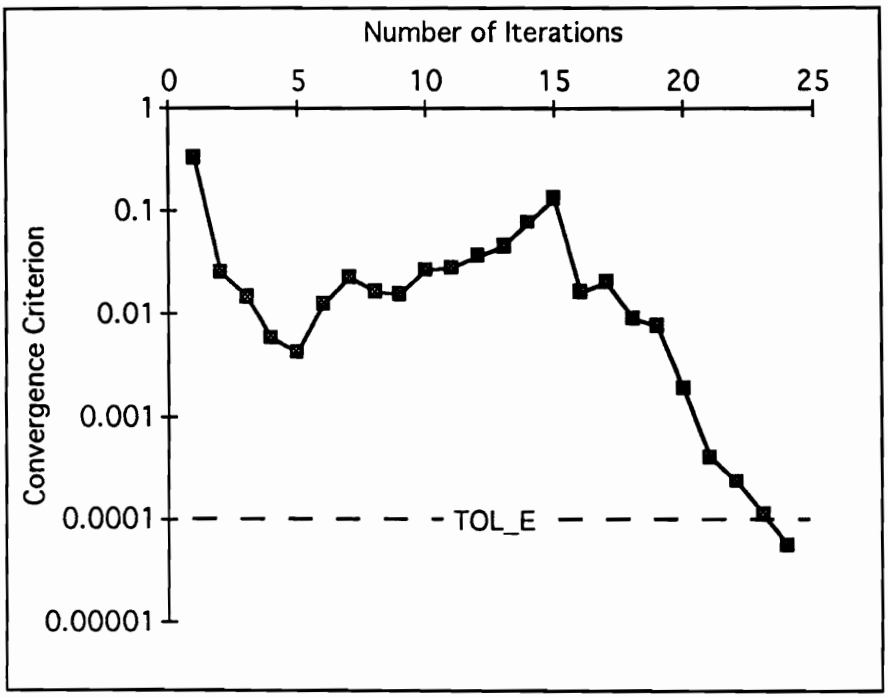

Fig. 6.19 Typical Error Convergence Behavior

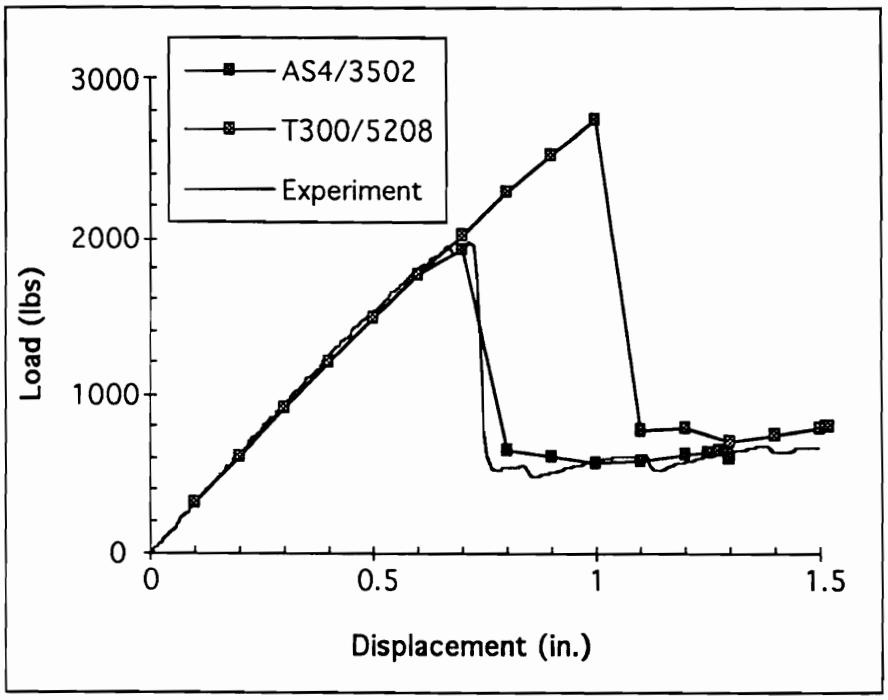

Fig. 6.20 Comparison of Damage Analysis for AS4/3502 and T300/5208

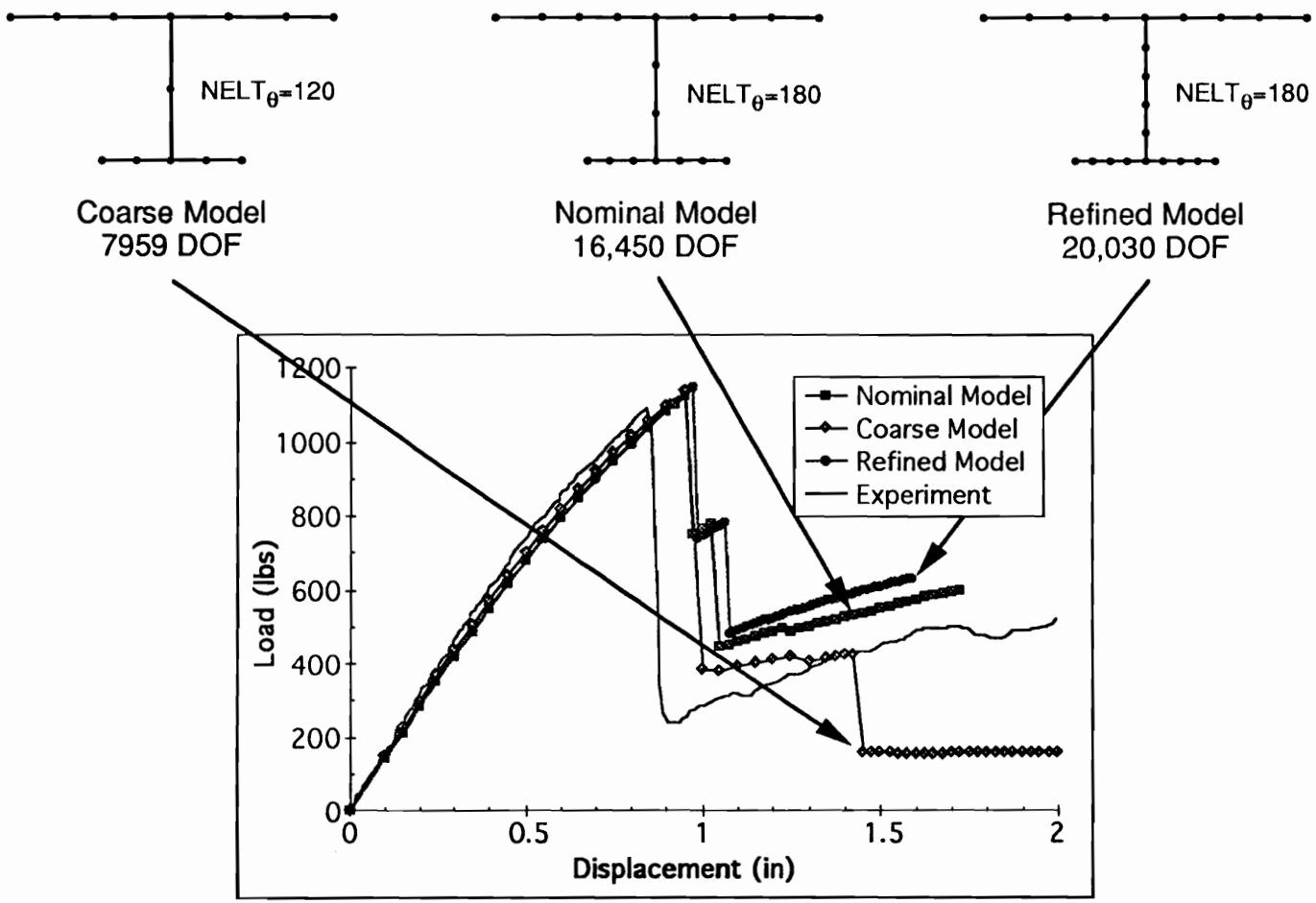

Fig. 6.21 Effect of Finite Element Mesh on Damage Analysis Results

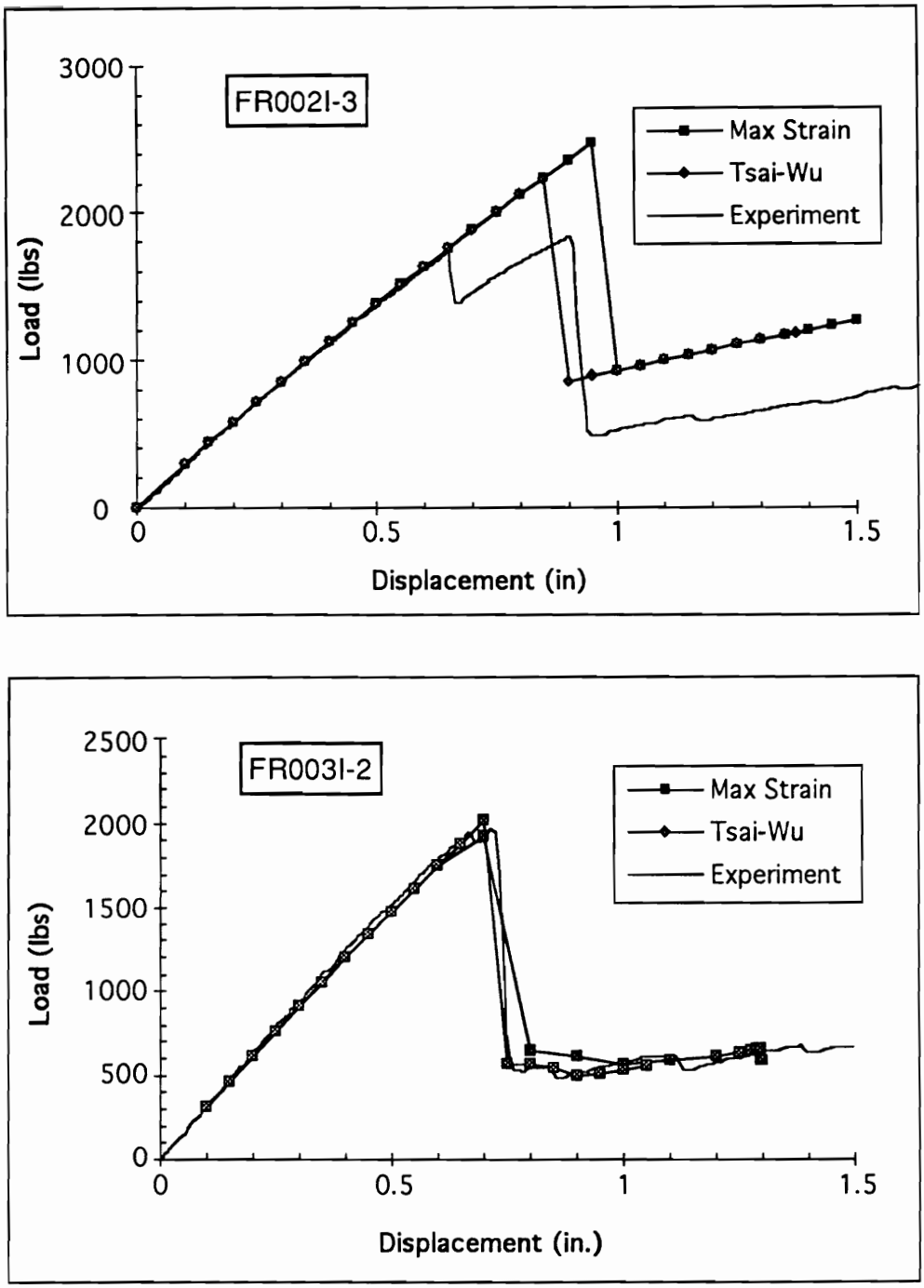

Fig. 6.22 Comparison of Maximum Strain and Tsai-Wu Failure Criteria

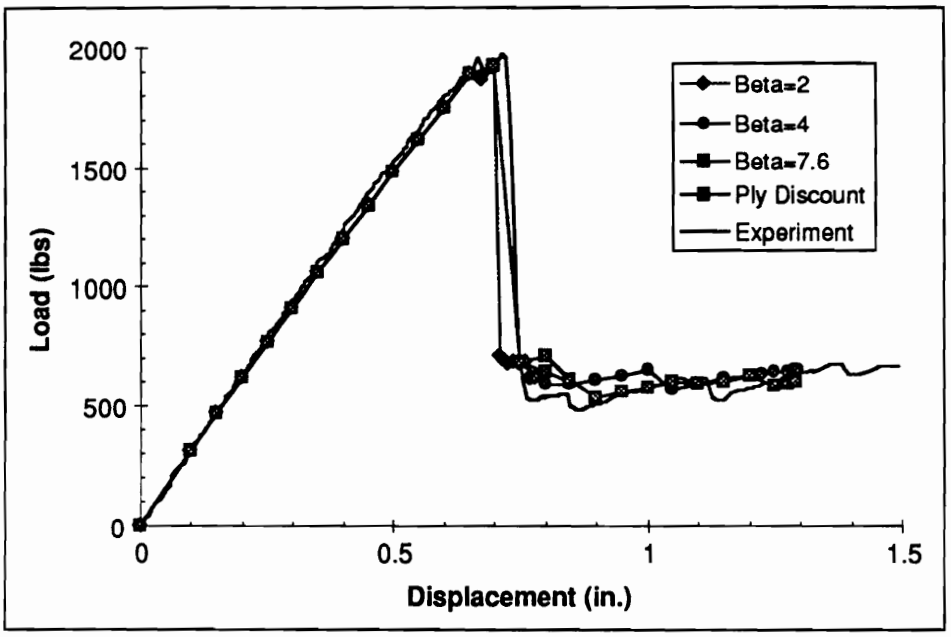

Fig. 6.23 Comparison of Discount and Statistical Strength Damage Models

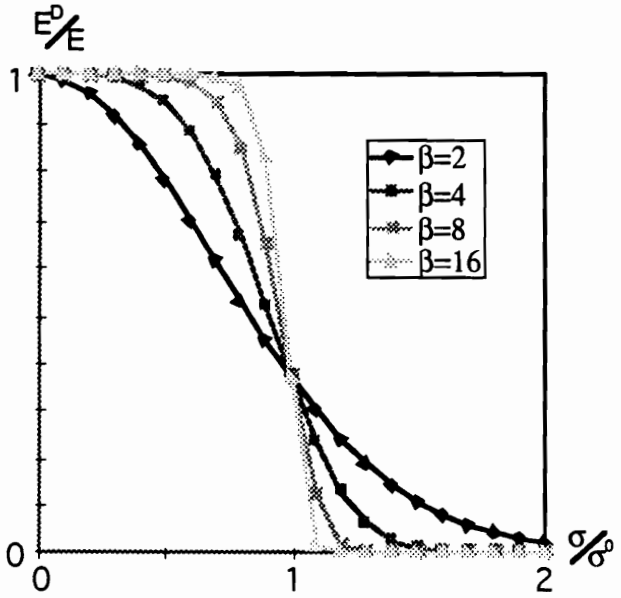

Fig. 6.24 Material Property Degradation in Statistical Strength Damage Model

CHAPTER 7
CONCLUDING REMARKS

7.1 Summary

A methodology for progressive failure analysis was presented that is applicable to thin composite structures undergoing large deformations. A nonlinear shell theory was developed based on the principle of virtual work using an updated Lagrangian formulation. An exact, incremental form of the three-dimensional variational principle was derived first; then consistent approximations of the nonlinear strain and constitutive tensors were introduced to linearize the governing equations. Kinematic approximations, equivalent to the Reissner-Mindlin plate theory, were used to reduce the three-dimensional theory to a two-dimensional form applicable to thin shell structures. This "resultant" form was stated in terms of the midsurface displacements and relative displacements (rotations), and through-thickness integrated stress resultants.

Damage models were described that predicted the onset of damage and subsequent constitutive behavior of the damaged material. Phenomenological failure criteria were used to predict damage initiation. These criteria rely on empirical

data and are efficient to calculate (due to the availability of the nonlinear strains in the formation of the geometric stiffness operator). The damage constitutive models were based on a linear, inelastic theory that included material degradatian, in which the physical properties are locally degraded to simulate loss of load-carrying capability. The use of the linear (Hookean) material description was consistent with the use of the incremental, updated Lagrangian formulation; the nonlinear stress and strain tensor are object tensors and their increments are linearly related.

A displacement-based finite element formulation was derived based on the incremental, linearized, resultant form of the principle of virtual work. An isoparametric formulation was used where both the geometry and deformations are approximated by the same interpolation functions. A C^0-continuous displacement field was assumed using Lagrange interpolating polynomials. The finite element formulation resulted in a system of nonlinear algebraic equations that approximated the scalar variational principle. The Newton-Raphson method was described for iteratively solving the nonlinear finite element equations; a load-stepping algorithm was introduced for automatically adjusting the step size during the analysis.

The finite element matrices were numerically integrated using two-dimensional Gauss quadrature. The constitutive matrices and stress resultants were numerically integrated (at each 2-D Gauss point) using a repeated Simpson's quadrature formula. The latter required the damage models to be evaluated at several material points within each ply, and allowed the damage to be localized within an element or ply. An added benefit was reduced sensitivity to the finite element mesh, since localized damage could still develop even in a coarse mesh.

The progressive failure methodolgy summarized above was implemented and tested in the Computational Structural Mechanics (CSM) Testbed. The damage models were implemented as nonlinear material models via the Generic Constitutive Processor. The finite element was implemented using the Generic Structural

Element Processor. The Testbed nonlinear solution procedure, NL_STATIC_1, was modified for the present study.

Six foot diameter graphite/epoxy frames—representative of ring stiffeners for rotorcraft fuselage—were tested in quasi-static crush tests that simulated crash loading of the rotorcraft. The frames were measured prior to testing to provide accurate dimensions for later analysis. The frames were crushed in a 120 KIP Baldwin testing machine in displacement-controlled tests. Displacement, load, and strains were measured throughout the test. Most of the tests were conducted at NASA Langley Research Center where a high speed data acquisition system (designed for impact tests) was used.

Finite element analyses of the graphite/epoxy frames were completed using the CSM Testbed to compare the progressive failure analysis with the experiments. Branched-shell finite element models were used where each component of the frame cross-section was discretized using the two-dimensional shell elements (*e.g.*, cap flange, web, attachment flange, skin). A convergence study was completed to determine an appropriate mesh for the model. Actual measurements of the frame cross-section and radius were used in the finite element model. The linear analysis of the frame showed that the results were very sensitive to these measurements. Excellent agreement in the linear stiffness was obtained when reliable frame measurements were available.

Good agreement between the analysis and experiment was also obtained in the nonlinear response (without damage) for both the load-deflection curve and the nonlinear strains. Two of the frame configurations, FR001I and FR004I, exhibited local buckling modes characterized by web and cap flange crippling. Imperfections in the shape of the first several buckling mode shapes were added to the frame finite element models for these two cases. The imperfections were necessary to stabilize

the nonlinear response and prevent the development of negative roots in the tangent matrix (indicating an unstable equilibrium path past a bifurcation point).

Excellent agreement was obtained between the progressive failure analysis and the experiments. Typically, damage initiated at the frame midspan as matrix cracking in the 90° plies of the web and cap flange, spread to the off-axis plies, and culminated with fiber failure in the load-bearing 0° plies. The analysis successfully predicted the failure load, the magnitude of unloading, and the residual stiffness of the frame after failure.

7.2 Guidelines for Progressive Failure Analysis

The following observations were made during numerical testing of the progressive failure analysis and may provide some insights to the analyst:

Material Failure Data

- The analysis was sensitive to the material failure data. Best results were obtained with data from a material system with the same fiber used in the frames, since the failure was fiber-dominated.

Failure Criterion

- Improved results were obtained with the Tsai-Wu failure criterion compared with the Maximum Strain criterion for the quasi-isotropic laminates. The combined stress criterion predicted fiber failure at a lower load, leading to an improved prediction of failure load and slightly improved prediction of the unloading that occurred at failure.

Convergence Behavior

- The redistribution of stresses during failure leads to oscillations of the nonlinear solution error before convergence. The `MAX_DIV` nonlinear solution control parameter, which forces a step cut if the error starts to rise, is not recommended since it leads to unnecessary step cuts.

- A large number of iterations may be required for convergence when the material is failing, especially for fiber-dominated failure modes. Setting `MAX_ITERS` to a large value is recommended, *e.g.*, `MAX_ITERS`=50.

Nonlinear Analysis Step Control

- Mixed results were obtained with the automatic load stepping algorithm controlled by `DES_ITERS`. A small value would lead to small load steps at failure, since invariably a large number of iterations was required to converge. However a benefit of the small load step was a good prediction of the failure load. Conversely a large value for `DES_ITERS` would lead to large load steps early in the analysis, and much poorer resolution of the load-deflection curve around the critical failure region.

Finite Element Mesh Effects

- The analysis was sensitive to the finite element mesh, however the effect diminished as the mesh was refined. The effect was most pronounced in the residual frame stiffness.

7.3 Conclusions

- The incremental, updated Lagrangian formulation provides a natural mechanism to incorporate damage models in a large deformation analysis. The use of objective stres/strain tensors that remain invariant under rigid body rotation admit the use of linearized constitutive relations in the formulation. Then the damage models can be expressed as linearized constitutive models that relate the incremental stresses and strains.

- Phenomenological failure criteria can be used to accurately predict the initiation of major failure events in stiffened structures. Both the Tsai-Wu and Maximum Strain criteria successfully predicted the failure load in tests of six-foot diameter, semi-circular graphite-epoxy I-frames subjected to compressive loading.

- Discount methods proved accurate for modeling the damaged material after failure was predicted. Stresses are effectively redistributed in the damaged material by reducing the physical properties. The progressive failure analysis correctly predicted the load drop and residual structural stiffness after failure in the frame experiments.

- Evaluating the damage models at each of the finite element quadrature points provides some mitigation of mesh effects in the analysis by allowing damage to be localized in a portion of the element.

- Accurate modeling was essential for obtaining good correlation between the progressive failure analysis and experiment, including material failure data and specimen geometry.

7.4 Recommendations for Future Studies

Damage Model

- Delamination clearly was a factor in the development of damage in the frame experiments but was not included in the analysis. The addition of delamination in the damage model may lead to significant improvement.
- The use of micromechanics-based damage models offers potentially improved prediction of failure initiation and damaged material properties, but remains computationally expensive. Parallel processing can be investigated as an option for efficiently implementing a micromechanics-based damage model.
- The present analysis assumed the material was linearly elastic until failure. Improved results may be obtained with a nonlinear material model, especially for modeling nonlinear shear stress-strain behavior.

Nonlinear Analysis

- The present study was limited by the lack of contact analysis capabilities, since the boundary conditions between the frame and load machine changed dramatically due to contact during the tests. The addition of contact analysis in COMET-AR is highly recommended.
- It is currently not possible to restart a materially nonlinear analysis in COMET-AR since the Generic Constitutive Processor (GCP) is unable to retrieve historical data from a previous converged step. The GCP should be modified to enable this capability.
- A "true" Newton's method was found to be effective by quickly redistributing stresses away from a damaged region. The nonlinear analysis may be optimized using a modified Newton's method in which only failed elements are recomputed

for each iteration, significantly decreasing the cost of reforming the tangent matrix.

- The use of an iterative solver may further improve performance in the nonlinear analysis.
- Investigate use of transient dynamic analysis for traversing the failure point in the equilibrium path; the dynamic response may initiate more damage than the static analysis, leading to improved prediction of unloading at failure.

Frame Modeling and Testing

- The frame finite element model convergence study was based on linear stiffness and strains. The convergence study should be extended to check stability analysis, *e.g.*, more refinement may be needed around the local crippling region.
- A simple solution for refining the frame model may be to use the strain distribution (or strain gradient) as a mesh scale factor, *i.e.*, increase the mesh density in regions of high strains or gradients.
- Using average measurements of the frame specimen dimensions led to significantly improved finite element analysis results. Better results may be obtained with spatially varying dimensions, *e.g.*, fitting the measured dimensions to some function that can be used to construct the finite element model. In addition to the cross-section dimensions, measured imperfections can be used to improve the nonlinear response of the thin-walled frames.
- The frame tests were inconclusive in showing the benefit of different potting methods. The frame response at the potted ends should be monitored in future tests to verify boundary conditions.

REFERENCES

Allen, D. H. (1994) "Damage Evolution in Laminates," in **Damage Mechanics of Composite Materials**, Composite Material Series, Vol. 9, edited by R. Talreja, Elsevier Science Publishers, pp. 79–116.

Averill, R. C. (1989) "On the Behavior of Shear Deformable Plate Elements," Master's Thesis, Virginia Polytechnic Institute and State University, Blacksburg, VA.

Averill, R. C. (1992) "Nonlinear Analysis of Laminated Composite Shells Using a Micromechanics-Based Progressive Damage Model," Ph.D. Dissertation, Virginia Polytechnic Institute and State University, Blacksburg, VA.

Barlow, J. (1976) "Optimal Stress Locations in Finite Element Models," *International Journal for Numerical Methods in Engineering*, Vol. 10, pp. 243–251.

Barlow, J. (1989) "More on Optimal Stress Points—Reduced Integration, Element Distortions and Error Estimation," *International Journal for Numerical Methods in Engineering*, Vol. 28, pp. 1487–1504.

Bathe, K.J. (1982) **Finite Element Procedures in Engineering Analysis**, Prentice-Hall, Inc., Englewood Cliffs, NJ.

Bathe, K.J. and Cimento, A.P. (1980) "Some Practical Procedures for the Solution of Nonlinear Finite Element Equations," *Computer Methods in Applied Mechanics and Engineering*, Vol. 22, pp. 59–85.

Bergan, P.G. and Søreide, T.H. (1977) "Solution of Large Displacement and Instability Problems Using the Current Stiffness Parameter," in **Finite Elements in Nonlinear Mechanics**, Tapir Publishers, Trondheim, Norway, pp. 647–669.

Bergan, P.G., Horrigmoe, G., Kråkeland, B. and Søreide, T.H. (1978) "Solution Techniques for Nonlinear Finite Element Problems," *International Journal for Numerical Methods in Engineering*, Vol. 12, pp. 1677–1696.

Chang, F.-K. and Chang, K.-Y. (1987a) "A Progressive Damage Model for Laminated Composites Containing Stress Concentrations," *Journal of Composite Materials*, Vol. 21, pp. 834–855.

Chang, F.-K. and Chang, K.-Y. (1987b) "Post-Failure Analysis of Bolted Composite Joints in Tension or Shear-Out Mode Failure," *Journal of Composite Materials*, Vol. 21, pp. 809–833.

Chang, F.-K. and Chen, M.-H. (1987) "The In Situ Ply Shear Strength Distributions in Graphite/Epoxy Laminated Composites," *Journal of Composite Materials*, Vol. 21, pp. 708–733.

Chang, F. K. and Kutlu, Z. (1989a) "Strength and Response of Cylindrical Composite Shells Subjected to Out-of-Plane Loadings," *Journal of Composite Materials*, Vol. 23, pp. 11–31.

Chang, F.-K. and Lessard, L. (1989b) "Modeling Compression Failure in Laminated Composite Plates Containing an Open Hole," Proceedings of the AIAA/ASME/-ASCE/AHS/ASC 30th Structures, Structural Dynamics and Materials Conference, Mobile, AL, April 3–5, pp. 979–988.

Collins, J. S. and Johnson, E. R. (1989) "Static and Free-Vibrational Response of Semi-Circular Graphite-Epoxy Frames with Thin-Walled Open Sections," Virginia Tech Center for Composite Materials and Structures Report No. CCMS-89-21.

The Computational Structural Mechanics Testbed Procedures Manual, compiled by C. B. Stewart, NASA TM 100646, 1991.

The Computational Structural Mechanics Testbed User's Manual, compiled by C. B. Stewart, NASA TM 100644, 1989.

Crisfield, M. A. (1981) "A Fast Incremental/Iterative Solution Procedure that Handles "Snap-Through"," *Computers and Structures*, Vol. 13, pp. 55-62.

Fung, Y. C. (1965) **Foundations of Solid Mechanics**, Prentice-Hall, Inc., Englewood Cliffs, NJ.

Gol'denblat, I. I. and V. A. Kopnov (1965) "Strength of Glass-Reinforced Plastics in Complex Stress States," *Mekhanika Polimerov*, Vol. 1, p. 70; English translation: *Polymer Mechanics*, Vol. 1 (1966), pp. 54–59.

Green, A. E. and Zerna, W. (1968) **Theoretical Elasticity**, Second Edition, Oxford University Press, New York.

Grimes, G. C. and Whitney, J. M. (1974) " Degradation of Graphite/epoxy Composite Materials Because of Load Induced Micromechanical Damage," *SAMPE Quarterly*, Vol. 5, No. 4, pp. 1–13.

Gücer, D. E. and Gurland, J. (1962) "Comparison of the Statistics of Two Fracture Modes," *Journal of the Mechanics and Physics of Solids*, Vol. 10, pp. 365–373.

Hahn, H. T. and Tsai, S. W. (1973) "Nonlinear Elastic Behavior of Unidirectional Composite Laminae," *Journal of Composite Materials*, Vol. 7, pp. 102–118.

Humphreys, E. A. (1981) "Development of an Engineering Analysis of Progressive Damage in Composites During Low Velocity Impact," NASA CR 165778, July, 1981.

Hughes, T. J. R. (1987) **The Finite Element Method**, Prentice-Hall, Inc., Englewood Cliffs, NJ.

Johnson, L. W. and Riess, R. D. (1982) *Numerical Analysis*, Second Edition, Addison-Wesley Publishing Company, Reading, Massachusetts.

Jones, R. M. (1975) *Mechanics of Composite Materials*, Hemisphere Publishing Corporation, New York.

Lee, J. D. (1982) "Three Dimensional Finite Element Analysis of Damage Accumulation in Composite Laminate," *Computers and Structures*, Vol. 15, No. 3, pp. 335–350.

Malvern, L. E. (1969) **Introduction to the Mechanics of a Continuous Medium**, Prentice-Hall, Inc., Englewood Cliffs, NJ.

McConnell, A. J. (1957) **Applications of Tensor Analysis**, Dover Publications, New York.

McCormick, R. F., Spears, J. C., Lynch, J. W., and Batten, F. R. (1982) "Data Acquisition System for NASA LaRC Impact Dynamics Research Facility," NASA TM 84510.

Metcalfe, A. G. and Schmitze, G. K. (1964) "Effect of Length on the Strength of Glass Fibers," ASTM Preprint No. 87.

MIL-HDBK-17-2C (1994) "Polymer Matrix Composites, Volume II. Material Properties," Standardization Documents Order Desk, Department of Defense, Philadelphia.

Mindlin, R. D. (1951) "Influence of Rotary Inertia and Shear on Flexural Motions of Isotropic, Elastic Plates," *Journal of Applied Mechanics*, Vol. 18, pp. 31–38.

Nahas, M. N. (1986) "Survey of Failure and Post-Failure Theories of Laminated Fiber-Reinforced Composites," *Journal of Composites Technology and Research*, Vol. 8, No. 4, pp. 138–153.

Narayanaswami, R. and Adelman, H. M. (1977) "Evaluation of the Tensor Polynomial and Hoffman Strength Theories for Composite Materials," *Journal of Composite Materials*, Vol. 11, pp. 366–377.

O'Brien, T. K. (1990) "Towards a Damage Tolerance Philosophy for Composite Materials and Structures," *Composite Materials: Testing and Design (Ninth Volume), ASTM STP 1059*, S. P. Garbo, Ed., American Society for Testing and Materials, Philadelphia, pp. 7–33.

Pandey, A. K. (1987) "A Nonlinear Computational Model for the Strength and Failure of Composite Plates and Shells," Ph. D. Dissertation, Virginia Polytechnic Institute and State University, Blacksburg, VA.

Pandey, A. K. and Reddy, J. N. (1987) "A Post First-Ply Failure Analysis of Composite Laminates," Proceedings of the AIAA/ASME/ASCE/AHS 28th Structures, Structural Dynamics and Materials Conference, Monterey, CA, April 6–8, pp. 788–797.

Petit, P. H. and Waddoups, M. E. (1969) "A Method of Predicting the Nonlinear Behavior of Laminated Composites," *Journal of Composite Materials*, Vol. 3, pp. 2–19.

Pipes, R. B. and Cole, B. W. (1973) "On the Off-Axis Strength Test for Anisotropic Materials," *Journal of Composite Materials*, Vol. 7, pp. 246–256.

Ramm, E. (1980) "Strategies for Tracing the Nonlinear Response Near Limit Points," Proceedings of the Europe-U.S. Workshops, edited by Wunderlich, et. al., pp. 63–89.

Reddy, J. N. (1984) **An Introduction to the Finite Element Method**, McGraw-Hill Book Co., New York.

Reifsnider, K. L., Henneke, E. G., Stinchcomb, W. W., and Duke, J. C. (1982) "Damage Mechanics and NDE of Composite Laminates," *Mechanics of Composite Materials, Proceedings of the IUTAM Symposium on Mechanics of Composite Materials*, Z. Hashin and C. T. Herakovich, Eds., Blacksburg, VA., pp. 399–420.

Reissner, E. (1944) "On the Theory of Bending of Elastic Plates," *Journal of Mathematics and Physics*, Vol. 23, pp. 184–191.

Reissner, E. (1945) "The Effects of Transverse Shear Deformation on the Bending of Elastic Plates," *Journal of Applied Mechanics*, Vol. 12, pp. 69–77.

Rosen, B. W. (1965) "Mechanics of Composite Strengthening," in *Fiber Composite Materials*, American Society for Metals, Metals Park, OH, Chapter 3.

Sandhu, R. S. (1974) "Ultimate Strength Analysis of Symmetric Laminates," Report No. AFFDL-TR-73-137, Air Force Flight Dynamics Laboratory, Wright-Patterson Air Force Base, OH.

Sensmeier, M. D., Griffin, O. H., and Johnson, E. R. (1988) "Static and Dynamic Large Deflection Flexural Response of Graphite-Epoxy Beams," NASA CR 4118.

Shivakumar, K. N., Elber, W., and Illg, W. (1983) "Analysis of Progressive Damage in Thin Circular Laminates Due to Static-Equivalent Impact Loads," Proceedings of the AIAA/ASME/ASCE/AHS 24th Structures, Structural Dynamics and Materials Conference, Lake Tahoe, NV, May 2–4, pp. 606–615.

Sokolnikoff, I. S. (1956) **Mathematical Theory of Elasticity**, McGraw-Hill Book Co., New York.

Stanley, G. M. (1985) "Continuum-Based Shell Elements," Ph.D. Dissertation, Stanford University, Palo Alto, CA.

Stanley, G. M. and Nour-Omid, S. (1990) "The Computational Structural Mechanics Testbed Generic Structural-Element Processor Manual," NASA CR 181728.

Stricklin, J.A., Haisler, W.E. and von Riesemann, W.A. (1973) "Evaluation of Solution Procedures for Material and/or Geometrically Nonlinear Structural Analysis," *A.I.A.A Journal*, Vol. 11, pp. 292-299.

Stuart, M., Private Communication, CYTEK Engineered Materials, Inc., Anaheim, California, January 10, 1996.

Truesdell, C. and Toupin, R. A. (1960) "The Classical Field Theories," in *Encyclopedia of Physics*," edited by S. Flügge, Vol. III/1, pp. 226–793, Springer-Verlag, Berlin.

Tsai, S. W. (1988) "Design Limit and Ultimate Strengths of Laminates," Section 12, *Composite Design*, 4th Ed., Think Composites, Dayton, OH.

Tsai, S. W. and Hahn, H. T. (1980) *Introduction to Composite Materials*, Technomic Publishing Co., Lancaster, PA.

Tsai, S. W. and Wu, E. M. (1971) "A General Theory of Strength for Anisotropic Materials," *Journal of Composite Materials*, Vol. 5, pp. 58–80.

Weibull, W. (1951) "A Statistical Distribution Function of Wide Applicability," *Journal of Applied Mechanics*, Vol. 18, pp. 293–297.

Whitney, J. M. (1973) "Shear Correction Factors for Orthotropic Laminates Under Static Load," *Journal of Applied Mechanics*, Vol. 40, No. 1, pp. 302–304.

Woodson, M. B. (1994) "Optimal Design of Composite Fuselage Frames for Crashworthiness," Ph.D. Dissertation, Virginia Polytechnic Institute and State University, Blacksburg, VA.

Wu, E. (1974) "Phenomenological Anisotropic Failure Criterion," in **Mechanics of Composite Materials**, Composite Materials Series, Vol. 2, edited by G. P. Sendeckyj, Academic Press, New York, pp. 353–431.

Yamada, S. E. and Sun, C. T. (1978) "Analysis of Laminated Strength and Its Distribution," *Journal of Composite Materials*, Vol. 12, pp. 275–284.

Zienkiewicz, O. C. (1977) *The Finite Element Method*, Third Ed., McGraw-Hill Book Co., New York.

APPENDIX A
GREEN-LAGRANGE (GL) STRAIN TENSOR

Consider the two line segments shown in Fig. A.1. In the initial configuration, the endpoints of the line segment are given by $X_i, X_i + dX_i$, and the length of the line segment is $(dS)^2 = dX_i\, dX_i$. After deformation, the line segment translates, rotates and stretches so the endpoints are given by $x_i, x_i + dx_i$, and the length is $(ds)^2 = dx_i\, dx_i$.

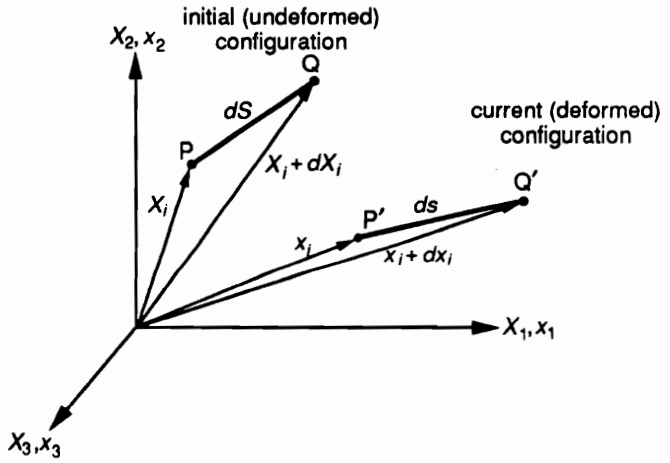

Fig. A.1 Line Segments in Deformed and Undeformed Configurations

The change in length of the line segment from the initial to the current configuration is given by:

$$(ds)^2 - (dS)^2 = dx_i\, dx_i - dX_i\, dX_i \qquad \text{(A-1)}$$

The components dx_i of the line vector in the current configuration can be expressed in terms of the those in the initial configuration by introducing the deformation gradient,

$$\begin{aligned} \boldsymbol{\mathcal{X}} &= (\boldsymbol{\nabla} \mathbf{x})^T \\ \mathcal{X}_{ij} &= \frac{\partial x_i}{\partial X_j} \end{aligned} \tag{A-2}$$

Then using the chain rule, the components dx_i in the current configuration can be written as:

$$dx_i = \frac{\partial x_i}{\partial X_j} dX_j = \mathcal{X}_{ij}\, dX_j \tag{A-3}$$

Thus the deformation gradient transforms the line segment from the initial configuration to the current one, and accounts for both the rigid-body motion and stretching of the line segment. Substituting Eq. A-3 in A-1 yields:

$$\begin{aligned} (ds)^2 - (dS)^2 &= (\mathcal{X}_{ri}\mathcal{X}_{rj}\, dX_i\, dX_j - dX_i\, dX_i) \\ &= (\mathcal{X}_{ri}\mathcal{X}_{rj} - \delta_{ij})\, dX_i\, dX_j \end{aligned} \tag{A-4}$$

The components $\mathcal{X}_{ri}\mathcal{X}_{rj}$ are recognized as the component form of the right Cauchy-Green deformation tensor, $\boldsymbol{\mathcal{C}} = \boldsymbol{\mathcal{X}}^T \boldsymbol{\mathcal{X}}$, so that

$$(ds)^2 - (dS)^2 = (\mathcal{C}_{ij} - \delta_{ij})\, dX_i\, dX_j \tag{A-5}$$

The Green-Lagrange strain tensor, ϵ_{ij}, referred to the initial configuration, is defined as:

$$2\epsilon_{ij}\, dX_i\, dX_j = (ds)^2 - (dS)^2 \tag{A-6}$$

The strain tensor can be expressed elegantly as a function of the right Cauchy-Green deformation tensor,

$$\begin{aligned} \boldsymbol{\epsilon} &= \tfrac{1}{2}(\boldsymbol{\mathcal{C}} - \mathbf{I}) \\ \epsilon_{ij} &= \tfrac{1}{2}(\mathcal{C}_{ij} - \delta_{ij}) \end{aligned} \tag{A-7}$$

or alternatively in terms of the deformation gradient,

$$\begin{aligned} \boldsymbol{\epsilon} &= \tfrac{1}{2}(\boldsymbol{\mathcal{X}}^T \boldsymbol{\mathcal{X}} - \mathbf{I}) \\ \epsilon_{ij} &= \tfrac{1}{2}(\mathcal{X}_{ri}\mathcal{X}_{rj} - \delta_{ij}) \end{aligned} \tag{A-8}$$

However, in anticipation of using a displacement-based finite element method to solve the nonlinear equations derived from the principle of virtual work, we seek to express the strain tensor in terms of the displacement vector, $\mathbf{u}$, defined as $x_i = u_i + X_i$. Then the deformation gradient becomes

$$\begin{aligned} \mathcal{X} &= (\nabla \mathbf{x})^T = (\nabla \mathbf{u} + \mathbf{I})^T \\ \mathcal{X}_{ij} &= \frac{\partial x_i}{\partial X_j} = \frac{\partial u_i}{\partial X_j} + \delta_{ij} \end{aligned} \tag{A-9}$$

and substituting this result in Eq. A-8 yields the Green-Lagrange strain tensor in terms of the current deformation:

$$\begin{aligned} \boldsymbol{\epsilon} &= \tfrac{1}{2}\Big((\nabla \mathbf{u}) + (\nabla \mathbf{u})^T + (\nabla \mathbf{u})(\nabla \mathbf{u})^T\Big) \\ \epsilon_{ij} &= \tfrac{1}{2}\left(\frac{\partial u_i}{\partial X_j} + \frac{\partial u_j}{\partial X_i} + \frac{\partial u_r}{\partial X_i}\frac{\partial u_r}{\partial X_j}\right) \end{aligned} \tag{A-10}$$

Several important points can be made about the Green-Lagrange strain tensor:

(1) it is symmetric,

(2) it is exact for any deformation,

(3) it is invariant under rigid-body rotation.

The invariance of the strain tensor can be proven using the polar decomposition theorem for the deformation gradient, which is derived in Appendix D. The theorem states that the deformation gradient can be decomposed as $\mathcal{X} = \mathbf{RU}$, where $\mathbf{U}$ is a symmetric matrix describing the stretching, and $\mathbf{R}$ is an orthogonal matrix describing the rotation of the line segment. Substituting $\mathcal{X} = \mathbf{RU}$ in Eq. A-8 yields

$$\boldsymbol{\epsilon} = \tfrac{1}{2}(\mathbf{U}^T\mathbf{R}^T\mathbf{RU} - \mathbf{I}) \tag{A-11}$$

But $\mathbf{R}$ is orthogonal, so $\mathbf{R}^T\mathbf{R} = \mathbf{I}$, and $\boldsymbol{\epsilon}$ becomes

$$\boldsymbol{\epsilon} = \tfrac{1}{2}(\mathbf{U}^T\mathbf{U} - \mathbf{I}) \tag{A-12}$$

Thus $\boldsymbol{\epsilon}$ represents the strain due to only stretching of the line segment and remains invariant under rotation or rigid-body motion.

APPENDIX B
SECOND PIOLA-KIRCHHOFF (2PK) STRESS TENSOR

The force vector acting on an infinitesimal surface area of the current configuration due to the Cauchy stresses τ_{ij} is shown in Fig. B.1, and can be written by Cauchy's formula as:

$$\begin{aligned} d\mathbf{t} &= \boldsymbol{\tau}\, {}^t\mathbf{n}\, {}^t dS \\ dt_i &= \tau_{ij}\, {}^t n_j\, {}^t dS \end{aligned} \tag{B-1}$$

where ${}^t\mathbf{n}$ is the normal to the surface ${}^t dS$ in the current configuration.

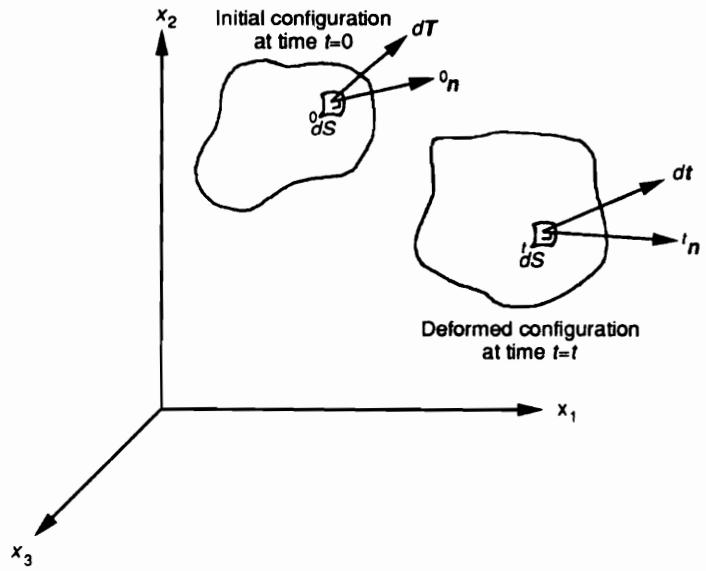

Fig. B.1 Force Vectors Due to 2PK and Cauchy Stresses

Now define a force vector $d\mathbf{T}$ acting on the surface ${}^0dS$ which is the original configuration of ${}^tdS$, as shown in Fig. B.1, and is related to $d\mathbf{t}$ by:

$$\begin{aligned} d\mathbf{T} &= \boldsymbol{\mathcal{X}}^{-1} d\mathbf{t} \\ dT_i &= \mathcal{X}_{ij}^{-1} dt_j = \frac{\partial X_i}{\partial x_j} dt_j \end{aligned} \tag{B-2}$$

where $\boldsymbol{\mathcal{X}}^{-1}$ is the inverse of the deformation gradient. Eq. B-2 can be interpreted to mean that the force $d\mathbf{t}$ is "stretched and rotated in the same way that $d\mathbf{x}$ is stretched and rotated to obtain $d\mathbf{X}$" [Bathe, 1982]. The force $d\mathbf{T}$ balances the components of the second Piola-Kirchhoff stress tensor:

$$\begin{aligned} d\mathbf{T} &= \boldsymbol{\sigma}\, {}^0\mathbf{n}\, {}^0dS \\ dT_i &= \sigma_{ij}\, {}^0n_j\, {}^0dS \end{aligned} \tag{B-3}$$

Next, the components of σ_{ij} and τ_{ij} can be related by introducing Nanson's formula:

$$\begin{aligned} {}^t\mathbf{n}\, {}^tdS &= \frac{{}^0\rho}{{}^t\rho} (\boldsymbol{\mathcal{X}}^{-1})\, {}^0\mathbf{n}\, {}^0dS \\ {}^tn_i\, {}^tdS &= \frac{{}^0\rho}{{}^t\rho} (\mathcal{X}_{ij}^{-1})\, {}^0n_j\, {}^0dS \end{aligned} \tag{B-4}$$

where ${}^0\rho$,${}^t\rho$ are densities in the original and current configurations, respectively. Substituting Eqs. B-3 and B-4 in B-2 yields:

$$\begin{aligned} \left(\boldsymbol{\sigma} - \frac{{}^0\rho}{{}^t\rho} (\boldsymbol{\mathcal{X}}^{-1})\, \boldsymbol{\tau} (\boldsymbol{\mathcal{X}}^{-1})^T\right) {}^0\mathbf{n}\, {}^0dS = 0 \\ \left(\sigma_{ij} - \frac{{}^0\rho}{{}^t\rho} \frac{\partial X_i}{\partial x_m} \tau_{mn} \frac{\partial X_j}{\partial x_n}\right) {}^0n_j\, {}^0dS = 0 \end{aligned} \tag{B-5}$$

However, Eq. B-5 must be valid for any surface area, so the term in parenthesis must vanish. Then the components of the second Piola-Kirchhoff stress tensor are related to the Cauchy stress tensor as:

$$\begin{aligned} \boldsymbol{\sigma} &= \frac{{}^0\rho}{{}^t\rho} (\boldsymbol{\mathcal{X}}^{-1})\, \boldsymbol{\tau} (\boldsymbol{\mathcal{X}}^{-1})^T \\ \sigma_{ij} &= \frac{{}^0\rho}{{}^t\rho} \frac{\partial X_i}{\partial x_m} \tau_{mn} \frac{\partial X_j}{\partial x_n} \end{aligned} \tag{B-6}$$

Two important points can be made about σ_{ij}. First, since τ_{ij} is symmetric, then σ_{ij} is symmetric as well. Second, σ_{ij} is invariant to rigid body rotations. In this case the deformation gradient $\boldsymbol{\mathcal{X}} = \mathbf{RU}$ reduces to the rotation tensor $\mathbf{R}$, since $\mathbf{U} = \mathbf{I}$ (see Appendix D).

The ratio ${}^0\rho/{}^t\rho$ in Eq. B-6 can be computed from conservation of mass:

$$ {}^t\rho\, {}^tdV = {}^0\rho\, {}^0dV \tag{B-7}$$

Define an infinitesimal volume element that is bounded by $d\mathbf{X}^1, d\mathbf{X}^2, d\mathbf{X}^3$. Then the volume of this element in the initial configuration is

$$ {}^0dV = (d\mathbf{X}^1 \times d\mathbf{X}^2) \cdot d\mathbf{X}^3 = \epsilon_{ijk}\, d\mathbf{X}^1_i\, d\mathbf{X}^2_j\, d\mathbf{X}^3_k \tag{B-8}$$

where ϵ_{ijk} is the permutation symbol. After deforming to the current configuration, the line segments bounding the infinitesimal volume are transformed to $d\mathbf{x}^1, d\mathbf{x}^2, d\mathbf{x}^3$ by the deformation gradient, *i.e.*, $dx_i = \mathcal{X}_{ij}\, dX_j$. Then the volume in the current configuration becomes

$$\begin{aligned} {}^tdV = (d\mathbf{x}^1 \times d\mathbf{x}^2) \cdot d\mathbf{x}^3 &= \epsilon_{ijk}\, d\mathbf{x}^1_i\, d\mathbf{x}^2_j\, d\mathbf{x}^3_k \\ &= \epsilon_{ijk}\mathcal{X}_{il}\mathcal{X}_{jm}\mathcal{X}_{kn}\, d\mathbf{X}^1_l\, d\mathbf{X}^2_m\, d\mathbf{X}^3_n \end{aligned} \tag{B-9}$$

But $\epsilon_{ijk}\mathcal{X}_{il}\mathcal{X}_{jm}\mathcal{X}_{kn} = \epsilon_{lmn}\det(\boldsymbol{\mathcal{X}})$ [McConnell, 1957], so

$$\begin{aligned} {}^tdV &= \det(\boldsymbol{\mathcal{X}})\, \epsilon_{lmn}\, d\mathbf{X}^1_l\, d\mathbf{X}^2_m\, d\mathbf{X}^3_n \\ &= \det(\boldsymbol{\mathcal{X}})\, {}^0dV \end{aligned} \tag{B-10}$$

Comparing Eqs. B-7 and B-10 reveals that

$$ \frac{{}^0\rho}{{}^t\rho} = \det(\boldsymbol{\mathcal{X}}) \tag{B-11}$$

Then the components of the second Piola-Kirchhoff and Cauchy stress tensors are related by:

$$ \sigma_{ij} = \det\left(\frac{\partial \mathbf{x}}{\partial \mathbf{X}}\right) \frac{\partial \mathbf{X}_i}{\partial \mathbf{x}_m}\, \tau_{mn}\, \frac{\partial \mathbf{X}_j}{\partial \mathbf{x}_n} \tag{B-12}$$

$$ \tau_{ij} = \det\left(\frac{\partial \mathbf{X}}{\partial \mathbf{x}}\right) \frac{\partial \mathbf{x}_i}{\partial \mathbf{X}_m}\, \sigma_{mn}\, \frac{\partial \mathbf{x}_j}{\partial \mathbf{X}_n} \tag{B-13}$$

APPENDIX C
ENERGY CONJUGANCE OF 2PK AND GL TENSORS

It is instructive to prove that the Piola-Kirchhoff stress tensor is energetically conjugate to the Green-Lagrange strain tensor, *i.e.*, at some arbitrary time t

$$\int_{{}^0V} {}^t\sigma_{ij}\, \delta\, {}^t\epsilon_{ij}\, {}^0dV = \int_{{}^tV} {}^t\tau_{ij}\, \delta\varepsilon_{ij}\, {}^0dV \tag{C-1}$$

The relationship between ${}^t\sigma_{ij}, {}^t\tau_{ij}$ was derived in Appendix B:

$${}^t\sigma_{ij} = \frac{{}^0\rho}{{}^t\rho} \frac{\partial X_i}{\partial\, {}^tx_m}\, \tau_{mn}\, \frac{\partial X_j}{\partial\, {}^tx_n} \tag{C-2}$$

Next, the variation in the Green-Lagrange strain tensor must be related to that of the infinitesimal strain tensor. Begin with the definition for ϵ_{ij} from Appendix A:

$$2\, {}^t\epsilon_{ij}\, dX_i\, dX_j = {}^tdx_i\, {}^tdx_i - dX_i\, dX_i \tag{C-3}$$

Then the variation in ${}^t\epsilon_{ij}$ corresponding to a variation δx_i can be written as

$$2\, \delta\, {}^t\epsilon_{ij}\, dX_i\, dX_j = 2\, {}^tdx_i\, d\, \delta x_i \tag{C-4}$$

where the variation is taken with respect to a fixed (initial) configuration X_i so $d\, \delta X_i = 0$. Recall the definition of the displacement vector, ${}^tx_i = {}^tu_i + X_i$. Then

$$d\, \delta x_i = d\, \delta u_i = \frac{\partial\, \delta u_i}{\partial\, {}^tx_j}\, {}^tdx_j \tag{C-5}$$

and Eq. C-4 becomes

$$\begin{aligned} 2\,\delta^t\epsilon_{ij}\,dX_i\,dX_j &= 2\,\frac{\partial\,\delta u_i}{\partial\,{}^t x_j}\,{}^t dx_i\,{}^t dx_j \\ &= 2\,\delta\varepsilon_{ij}\,{}^t dx_i\,{}^t dx_j \end{aligned} \tag{C-6}$$

Finally, ${}^t dx_i = {}^t\mathcal{X}_{ij}\,dX_j$, so that

$$2\,\delta^t\epsilon_{ij}\,dX_i\,dX_j = 2\,\delta\varepsilon_{ij}\,{}^t\mathcal{X}_{il}\,{}^t\mathcal{X}_{jm}\,dX_l\,dX_m \tag{C-7}$$

and the relationship between $\delta\epsilon_{ij}, \delta\varepsilon_{ij}$ is given by

$$\delta^t\epsilon_{ij} = \delta\varepsilon_{rs}\,{}^t\mathcal{X}_{ri}\,{}^t\mathcal{X}_{sj} \tag{C-8}$$

Now the virtual work in terms of $\sigma_{ij}, \epsilon_{ij}$ can be rewritten by substituting Eqs. C-2, C-8:

$$\int_{{}^0V} {}^t\sigma_{ij}\,\delta^t\epsilon_{ij}\,{}^0dV = \int_{{}^tV} \frac{{}^0\rho}{{}^t\rho}\frac{\partial X_i}{\partial\,{}^t x_m}\frac{\partial X_j}{\partial\,{}^t x_n}\frac{\partial\,{}^t x_r}{\partial X_i}\frac{\partial\,{}^t x_s}{\partial X_j}\,{}^t\tau_{mn}\,\delta\varepsilon_{rs}\,{}^0dV \tag{C-9}$$

But

$$\frac{\partial X_i}{\partial\,{}^t x_m}\frac{\partial\,{}^t x_r}{\partial X_i} = \delta_{mr}, \qquad \frac{\partial X_j}{\partial\,{}^t x_n}\frac{\partial\,{}^t x_s}{\partial X_j} = \delta_{ns} \tag{C-10}$$

and from conservation of mass,

$$\frac{{}^0\rho}{{}^t\rho}\,{}^0dV = {}^t dV \tag{C-11}$$

so Eq. C-9 reduces to

$$\int_{{}^0V} {}^t\sigma_{ij}\,\delta^t\epsilon_{ij}\,{}^0dV = \int_{{}^tV} {}^t\tau_{ij}\,\delta\varepsilon_{ij}\,{}^t dV \tag{C-12}$$

which completes the proof that $\sigma_{ij}, \epsilon_{ij}$ are energetically conjugate.

APPENDIX D
POLAR DECOMPOSITION OF THE DEFORMATION GRADIENT

This appendix contains a proof that the deformation gradient $\boldsymbol{\mathcal{X}}$ can be decomposed into the product of an orthogonal rotation tensor $\mathbf{R}$ and a symmetric stretch tensor $\mathbf{U}$ as

$$\boldsymbol{\mathcal{X}} = \mathbf{RU} \tag{D-1}$$

Begin with the right Cauchy-Green deformation tensor defined in Appendix A, $\boldsymbol{\mathcal{C}} = \boldsymbol{\mathcal{X}}^T\boldsymbol{\mathcal{X}}$, and transform $\boldsymbol{\mathcal{C}}$ to its principal axes:

$$\begin{aligned} \mathcal{C}'_{ij} &= a_{im}a_{jn}\mathcal{C}_{mn} \\ \boldsymbol{\mathcal{C}}' &= \mathbf{a}\boldsymbol{\mathcal{C}}\mathbf{a}^T \end{aligned} \tag{D-2}$$

where $a_{ij} = \mathbf{e}'_i \cdot \mathbf{e}_j$ is the tensor transformation betwen the primed and unprimed coordinate reference frames (whose basis vectors are $\mathbf{e}'_i, \mathbf{e}_i$, respectively). Eq. D-2 is equivalent to the eigenvalue problem, where $\boldsymbol{\mathcal{C}}'$ is a diagonal tensor containing the eigenvalues of $\boldsymbol{\mathcal{C}}$, and the rows of $\mathbf{a}$ are the eigenvectors of $\boldsymbol{\mathcal{C}}$. Now the deformation gradient can be transformed to the same reference frame as $\boldsymbol{\mathcal{C}}'$:

$$\begin{aligned} \mathcal{X}'_{ij} &= a_{im}a_{jn}\mathcal{X}_{mn} \\ \boldsymbol{\mathcal{X}}' &= \mathbf{a}\boldsymbol{\mathcal{X}}\mathbf{a}^T \end{aligned} \tag{D-3}$$

and $\boldsymbol{\mathcal{C}}' = \boldsymbol{\mathcal{X}}'^T\boldsymbol{\mathcal{X}}'$.

Next, define the rotation tensor $\mathbf{R}'$ as follows:

$$\mathbf{R}' = \boldsymbol{\mathcal{X}}'(\boldsymbol{\mathcal{C}}')^{\frac{1}{2}} \tag{D-4}$$

where $(\boldsymbol{\mathcal{C}}')^{\frac{1}{2}}$ is evaluated using the positive roots of $\boldsymbol{\mathcal{C}}'$. We can show that $\mathbf{R}'$ is orthogonal, *i.e.*, $\mathbf{R}'^{T}\mathbf{R}' = \mathbf{I}$ as follows:

$$\mathbf{R}'^{T}\mathbf{R}' = \left((\boldsymbol{\mathcal{C}}'^{T})^{\frac{1}{2}}\boldsymbol{\mathcal{X}}'^{T}\right)\left(\boldsymbol{\mathcal{X}}'(\boldsymbol{\mathcal{C}}')^{\frac{1}{2}}\right) \tag{D-5}$$

but $\boldsymbol{\mathcal{C}}'^{T} = \boldsymbol{\mathcal{C}}'$, since $\boldsymbol{\mathcal{C}}'$ is diagonal, and $\boldsymbol{\mathcal{X}}'^{T}\boldsymbol{\mathcal{X}}' = \boldsymbol{\mathcal{C}}'$, so

$$\mathbf{R}'^{T}\mathbf{R}' = (\boldsymbol{\mathcal{C}}')^{\frac{1}{2}}\boldsymbol{\mathcal{C}}'(\boldsymbol{\mathcal{C}}')^{\frac{1}{2}} = \mathbf{I} \tag{D-6}$$

With the orthogonality of $\mathbf{R}'$ established, the deformation gradient can be decomposed as

$$\boldsymbol{\mathcal{X}}' = \mathbf{R}'\mathbf{U}' \tag{D-7}$$

where $\mathbf{U}$ is a "stretch" tensor which is symmetric and positive-definite:

$$\mathbf{U}' = (\boldsymbol{\mathcal{C}}')^{\frac{1}{2}} \tag{D-8}$$

Finally, $\mathbf{R}', \mathbf{U}'$ can be transformed to the original basis of $\boldsymbol{\mathcal{C}}$ using the inverse of the transformation defined in Eq. D-2:

$$\begin{aligned} \mathbf{R} &= \mathbf{a}^{T}\mathbf{R}'\mathbf{a} \\ \mathbf{U} &= \mathbf{a}^{T}\mathbf{U}'\mathbf{a} \end{aligned} \tag{D-9}$$

This completes the proof of the polar decomposition theorem for the deformation gradient. A more insightful approach is presented by Malvern [1969], in which he shows that the rotation matrix $\mathbf{R}$ rotates the principal axes of the right Cauchy-Green tensor to those of the left Cauchy-Green tensor. Truesdell and Toupin [1960] present a similar derivation using curvilinear coordinates.

APPENDIX E
ROTATION MATRIX FOR SMALL ANGLES

An orthogonal triad may be rotated from some initial configuration by applying rotations θ_i about each axis. Then the transformation of the triad basis vectors from the initial configuration to the final one is given by:

$$\mathbf{e}'_i = R_{ij}(\theta_1, \theta_2, \theta_3)\, \mathbf{e}_j \tag{E-1}$$

where $\mathbf{R}$ is a rotation matrix that is generally a nonlinear function of θ_i and depends on the order in which the θ_i are taken. For example, consider a triad that is rotated in the order θ_1-θ_2-θ_3, as shown in Fig. E.1. The first rotation, θ_1 about the $\mathbf{e}_1$ axis, rotates the triad to the $\mathbf{e}'_i$ configuration:

$$\mathbf{e}'_i = a^1_{ij}(\theta_1)\, \mathbf{e}_j \tag{E-2}$$

where $a^1_{ij} = \mathbf{e}'_i \cdot \mathbf{e}_j$. The next rotation, θ_2 about the $\mathbf{e}'_2$ axis, rotates the triad to the $\mathbf{e}''_i$ configuration:

$$\mathbf{e}''_i = a^2_{ij}(\theta_2)\, \mathbf{e}'_j \tag{E-3}$$

where $a^2_{ij} = \mathbf{e}''_i \cdot \mathbf{e}'_j$. Finally, the θ_3 rotation about the $\mathbf{e}''_3$ axis rotates the triad to the $\mathbf{e}'''_i$ configuration:

$$\mathbf{e}'''_i = a^3_{ij}(\theta_3)\, \mathbf{e}''_j \tag{E-4}$$

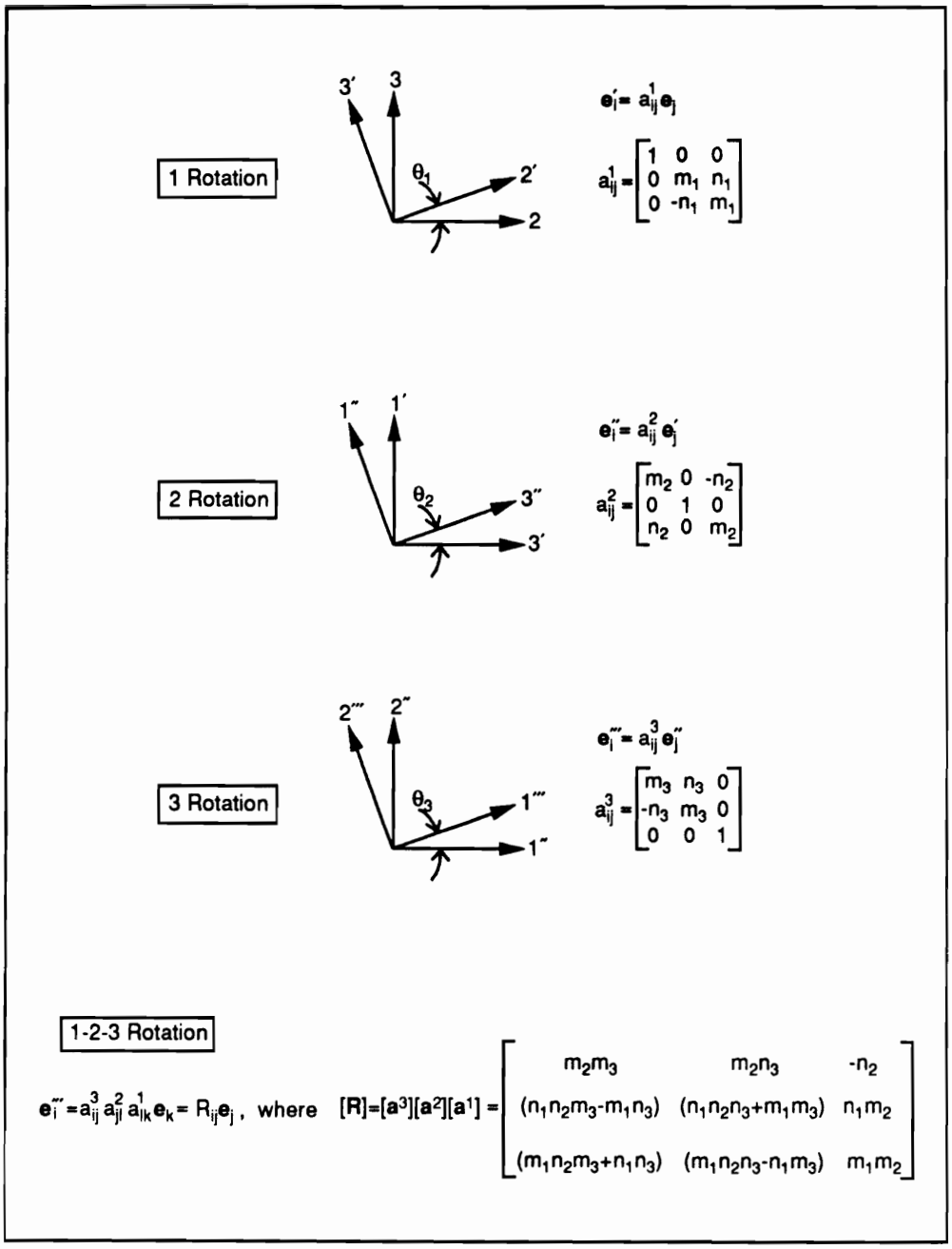

Fig. E.1 1-2-3 Rotation of Orthogonal Triad

where $a_{ij}^3 = \mathbf{e}_i''' \cdot \mathbf{e}_j''$. The components of the transformation matrices $a_{ij}^1, a_{ij}^2, a_{ij}^3$ are listed in Fig. E.1. Now, substituting Eqs. E-2, E-3 in E-4 yields

$$\begin{aligned} \mathbf{e}_i''' &= a_{ij}^3(\theta_3)\, a_{jk}^2(\theta_2)\, a_{kl}^1(\theta_1)\, \mathbf{e}_l \\ &= R_{ij}(\theta_1, \theta_2, \theta_3)\, \mathbf{e}_l \end{aligned} \tag{E-5}$$

where

$$\mathbf{R} = \begin{bmatrix} c\theta_2 c\theta_3 & c\theta_2 s\theta_3 & -s\theta_2 \\ (s\theta_1 s\theta_2 c\theta_3 - c\theta_1 s\theta_3) & (s\theta_1 s\theta_2 s\theta_3 + c\theta_1 c\theta_3) & s\theta_1 c\theta_2 \\ (c\theta_1 s\theta_2 c\theta_3 - s\theta_1 s\theta_3) & (c\theta_1 s\theta_2 s\theta_3 - s\theta_1 c\theta_3) & c\theta_1 c\theta_2 \end{bmatrix} \tag{E-6}$$

and $c\theta = \cos\theta, s\theta = \sin\theta$. Obviously, different results would be obtained for $\mathbf{R}$ if the θ_i were taken in a different order.

If the θ_i are restricted to small to moderate rotations ($\theta < 15°$), the following small angle approximations may be used:

$$\begin{aligned} \cos\theta &\approx 1 \\ \sin\theta &\approx \theta \end{aligned} \tag{E-7}$$

and products of θ are ignored. Then the rotation matrix simplifies to

$$\mathbf{R} = \begin{bmatrix} 1 & \theta_3 & -\theta_2 \\ -\theta_3 & 1 & \theta_1 \\ \theta_2 & -\theta_1 & 1 \end{bmatrix} \tag{E-8}$$

which also can be written in terms of the skew-symmetric matrix $\boldsymbol{\Theta}$:

$$\mathbf{R} = \mathbf{I} + \boldsymbol{\Theta} \tag{E-9}$$

where

$$\boldsymbol{\Theta} = \begin{bmatrix} 0 & \theta_3 & -\theta_2 \\ -\theta_3 & 0 & \theta_1 \\ \theta_2 & -\theta_1 & 0 \end{bmatrix} \tag{E-10}$$

The same small angle approximation for the rotation matrix is obtained regardless of the order in which the rotations are taken, *i.e.*, all the general, nonlinear rotation matrices simplify to the same result given by Eq. E-10.

APPENDIX F
CONSTITUTIVE TRANSFORMATIONS FOR AN OFF-AXIS PLY

The structure is assumed to be constructed from a layered composite material fabricated from orthotropic plies that may rotated about the x_3-axis normal to the laminate (see Fig. F.1). The three-dimensional incremental stress-strain relations for an elastic material are given by the generalized form of Hooke's Law:

$$\sigma_{ij} = C_{ijkl}\epsilon_{kl} \tag{F-1}$$

where C_{ijkl} is a constitutive tensor of rank four with 81 elastic coefficients, and $\sigma_{ij}, \epsilon_{kl}$ are measured with respect to the principal material (ply) reference frame.

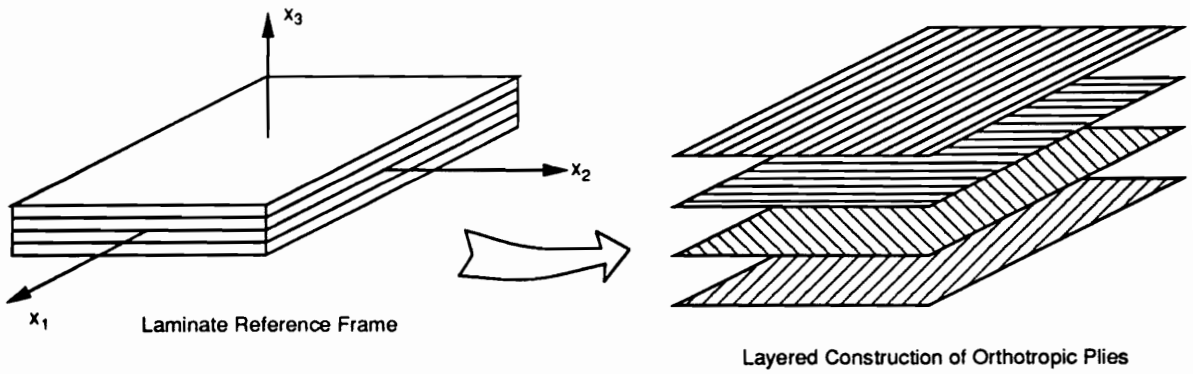

Fig. F.1 Laminated Composite Construction

Due to the symmetry of the stress and strain tensor, it follows that C_{ijkl} possesses the following symmetries:

$$\sigma_{ij} = \sigma_{ji} \quad \longrightarrow \quad C_{ijkl} = C_{jikl}$$
$$\epsilon_{kl} = \epsilon_{lk} \quad \longrightarrow \quad C_{ijkl} = C_{ijlk}$$

which reduces the number of independent coefficients from 81 to 36. This allows for the introduction of a contracted notation for the constitutive relations:

$$\sigma_I = C_{IJ}\epsilon_J \qquad I, J = 1, 2, \ldots, 6 \tag{F-2}$$

where the contraction of indices is completed as follows:

$$\begin{aligned} ij = 11 &\longrightarrow I = 1 & \qquad ij = 23 &\longrightarrow I = 4 \\ ij = 22 &\longrightarrow I = 2 & \qquad ij = 13 &\longrightarrow I = 5 \\ ij = 33 &\longrightarrow I = 3 & \qquad ij = 12 &\longrightarrow I = 6 \end{aligned}$$

For a linearly elastic material, we can postulate the existence of a strain energy density function $u = \frac{1}{2}C_{IJ}\epsilon_I\epsilon_J$ such that [Green and Zerna, 1968]

$$\sigma_I = \frac{\partial u}{\partial \epsilon_I} = \tfrac{1}{2}(C_{IJ} + C_{JI})\epsilon_J \tag{F-3}$$

Comparing Eqs. F-3 and F-2, it follows that $C_{IJ} = C_{JI}$, which reduces the number of independent elastic constants to 21. Finally, if the material is orthotropic, possessing three mutually perpendicular planes of symmetry, the number of elastic constants is reduced to nine (see [Sokolnikoff, 1956], [Fung, 1965]), and the stress-strain relations can be written as

$$\begin{Bmatrix} \sigma_1 \\ \sigma_2 \\ \sigma_3 \\ \sigma_4 \\ \sigma_5 \\ \sigma_6 \end{Bmatrix} = \begin{bmatrix} C_{11} & C_{12} & C_{13} & 0 & 0 & 0 \\ C_{12} & C_{22} & C_{23} & 0 & 0 & 0 \\ C_{13} & C_{23} & C_{33} & 0 & 0 & 0 \\ 0 & 0 & 0 & C_{44} & 0 & 0 \\ 0 & 0 & 0 & 0 & C_{55} & 0 \\ 0 & 0 & 0 & 0 & 0 & C_{66} \end{bmatrix} \begin{Bmatrix} \epsilon_1 \\ \epsilon_2 \\ \epsilon_3 \\ \epsilon_4 \\ \epsilon_5 \\ \epsilon_6 \end{Bmatrix} \tag{F-4}$$

where the shear strains $\epsilon_4, \epsilon_5, \epsilon_6$ are engineering shear strains that are two times the respective tensorial strain components, *e.g.*, $\epsilon_4 = \gamma_{23} = 2\epsilon_{23}$.

The stress and strain tensors are of rank two and obey the tensor transformations laws:

$$\sigma'_{ij} = a_{ik}a_{jl}\sigma_{kl} \tag{F-5}$$

$$\epsilon'_{ij} = a_{ik}a_{jl}\epsilon_{kl} \tag{F-6}$$

where a_{ij} is the tensor transformation matrix

$$a_{ij} = \mathbf{e}'_i \cdot \mathbf{e}_j \tag{F-7}$$

and $\mathbf{e}'_i, \mathbf{e}_i$ are the basis vectors for the primed (ply) and unprimed (laminate) coordinate reference frames, respectively. For a rotation θ about the x_3-axis as shown in Fig. F.2, the transformation is given by

$$a_{ij} = \begin{pmatrix} m & n & 0 \\ -n & m & 0 \\ 0 & 0 & 1 \end{pmatrix} \tag{F-8}$$

where $m = \cos\theta, n = \sin\theta$. For this case the stress and strain transformations given by Eqs. F-5, F-6 can be written in the contracted form by substituting a_{ij} from Eq. F-8:

$$\{\sigma\}_1 = [T]^{-T}\{\sigma\}_x \tag{F-9}$$

$$\{\epsilon\}_1 = [T]\{\epsilon\}_x \tag{F-10}$$

where the subscripts x and 1 refer to the laminate and ply reference frames, respectively, and

$$[T] = \begin{bmatrix} m^2 & n^2 & 0 & 0 & 0 & mn \\ n^2 & m^2 & 0 & 0 & 0 & -mn \\ 0 & 0 & 1 & 0 & 0 & 0 \\ 0 & 0 & 0 & m & -n & 0 \\ 0 & 0 & 0 & n & m & 0 \\ -2mn & 2mn & 0 & 0 & 0 & (m^2 - n^2) \end{bmatrix} \tag{F-11}$$

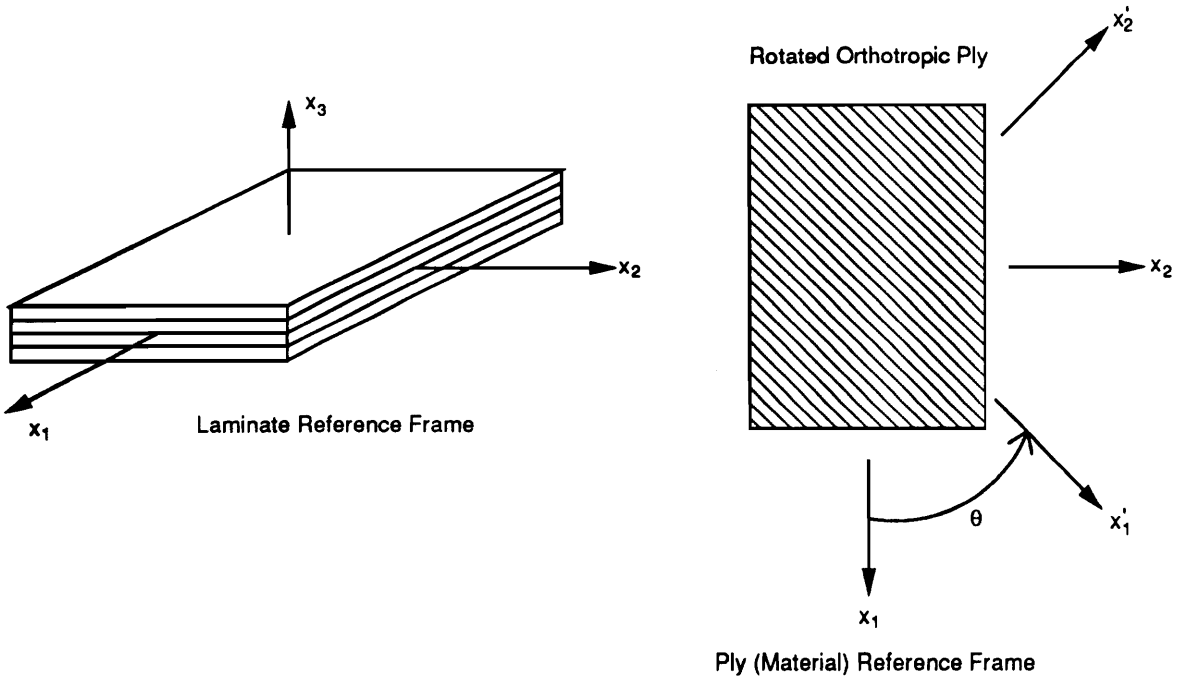

Fig. F.2 Orthotropic Ply with θ Rotation about the x_3-Axis

The notation $[T]^{-T}$ indicates the transpose of the inverse of $[T]$. The inverse of the transformation matrix is simply $[T(\theta)]^{-1} = [T(-\theta)]$, and due to this property

$$[T]^{-T} = \left[[T]^{-1}\right]^{T} = \left[[T]^{T}\right]^{-1} \tag{F-12}$$

The constitutive tensor is of rank four and its transformation is given by

$$C'_{ijkl} = a_{im}a_{jn}a_{ko}a_{lp}C_{mnop} \tag{F-13}$$

For the case of a single rotation about the x_3-axis described above, the contracted transformation equations for C_{IJ} can be derived directly using Eqs. F-9 and F-10. Begin with the constitutive relations in the ply (material) reference frame given by Eq. F-4: $\{\sigma\}_1 = [C]\{\epsilon\}_1$. Substitute Eqs. F-9, F-10 and premultiply both sides by $[T]^T$ to obtain:

$$\{\sigma\}_x = [T]^T[C][T]\{\epsilon\}_x \tag{F-14}$$

But $\{\sigma\}_x = [\overline{C}]\{\epsilon\}_x$,† so

$$[\overline{C}] = [T]^T[C][T] \tag{F-15}$$

Finally, the constitutive relations at a material point can be written as

$$\begin{Bmatrix} \sigma_1 \\ \sigma_2 \\ \sigma_3 \\ \sigma_4 \\ \sigma_5 \\ \sigma_6 \end{Bmatrix}_x = \begin{bmatrix} \overline{C}_{11} & \overline{C}_{12} & \overline{C}_{13} & 0 & 0 & \overline{C}_{16} \\ \overline{C}_{12} & \overline{C}_{22} & \overline{C}_{23} & 0 & 0 & \overline{C}_{26} \\ \overline{C}_{13} & \overline{C}_{23} & \overline{C}_{33} & 0 & 0 & \overline{C}_{36} \\ 0 & 0 & 0 & \overline{C}_{44} & \overline{C}_{45} & 0 \\ & & & \overline{C}_{45} & \overline{C}_{55} & 0 \\ \overline{C}_{16} & \overline{C}_{26} & \overline{C}_{36} & 0 & 0 & \overline{C}_{66} \end{bmatrix} \begin{Bmatrix} \epsilon_1 \\ \epsilon_2 \\ \epsilon_3 \\ \epsilon_4 \\ \epsilon_5 \\ \epsilon_6 \end{Bmatrix}_x \tag{F-16}$$

where the components of $\overline{C}$ are listed below.

Elastic Coefficients for an Orthotropic Ply with Rotation θ about the x_3-Axis

$$\begin{aligned}
\overline{C}_{11} &= m^4C_{11} + 2m^2n^2(C_{12} + 2C_{66}) + n^4C_{22} \\
\overline{C}_{12} &= m^2n^2(C_{11} + C_{22} - 4C_{66}) + (m^4 + n^4)C_{12} \\
\overline{C}_{13} &= m^2C_{13} + n^2C_{23} \\
\overline{C}_{16} &= m^3n(C_{11} - C_{12} - 2C_{66}) + mn^3(C_{12} - C_{22} + 2C_{66}) \\
\overline{C}_{22} &= n^4C_{11} + 2m^2n^2(C_{12} + 2C_{66}) + m^4C_{22} \\
\overline{C}_{23} &= n^2C_{13} + m^2C_{23} \\
\overline{C}_{26} &= mn^3(C_{11} - C_{12} - 2C_{66}) + m^3n(C_{12} - C_{22} + 2C_{66}) \\
\overline{C}_{33} &= C_{33} \\
\overline{C}_{36} &= mn(C_{13} - C_{23}) \\
\overline{C}_{44} &= m^2C_{44} + n^2C_{55} \\
\overline{C}_{45} &= mn(C_{55} - C_{44}) \\
\overline{C}_{55} &= n^2C_{44} + m^2C_{55} \\
\overline{C}_{66} &= m^2n^2(C_{11} - 2C_{12} + C_{22}) + (m^2 - n^2)^2C_{66}
\end{aligned}$$

† We adopt the notation from classical lamination theory [Jones, 1975] and use an overbar to denote quantities referred to the laminate reference frame.

In the present study, the structural components are assumed to be thin and so can be considered to be in a state of plane stress. Then ϵ_3 can be eliminated from the constitutive equations using the condition that $\sigma_3 = 0$. From Eq. F-16:

$$\sigma_3 = \overline{C}_{13}\epsilon_1 + \overline{C}_{23}\epsilon_2 + \overline{C}_{33}\epsilon_3 + \overline{C}_{36}\epsilon_6 = 0 \tag{F-17}$$

which can be solved for ϵ_3:

$$\epsilon_3 = -\frac{1}{\overline{C}_{33}}(\overline{C}_{13}\epsilon_1 + \overline{C}_{23}\epsilon_2 + \overline{C}_{36}\epsilon_6) \tag{F-18}$$

This result can be substituted in Eq. F-16 to eliminate ϵ_3, which yields the following for the constitutive equations:

$$\begin{Bmatrix} \sigma_1 \\ \sigma_2 \\ \sigma_4 \\ \sigma_5 \\ \sigma_6 \end{Bmatrix}_x = \begin{bmatrix} \overline{Q}_{11} & \overline{Q}_{12} & 0 & 0 & \overline{Q}_{16} \\ \overline{Q}_{12} & \overline{Q}_{22} & 0 & 0 & \overline{Q}_{26} \\ 0 & 0 & \overline{C}_{44} & \overline{C}_{45} & 0 \\ 0 & 0 & \overline{C}_{45} & \overline{C}_{55} & 0 \\ \overline{Q}_{16} & \overline{Q}_{26} & 0 & 0 & \overline{Q}_{66} \end{bmatrix} \begin{Bmatrix} \epsilon_1 \\ \epsilon_2 \\ \epsilon_4 \\ \epsilon_5 \\ \epsilon_6 \end{Bmatrix}_x \tag{F-19}$$

where $\overline{\mathbf{Q}}$ is the reduced stiffness matrix for the plane stress components of stress and strain:

$$\overline{Q}_{IJ} = \overline{C}_{IJ} - \frac{\overline{C}_{I3}\overline{C}_{J3}}{\overline{C}_{33}} \qquad I, J = 1, 2, 6 \tag{F-20}$$

Equation F-19 can be reordered to form membrane and transverse shear partitions:

$$\begin{Bmatrix} \boldsymbol{\sigma}^{(M)} \\ \boldsymbol{\sigma}^{(S)} \end{Bmatrix} = \begin{bmatrix} \overline{\mathbf{Q}} & \mathbf{0} \\ \mathbf{0} & \overline{\mathbf{C}}^{(S)} \end{bmatrix} \begin{Bmatrix} \boldsymbol{\epsilon}^{(M)} \\ \boldsymbol{\epsilon}^{(S)} \end{Bmatrix} \tag{F-21}$$

where

$$\boldsymbol{\sigma}^{(M)} = \begin{Bmatrix} \sigma_1 \\ \sigma_2 \\ \sigma_6 \end{Bmatrix}, \qquad \boldsymbol{\sigma}^{(S)} = \begin{Bmatrix} \sigma_5 \\ \sigma_4 \end{Bmatrix}$$

and

$$\overline{\mathbf{Q}} = \begin{bmatrix} \overline{Q}_{11} & \overline{Q}_{12} & \overline{Q}_{16} \\ \overline{Q}_{12} & \overline{Q}_{22} & \overline{Q}_{26} \\ \overline{Q}_{16} & \overline{Q}_{26} & \overline{Q}_{66} \end{bmatrix}, \qquad \overline{\mathbf{C}}^{(S)} = \begin{bmatrix} \overline{C}_{55} & \overline{C}_{45} \\ \overline{C}_{45} & \overline{C}_{44} \end{bmatrix}$$

APPENDIX G
FIBER BUNDLE STRENGTH DISTRIBUTION

Rosen [1965] proposed a fiber strength model in which the fiber was assumed to consist of a chain of fiber bundle links. The fiber strength was determined by the probability of failure of the weakest link, and an inverse method was used to determine the statistical strength distribution of a fiber link from experimental strength data. Rosen's model is summarized below.

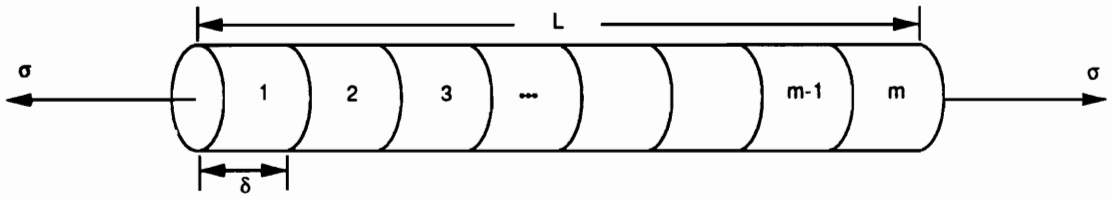

Fig. G.1 Fiber Bundle Chain

Let the fiber be composed of m fiber bundle links of length δ and subjected to axial tension σ as shown in Fig. G.1. Define the probability density function (PDF) and distribution function for fiber bundle failure as $f(\sigma)$ and $F(\sigma)$, respectively, where

$$F(\sigma) = \int_0^{\sigma} f(\xi)\, d\xi \tag{G-1}$$

The failure PDF for the entire chain is obtained by considering the probability that one link fails while the remaining ones survive, and that the failure can occur in any of the m links:

$$g(\sigma) = mf(\sigma)\,[1 - F(\sigma)]^{m-1} \tag{G-2}$$

The strength distribution for the entire fiber bundle chain is:

$$G(\sigma) = \int_0^{\sigma} g(\xi)\,d\xi \tag{G-3}$$

Equation G-3 can be integrated by substituting Eq. G-2 and using the relationship $f = dF/d\sigma$, which yields:

$$G(\sigma) = 1 - \Big[1 - F(\sigma)\Big]^m \tag{G-4}$$

Typically, fiber strength is characterized by a Weibull distribution [Weibull, 1951]. Metcalfe and Schmitze [1964] used the following form to characterize the relationship between fiber length and strength:

$$G(\sigma) = 1 - \exp\left(-\frac{L}{\delta}\left(\frac{\sigma}{\sigma_0}\right)^{\beta}\right) \tag{G-5}$$

$$g(\sigma) = \frac{dG}{d\sigma} = \beta\frac{L}{\delta}\frac{\sigma^{\beta-1}}{\sigma_0^{\beta}}\exp\left(-\frac{L}{\delta}\left(\frac{\sigma}{\sigma_0}\right)^{\beta}\right) \tag{G-6}$$

where L is the fiber length, $L = m\delta$, and σ_0 and β are statistical parameters of the Weibull distribution that can be determined experimentally. The parameter β is a shape factor that is inversely related to the material homogeneity: the smaller the scatter in strength data, the larger the value of β. Gücer and Gurland [1962] reported values of β in the range of two to four for brittle ceramics to about twenty for ductile metals. The parameter σ_0 is a scale factor that defines a reference stress level.

Now the solution of the inverse problem is desired: given the fiber failure PDF $g(\sigma)$ and distribution function $G(\sigma)$, we want to determine the fiber bundle link failure distribution. Begin with Eq. G-4 and solve for $F(\sigma)$:

$$F(\sigma) = 1 - \Big[1 - G(\sigma)\Big]^{\frac{1}{m}} \tag{G-7}$$

and

$$f(\sigma) = \frac{dF}{d\sigma} = \frac{1}{m} g(\sigma) \Big[1 - G(\sigma)\Big]^{\frac{1-m}{m}} \tag{G-8}$$

Substituting Eqs. G-5, G-6 in Eq. G-8 yields:

$$f(\sigma) = \beta \frac{\sigma^{\beta-1}}{\sigma_0^{\beta}} \exp\left(-\left(\frac{\sigma}{\sigma_0}^{\beta}\right)\right) \tag{G-9}$$

and from Eq. G-1:

$$F(\sigma) = \int_0^{\sigma} f(\xi)\, d\xi = 1 - \exp\left(-\left(\frac{\sigma}{\sigma_0}\right)^{\beta}\right) \tag{G-10}$$

VITA

Eduardo Moas was born on February 7, 1960 in Havana, Cuba to Eduardo and Olga Moas. He was raised in Rutherford, New Jersey and graduated from Rutherford High School in 1978. He received a Bachelor of Science degree from Massachusetts Institute of Technology in 1982 and a Master of Science degree from Virginia Polytechnic Institute and State University in 1987. Ed is presently employed with Applied Research Associates, Inc. in Raleigh, North Carolina.